

**Centro de Investigación Científica y de Educación
Superior de Ensenada, Baja California**



**Doctorado en Ciencias
en Óptica con orientación en Optoelectrónica**

**Study of multiple Bessel and Gaussian light-sheet fluorescence
excitations for a large field of view multicolor imaging**

Tesis

para cubrir parcialmente los requisitos necesarios para obtener el grado de
Doctor en Ciencias

Presenta:

Yryx Yanet Luna Palacios

Ensenada, Baja California, México
2022

Tesis defendida por
Yryx Yanet Luna Palacios
y aprobada por el siguiente Comité

Dr. Israel Rocha Mendoza
Director de tesis

Miembros del comité

Dr. Jacob Licea Rodríguez

Dr. Víctor Ruiz Cortes

Dra. Meritxell Riquelme Pérez

Dr. Eric Olaf Potma



Dra. Karina Garay Palmett
Coordinadora del Posgrado en Óptica

Dr. Pedro Negrete Regagnon
Director de Estudios de Posgrado

copyright © 2022

Queda prohibida la reproducción parcial o total de esta obra sin el permiso formal y explícito del autor y director de la tesis.

Resumen de la tesis que presenta **Yryx Yanet Luna Palacios** como requisito parcial para la obtención del grado de Doctor en Ciencias en Óptica con orientación en Optoelectrónica

Estudio de la excitación múltiple de la fluorescencia con hojas de luz Bessel y Gaussianas para la obtención de imágenes multicolores con campo de visión amplio

Resumen aprobado por:

Dr. Israel Rocha Mendoza
Director de tesis

La microscopía multicolor de campo amplio es indispensable para realizar estudios de biología del desarrollo. Tales estudios requieren, necesariamente, de una visualización simultánea de la dinámica de los diferentes componentes sub-celulares. Para tales propósitos, la microscopía de fluorescencia con hoja de luz láser (LSFM, por sus siglas en inglés) resulta ser una técnica de imagen poderosa por su capacidad de obtener de forma rápida imágenes tridimensionales de campo amplio. Sin embargo, utilizar diferente longitud de onda para la adquisición de imágenes multi-fluorescentes en muestras biológicas grandes bajo un sistema LSFM con haces Gaussianos, conlleva a diferentes posiciones de enfoque (debido a un retraso cromático intrínseco). Además, el ancho de las hojas de luz no se preserva en todo el campo de visión (FOV, por sus siglas en inglés) del objetivo de colección. Esto obliga a realizar una excitación no simultánea con hojas de diferente longitud de onda en diferentes zonas del objeto, uniendo posteriormente las imágenes obtenidas. En este contexto, este trabajo de tesis doctoral presenta un estudio comparativo entre la excitación múltiple de la fluorescencia con hojas de luz de Bessel y con hojas de luz Gaussianas para adquirir imágenes multicolores con FOV largo. Las hojas de luz multicolor y la resolución óptica de las diferentes configuraciones LSFM son discutidas con base a su caracterización experimental. De manera particular, se enfatizan las implicaciones que conllevan la excitación multi-cromática con hojas de luz de diferentes colores para lograr un FOV colocalizado. Con base a los resultados de este estudio, se demuestra que el uso de múltiples haces de Bessel es más adecuado para obtener imágenes multicolores en un campo de visión amplio. Superando con ello los problemas ópticos fundamentales originados al utilizar hojas de luz Gaussianas. Para demostrar las ventajas de la LSFM multicolor con haces Bessel, se utilizaron peritecios de *Sordaria macrospora*. Los resultados de este estudio han sido publicados recientemente (Luna-Palacios, Y. Y. et al., *Journal of Biophotonics*, 2022 <https://doi.org/10.1002/jbio.202100359>), complementando estudios previos que comparan solamente la excitación monocromática.

Palabras clave: Microscopía, Hojas de Luz, Haces Bessel, Haces Gaussianos, multicolor, *Sordaria macrospora*

Abstract of the thesis presented by **Yryx Yanet Luna Palacios** as a partial requirement to obtain the Doctor of Science degree in Optics with orientation in Optoelectronics

Study of multiple Bessel and Gaussian light-sheet fluorescence excitations for a large field of view multicolor imaging

Abstract approved by:

Dr. Israel Rocha Mendoza
Thesis Director

Multicolor wide-field imaging is essential for developmental biology experiments where the simultaneous visualization of different dynamic subcellular components is necessary. For those purposes, light-sheet fluorescence microscopy (LSFM) is a proven and powerful imaging technique since it can obtain rapid 3D wide-field imaging. However, when imaging large biological samples under an LSFM setup based on Gaussian excitation beams, the fluorescence excitation is often monochromatic because different wavelength beams lead to different focal positions due to the intrinsic chromatic defocusing. Additionally, the width of the light sheets is not uniform throughout the collection objective lens field of view (FOV). In this context, this doctoral project aims to perform a comparative study between multiple Bessel and Gaussian light-sheet fluorescence excitations for a large field of view multicolor imaging implementation. The multicolor light-sheets and optical resolution of the different LSFM configurations were experimentally characterized and discussed. A particular emphasis on the chromatic implications of the different-color light-sheet excitations to achieve colocalized FOV is highlighted. Based on the results of this study, the use of multiple Bessel beams is better suited for a large field of view multicolor imaging, overcoming fundamental optical problems that originate when using multiple Gaussian light sheets. LSFM imaging of *Sordaria macrospora* perithecia samples demonstrates such advantages. This study has been recently published (Luna-Palacios, Y. Y. et. al., *Journal of Biophotonics*, 2022 <https://doi.org/10.1002/jbio.202100359>), complementing previous comparative studies between Gaussian and Bessel beam-based LSFM implementations that discuss only single wavelength light-sheet excitations.

Keywords: Microscopy, Light Sheet, Bessel beams, Gaussian beams, multicolor, *Sordaria macrospora*.

Dedication

A mis Padres y amigos

Acknowledgments

A mi familia que siempre aunque a la distancia me han apoyado.

A mi director de tesis, el Dr. Israel Rocha Mendoza. Por su apoyo durante todo el proyecto.

A los miembros de mi comité de tesis, a la Dra. Meritxell Riquelme Pérez, Dr. Jacob Licea Rodríguez, Dr. Víctor Ruiz Cortes y al Dr. Eric Potma. Por aceptar ser parte de este comité y por siempre hacer críticas constructivas a este trabajo.

A todo el personal del departamento de óptica que siempre me apoyaron haciendo este proyecto más ameno.

Al Centro de Investigación Científica y de Educación Superior de Ensenada por la oportunidad de realizar mis estudios de posgrado.

Al Consejo Nacional de Ciencia y Tecnología (CONACyT) por brindarme el apoyo económico para realizar mis estudios de doctorado. No. de becario: 628904 y por el apoyo económico para la realización de una estancia en el extranjero (Beca de movilidad CONACyT 2019)

“Je vous écris tout ça d’un autre monde, un monde d’apparence. D’une certaine façon, les deux modes communiquent. La mémoire est pour l’autre: une impossibilité.”

“Les légendes naissent du besoin de déchiffrer l’indéchiffrable, les mémoires doivent se contenter de leurs délires, de leurs dérives.” Chris Marker, 1983.

Os escribo todo esto desde otro mundo, un mundo de apariencias. En cierto modo, los dos mundos se comunican. La memoria es para uno lo que la historia es para el otro: una imposibilidad.

Las Leyendas nacen de la necesidad de descifrar lo indescifrabable, las memorias tienen que conformarse con su delirio, con su deriva. Chris Marker, 1983.

Contents

Abstract in spanish.....	ii
Abstract.....	iii
Dedication.....	iv
Acknowledgments.....	v
List of figures.....	viii
List of tables.....	xii
Chapter 1. Introduction.....	1
1.1 Dissertation background	3
1.2 Hypothesis.....	4
1.3. Objective	4
1.4 Thesis structure	4
Chapter 2. Fundamental Theory.....	6
2.1 Transverse laser beam profiles	6
2.2 Gaussian beams.....	7
2.2.1 Depth of focus of Gaussian beams is the depth of field of an optical system	9
2.3 Bessel beams	9
2.3.1 Bessel beams generation	11
2.3.2 Bessel beams self-reconstruction property	13
2.4 Light Sheet Fluorescence Microscopy	14
2.4.1 Different LSFM arrangements (SPIM, DSLM).	15
2.4.2 LSMF parameters	19
2.4.3 LSFM drawbacks.....	21
2.5 Fluorescence	22
2.5.1 Fluorochromes, photodamage, and photobleaching.....	23
2.6 Beam propagation.....	24
2.7 <i>Sordaria macrospora</i>	26
Chapter 3. Methodology.....	28
3.1 Axicon lens	28

3.2 Multicolor LSFM optical setup	30
3.2.1 Excitation system	31
3.2.2 Collection system	32
3.3 Computational methods	33
3.3.1 Image processing and data storage	33
3.3.2 Beam propagation simulation	35
3.4 LSFM system characterization.....	37
3.4.1 Light-sheets characterization	37
3.4.2 Optical resolution characterization.....	37
3.5 Biological samples: <i>Sordaria macrospora</i>	37
Chapter 4. Results and Discussion	39
4.1 Bessel beams formation using an axicon lens.....	39
4.1.1 Bessel beams characterization after the axicon	39
4.1.2 Bessel beams characterization at the excitation objective back focal plane.....	43
4.2 Optical setup characterization	44
4.2.1 Multicolor light-sheets	44
4.2.2 Multicolor light-sheets FOVs.....	45
4.2.3 Multicolor light sheets optical sectioning	47
4.2.4 Optical sectioning vs. FOV ratio	47
4.2.5 The chromatic axial focal shifts limitation of Gaussian beams for multicolor LSFM	47
4.2.6 Lateral and axial resolution	50
4.2.7 Axial resolution variation over the FOV	52
4.3 Light Sheet <i>Sordaria macrospora</i> imaging	53
4.3.1 Small samples.....	53
4.3.2 Large samples.....	55
4.3.3 <i>Sordaria macrospora</i> imaging with LSFM vs. confocal microscopy	57
4.4 Bessel vs. Gaussian beam focusing under the same objective lens.....	57
4.4.1 Bessel vs. Gaussian beam under the same NA.....	58
4.4.2 Bessel vs. Gaussian beam under the same FOV.....	59
4.4.3 LSFM axial resolution dependence on the collection objective DoF	59

Chapter 5. Conclusions	62
5.1 Light-sheets characterization	62
5.2 Biological samples imaging	63
5.3 Beam propagation simulations	63
5.4 Future work.....	64
5.5 Publications derived from the thesis	64
References.....	66
Annexes.....	72
Image processing and data storage	72
Beam propagation simulation.....	74

List of figures

Figure 1 Gaussian and Bessel beams profiles. (a) Gaussian beam and (b) Bessel beam.	7
Figure 2 Gaussian beam propagation as a function of the propagation coordinate z . a) Beam width of a Gaussian beam as a function of the propagation coordinate z , The beam waist w_0 , Rayleigh range z_R , divergence angle θ and the radius of curvature $R(z)$, the image is a modified version of Figure 1 from (Garcia-ortiz et al., 2017). b) Depth of field and depth of focus from a lens (L).	10
Figure 3 Experimental arrangement to create a zero-order Bessel beam. The image is a modified version of Figure 2 from (Durnin et al., 1987).	11
Figure 4 The demonstration of Bessel beam generation using an axicon prism (Cizmar, 2006).....	12
Figure 5 Bessel beam reconstruction. The figure shows a cross-section of the Bessel beam as it propagates from left to right. The intensity profile of the Bessel beam is seen to reform even after encountering an obstruction (green circle). The image is a modified version of Figure 3 from (Mcgloin & Dholakia, 2005).....	13
Figure 6 General LSFM configuration; CO, collection objective; F, filter; TL, tube lens; CMOS, camera; and xyz, laboratory coordinate system.	15
Figure 7 SPIM diagram. A single cylindrical lens (CL) is used to form the light-sheet inside to sample (S); the collection objective (CO) collects the fluorescent image at a determined sample plane. Image adapted from (Huisken & Stainier, 2009).....	17
Figure 8 DSLM diagram. A galvanometric mirror oscillates at the Nyquist frequency vertically along the sample forming a virtual light sheet. A conjugated plane lens is used to pivot the laser into the back focal aperture of the objective excitation. Figure modified and taken from (Keller et al., 2011).	18
Figure 9 Three LSFM important parameters. The image represents the top view of an LSFM. EO, excitation objective, CO collection objective, NA_{EO} numerical Aperture from EO, NA_{CO} numerical Aperture from CO, n refraction index of the sample. The excitation beam (blue). The collection beam (green). The dotted lines indicate the field of view of the sheet. The red arrow the axial resolution or the optical sectioning (δz). The black arrow the lateral resolution for LSFM (δx).	19
Figure 10 Jablonski diagram for a green fluorescent molecule. $h\nu_{ex}$ excitation light (ex) and $h\nu_{em}$ emission light. A molecule in state S_0 absorbs energy from blue light (488 nm); this causes the molecule to pass to state S_1 . From S_1 , the molecule loses energy non-radiatively and emits a green photon (507 nm) when relaxing back to S_0	22
Figure 11 Cartesian coordinates to cylindrical coordinate's transformation.	24
Figure 12 focusing beam in cylindrical coordinates.....	25

- Figure 13** Life cycle of *Sordaria macrospora*. Figures represent different stages observed at different days of incubation (0 to 7 days). The final stage, the perithecium, is shown as a scanning electron micrograph. The figure was taken from (Engh et al., 2010). 27
- Figure 14** Schematics for an axicon lens. 29
- Figure 15** Experimental layout for the Bessel beam characterization after the axicon. a) Characterization of the Bessel beam generated by the axicon. b) Bessel beams at the Fourier plane characterization. Axicon (AX), Lens $f = 50$ mm (L1)..... 30
- Figure 16** Multicolor LSFM layout for DSLM and SPIM configuration using Gaussian and Bessel beams. AX, axicon; FL and L1, achromatic lenses; GM, galvanometric mirror; SL, scanning lens; TL, tube lens; EO, excitation objective; CO, collection objective; IMF, interferometric multiband filter; CMOS, camera; CL: achromatic cylindrical lens; and xyz, laboratory coordinate system. 32
- Figure 17** Image processing analysis workflow..... 34
- Figure 18** Fit PSF used in the LSFM deconvolution process. a) PSF along zy axis, b) PSF central plane along yx axis, c) PSF central plane duplicate the number of images from the stack..... 35
- Figure 19** Beam propagation program flow diagram..... 36
- Figure 20** Sample preparation for LSFM. After 13 days of growth, a block of 1 cm^2 was cut using a sterile scalpel. The block was mounted into a quartz cuvette. Then the quartz cuvette was mounted onto a custom-designed holder attached to the computer-controlled XYZ translational stage with the sample facing toward the CO..... 38
- Figure 21** Experimental and simulated xy transverse images generated by an axicon lens at different distances along the z axis 40
- Figure 22** Beam propagation of an axicon lens along z axis. a) Propagation of rays coming from axicon lens using the geometric optics approximation a) Intensity profile obtained using the model implemented by Brzobohat' 2008 in MATLAB, c) Intensity profile obtained from a 3D reconstruction of an experimental data. All the calculations were performed considering an excitation wavelength of 488 nm and a beam radius (ω_0) of 4.1 cm. 41
- Figure 23** Fourier transform of an axicon lens. a) diagram of an axicon and a lens used to generate the Fourier transform at the focus plane, where a CCD camera was used to obtain the images (model using geometric optics). (b, c, and d) Simulated Fourier transform for a wavelength of 445nm, 488 nm, and 561 nm, respectively. (e-g) Experimental Fourier transform images for a wavelength of 445nm, 488 nm, and 561 nm, respectively..... 42
- Figure 24** Input Bessel beam profile at the excitation objective back focal aperture in the LSFM. a-c) Fourier transform at the back focal aperture of the excitation objective for 445nm, 488 nm and 561 nm, respectively. d) Zoom of the ring from picture b. e) Intensity profile corresponding to the dashed line in picture d)..... 43
- Figure 25** Characterization of the multicolor light sheets for the different configurations. Fluorescence images of the static (non-scanned) focused beams at 445, 488, and 561 nm for DSLM-Bessel (a), DSLM-Gaussian (b), and SPIM (c). The white arrows in (a-c) indicate the beam propagation. Normalized intensity profile traces along x-direction for DSLM-Bessel (d), DSLM-Gaussian (e),

and SPIM (f); and y-direction for DSLM-Bessel (g), DSLM-Gaussian (h), and SPIM (i). The FWHM widths values are shown in Table 2. The shadowed gray area in Figures. (d-f) indicates the effective FOV. The yellow dash lines in Figure b indicate the achromatic shifting between 445 and 561 nm of DSLM-Gaussian. The inset image in Figure (e) shows the focal shift between DSLM-Bessel and -Gaussian beams for 561nm..... 45

- Figure 26** Lateral and axial resolution measurement for the three LSFM configurations using 0.16 μm fluorescent beads excited with the laser at 488 nm. Images of the point spread functions (PSFs) measured in both directions: a-c) lateral and g-i) axial. Normalized intensity profiles of the PSF in the d-f) lateral and j-l) axial directions measured along the dashed lines indicated in Figures. a-c) and g-i), respectively. The solid lines represent the corresponding fits of the experimental intensity profile traces. The lateral and axial average PSF widths measured at the FWHM value are summarized in table 3. Scale bar 1 μm 51
- Figure 27.** Axial resolution variation over the different LSFM configurations FOV. Maximum intensity projection images for DSLM-Bessel (a), DSLM-Gaussian (b), and SPIM (c). A total of 200 planes are acquired with a step of 0.1 μm along the z-direction. The axial PSF profile traces were obtained at Zone 1 (d), Zone 2 (e), and Zone 3 (f); these zones are indicated with white squares in (a-c). The red open triangle traces correspond to DSLM-Bessel; the blue open circles are for DSLM-Gauss, and the black open squares for SPIM. The fits of the experimental intensity profile traces are represented by the solid lines with the corresponding color. Scale bar 10 μm 52
- Figure 28** MIP images of a living perithecium of *Sordaria macrospora* after eight days of growth expressing the tdTomato fluorescent protein in the nuclei and the cell walls stained with SF7 acquired with the different LSFM configurations. a-c) DSLM-Bessel, d-f) DSLM-Gaussian, and g-i) SPIM; j) Intensity profile obtained from the dotted lines in figures b), e), and h). The white arrows in b), e), and h) indicate the incoming light-sheet direction and the blue arrows indicate structures with lower contrast in figure j. 54
- Figure 29** MIP images of a living perithecium of *Sordaria macrospora* of 16-days development expressing the tdTomato fluorescent protein in the nuclei and the cell wall stained with SF7 acquired with DSLM-Gaussian (a, c) and DSLM-Bessel (b, d) configurations. The collection objectives utilized were 20X (a, b) and 50X (c, d). In figures (c,d), the right and bottom insets are the in-depth yz-images and the focused Gaussian and Bessel beams, respectively. Scale bar 20 μm 56
- Figure 30** Z-projection images of a living perithecium of *Sordaria macrospora* acquired with a) commercial CLSM system (NA=1.42) and b) DSLM-Bessel configuration (NA=0.40). The scale bar is 20 μm 57
- Figure 31** Bessel (a) and Gaussian (b) beam propagation under a 0.16 NA objective. Both cases are under experimental settings. (c) Gaussian beam propagation through a 0.05 NA for obtaining a similar DoF as in the focused excitation Bessel beam. Normalized intensity profile traces along the x-direction (d) and z-direction (e) of figures a, b and c. The beam's propagation is simulated at 488 nm in free space. 58
- Figure 32.** LSFM Image and axial beam profile dependence on the collection objective Numerical Aperture. (a) Experimental scheme to demonstrate the effect of the DoF (b) XY-plane of Bessel beam intensity image integrated over different collection objective Numerical Apertures (i.e., different DOF, as indicated). 60

Figure 33 Beam profiles traced along the axial (z-direction) of the image simulation in **Figure 32** compared with the experimental results. (a) Bessel, (b) Gaussian. The cyan trace in (b) and (c) corresponds to the experimental axial beam profiles of **Figure 25 g** and **h**, respectively. Gray line: simulation of the axial beam profile from an objective with NA = 0.25. Light gray line: simulation of the axial beam profile from an objective with NA = 0.55 and the central plane black line. 61

Figure 34 Bessel (a) and Gaussian (b) beam propagation under a 0.16 NA objective. Both cases are under experimental settings for 445 nm. Normalized intensity profile traces along the x-direction c) and z-direction d) of figures a, b. Bessel (e) and Gaussian (f) beam propagation under a 0.16 NA objective. Both cases are under experimental settings for 561 nm. Normalized intensity profile traces along the x-direction e) and z-direction f) of figures e, f..... 74

List of tables

Table 1	Performance comparison of DLSM with other fluorescence microscopies.....	18
Table 2	Lateral and axial FWHM widths for the different LSFM configurations and wavelengths	44
Table 3	Axial focal shifts of different objectives class in LSFM.....	49
Table 4	Lateral and axial average PSF widths at the FWHM for the different LSFM configurations	51

Chapter 1. Introduction

Light-sheet fluorescence microscopy (LSFM) is a powerful wide-field imaging technique that allows obtaining optically sectioned images of volumetric samples with an excellent optical resolution, which is useful for performing a three-dimensional (3D) reconstruction of large organisms (Fahrbach et al., 2010; Olarte et al., 2012; Fahrbach, Gurchenkov, et al., 2013b; Müllenbroich, Silvestri, et al., 2018; Jia et al., 2019). In LSFM, a thin light sheet illuminates a specific sample plane; therefore, the fluorescence signal is excited selectively only at this plane. The fluorescent signal is then collected by the detection objective placed perpendicularly to the exciting plane and then imaged onto a camera. The advantages of LSFM over other fluorescence microscopy techniques capable of obtaining 3D images, such as laser scanning confocal microscopy, are the faster acquisition speed, reduced sample photobleaching, and good optical resolution obtained at higher visualization depths. Gaussian beams are commonly utilized to create the light sheet; however, due to its intrinsic diffractive nature, the light sheet is strongly degraded as it propagates through the scattering samples (as many biological samples). Consequently, a limited and non-homogeneous field of view (FOV) is obtained (Fahrbach et al., 2010; Olarte et al., 2012; Müllenbroich, Silvestri, et al., 2018).

Alternatively, Bessel beams are non-diffracting light beams that with the ability to self-reconstruct while propagating; therefore, such beams have also been employed in LSFM to generate the light-sheet and mitigate the Gaussian beam's diffraction drawbacks (Fahrbach et al., 2010; Müllenbroich, Silvestri, et al., 2018; Müllenbroich, Turrini, et al., 2018). The self-healing properties of Bessel beams allow them to recover their original profile, even in the presence of massive phase perturbations induced by undesired artifacts within the samples, and to produce a more extended depth of field (DoF) when the beams are focused (Fahrbach et al., 2010; Olarte et al., 2012; Takanezawa et al., 2021). Because of all this, Bessel beams have proven to improve the light-sheet homogeneity resulting in a more uniform sample illumination (Fahrbach et al., 2010; Planchon et al., 2011; Olarte et al., 2012; Fahrbach, Gurchenkov, et al., 2013b; Lau et al., 2018; Müllenbroich, Silvestri, et al., 2018; Müllenbroich, Turrini, et al., 2018; Xiong et al., 2020; Takanezawa et al., 2021), producing wider FOVs, which are useful for the visualization of large biological samples like mouse brains [5], Zebrafish brains and hearts (Lau et al., 2018; Müllenbroich, Turrini, et al., 2018), and chick embryos (MacDonald et al., 2017).

The main drawback of Bessel beams for LSFM is the presence of intense side lobes, which illuminate out-of-focus sample regions (Vettenburg et al., 2014; Remacha et al., 2020; Xiong et al., 2020). In addition to compromising the optical sectioning slightly (and thus the axial resolution), these side lobes introduce a

small background signal to the acquired images, slightly reducing image contrast and blurring (Fahrbach, Gurchenkov, et al., 2013a; Gao et al., 2014; MacDonald et al., 2017; Di Domenico et al., 2018; Xiong et al., 2020). Therefore, for 3D imaging of small samples, say slightly larger than the light-sheet thickness, the out-of-focus fluorescence can be reduced by using confocal line-scanning detection, spatial filtering techniques, or beam subtraction methods, among others (Di Domenico et al., 2018; Müllenbroich, Turrini, et al., 2018; Jia et al., 2019; Xiong et al., 2020). Nonlinear two-photon fluorescence excitation processes have also been utilized to overcome such drawbacks (Olarte et al., 2012; Fahrbach, Gurchenkov, et al., 2013a; Gao et al., 2014; Takanezawa et al., 2021). Here, the generated fluorescence at the central Bessel peak dominates over the fluorescence at the side lobes, improving the beam penetration depth and image background rejection. In contrast, when the objective is to perform 3D imaging over large and volumetric samples (larger than light-sheet thickness), the extended FOV produced with focused Bessel beams is still very attractive for multicolor imaging despite the compromised optical sectioning capability of Bessel beams mentioned above. In addition, one should bear in mind that when the same numerical aperture (NA) of the excitation objective is utilized to create both Bessel and Gaussian beams, their axial sectioning could be comparable, depending on the collection objective's NA, as shown later in this work.

Bessel beams have already been implemented in LSFM using complex optical systems, such as spatial light modulators (Fahrbach et al., 2010; MacDonald et al., 2017; Jia et al., 2019; Meinert & Rohrbach, 2019), and pupil filters of different phase distributions (Planchon et al., 2011; Xiong et al., 2020). Other more straightforward schemes utilize commercially available axicons (conical lenses) to form the Bessel beams resulting in a less expensive and easy-to-use alternative (Olarte et al., 2012; Müllenbroich, Silvestri, et al., 2018; Müllenbroich, Turrini, et al., 2018; Takanezawa et al., 2021), or even design custom-made micro-axicons (Li et al., 2021). It is worth noting that only a few of these configurations perform multicolor imaging (Planchon et al., 2011; Vettenburg et al., 2014; Zhao et al., 2016), and that the ones using axicons commonly utilize a single wavelength excitation (Olarte et al., 2012; Müllenbroich, Silvestri, et al., 2018; Müllenbroich, Turrini, et al., 2018; Takanezawa et al., 2021). Multicolor wide-field imaging is of the utmost importance to conduct developmental biology experiments, where a simultaneous visualization of different dynamic subcellular components (marked each with specific fluorescent proteins) is required, for instance, to elucidate their functionality for a particular biological process. Therefore, the large FOV achieved with a multicolor Bessel LSFM configuration, rather than with the Gaussian beam-based ones, is ideal for spanning the possibility of tracking different regions of interest (ROIs) simultaneously in such developmental studies. Additionally, Bessel beams are, in principle, better suited for overcoming the unavoidable chromatic problems and scattering effects of Gaussian beams for multicolor LSFM imaging.

1.1 Dissertation background

In an attempt to perform multicolor light-sheet imaging over a large field of view, the Advanced Microscopy Group at CICESE recently implemented a wide-field multicolor LSM system for the rapid and quasi-simultaneous acquisition of multicolor images (with multiple fluorophores). The system was implemented under a Selective Plane Illumination Microscopy (SPIM) configuration using three static Gaussian light-sheets and a single channel detection (Licea-Rodriguez et al., 2019). Despite the excellent homogeneity achieved with the multicolor excitation light-sheets, the sheet thickness (and so the optical sectioning) was compromised due to the long focal length of the cylindrical lens used to form the sheets. Moreover, using higher numerical aperture microscope objectives to create the multiple excitation light-sheets for wide-field imaging over large and volumetric samples was problematic because of their shorter DoF. It also conveyed the inherent chromatic defocusing (Abdeladim et al., 2019) and scattering problems of Gaussian beams for LSM imaging (Fahrbach et al., 2010; Kafian et al., 2020; Li et al., 2021).

In this context, the purpose of this doctoral project is to study the use of multiple Bessel and Gaussian light-sheet fluorescence excitations for a large field of view multicolor imaging implementation. For that, a multicolor Bessel LSM system under the Digitally Scanned Light-Sheet Microscopy (DSLMS) configuration was implemented. The system uses three Bessel beams for multi-fluorescence excitation to achieve quasi-simultaneous multicolor imaging with good optical sectioning and large FOV. A single axicon and a single spatial filter combination produced the three different-wavelength Bessel beams with more extensive and homogeneous light sheets. The beams are sequentially turned on and off synchronously with a single-camera acquisition frame rate achieving the quasi-simultaneous acquisition of the three fluorescent images. A detailed characterization of the Bessel beams and their multicolor LSM performance is compared with two Gaussian beams-based LSM configurations (DSLMS and SPIM). The implications on the effective FOV for the multiple color-Bessel and -Gaussian excitation light sheets are discussed when they are implemented under the same excitation path (i.e., the same excitation objective), as commonly implemented elsewhere for single-color light-sheets excitations (Olarde et al., 2012; Fahrbach, Gurchenkov, et al., 2013b; Fahrbach, Voigt, et al., 2013; Andilla et al., 2017; Müllenbroich, Turrini, et al., 2018; Xiong et al., 2020). Therefore, this study complements previous comparative studies between Gaussian and Bessel LSM configurations that only discussed monochromatic (or different colors but not simultaneous) excitation (Andilla et al., 2017; Remacha et al., 2020). The main goal of this work is to highlight the benefits of using multicolor Bessel LSM for large FOV imaging compared to Gaussian-LSM.

The feasibility of the multi-Bessel/Gaussian LSFM scheme is demonstrated by acquiring 2D and 3D images of non-melanized perithecia of the filamentous fungus *Sordaria macrospora*.

1.2 Hypothesis

Using multicolor Bessel beams in DSLM will improve the axial resolution in multi-fluorescence large FOV imaging compared to Gaussian beam-based LSFM (DSLM-Gaussian and o SPIM) configurations.

1.3. Objective

The main objective of this work is to implement a multi-fluorescence light-sheet microscopy platform to study the overall multicolor imaging performance using Bessel and Gaussian beams excitation.

1.4 Thesis structure

This dissertation comprises five chapters and is structured as follows:

Chapter 1 presents the dissertation's introduction. It provides general information about LSFM using different beam excitation configurations, emphasizing the advantages and limitations of using both Bessel and Gaussian beams to generate the light sheet. The hypothesis, objective, and thesis structure are also presented.

Chapter 2 contains the theoretical concepts essential to understand how the experimental system is designed and to comprehend the project results and discussions. Basic concepts of Bessel and Gaussian beams and general definitions of the terminology utilized such as the field of view, the lateral and axial resolution, the depth of field, and the point spread function are presented. The beam propagation theory used to simulate the different light sheets and the fluorescence process is also briefly explained. Finally,

since this thesis's principal biological sample is *Sordaria Macrospora*, a brief description of this model organism is presented.

Chapter 3 describes the experimental methods utilized in this work. The chapter starts by explaining how an axicon generates Bessel beams. Then, the multicolor LSFM setup is described using the Gaussian and Bessel beams-based LSFM configurations (SPIM-Gaussian, DSLM-Gaussian, and DSLM- Bessel). The computational methods to acquire and process the images taken in the experiments and simulations of Gaussian and Bessel beams propagation are also presented. The chapter ends by describing the samples utilized to characterize the light sheets, the optical resolution, and the biological samples preparation method.

Chapter 4 presents the results and discussions obtained in this doctoral project. First, the different color Bessel beam formation using an axicon is characterized experimentally and supported with numerical simulations. Then, the characterization for each LSFM configuration (DSLM- Bessel, DSLM-Gaussian, and SPIM-Gaussian) is described. Here, the multicolor FoV, optical sectioning, optical sectioning vs. FoV ratio, and the lateral and axial resolution are discussed, considering the effects produced in the final LSFM images due to the chromatic light-sheet shifts and beam types. To show the differences between DSLM- Bessel and -Gaussian imaging, biological samples of *Sordaria macrospora* are utilized. Finally, the results of simulating Bessel and Gaussian beams for light-sheet microscopy excitation using the same excitation objective are presented and discussed for the cases when the same FOV or NA is utilized.

Chapter 5 includes the conclusions derived from this work.

Chapter 2. Fundamental Theory

This chapter defines the basic concepts of Bessel, and Gaussian beams and the terminology utilized throughout this thesis, including the field of view, the lateral and axial resolution, the depth of field, the point spread function, etc. The beam propagation theory used to simulate the different light sheets and the fluorescence process is also briefly explained. Finally, a brief description of the model organism *Sordaria macrospora* is presented.

2.1 Transverse laser beam profiles

Lasers are the light sources commonly employed to generate the light sheet used in LSFM. Most lasers emit highly monochromatic beams, with transverse Gaussian intensity profile (depicted in **Figure 1a**); therefore, it is described mathematically by a Gaussian function (Power & Huisken, 2017). These beams are diverging beams and do not maintain the same width as they propagate. They only present a uniform intensity and phase distribution at the so-called beam waist, described below (Alda et al., 2003; Garcia-ortiz et al., 2017).

In contrast to Gaussian beams, there are “non-conventional beams” that propagate without changing their transverse profile over a relatively extensive range. One of them is the so-called Bessel beam which is a structured light beam generated by the interference of planes waves converging through a cone. Structured light is derived from the ability to tailor light, usually referring to the spatial control of its amplitude, phase, and polarization. Bessel beams are “non-diffracting” light with self-healing properties, and with an intensity profile mathematically described by the Bessel function (McGloin & Dholakia, 2005) (see **Figure 1b** and **equation (5)**). In LSFM, non-diffracting Bessel beams are desirable for imaging tissue and scattering biological samples (Fahrbach et al., 2010). Nowadays, there are several types of structured light; however, the current work was based on Bessel and Gaussian beams, as described below.

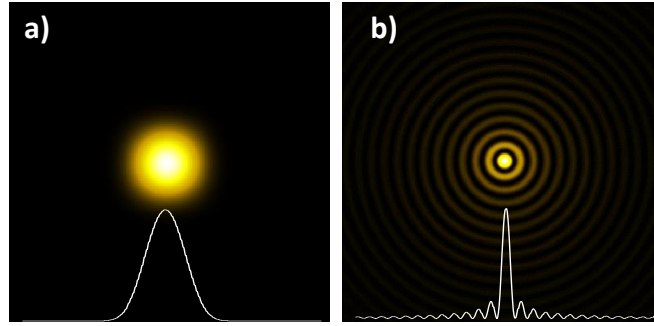


Figure 1 Gaussian and Bessel beams profiles. (a) Gaussian beam and (b) Bessel beam.

2.2 Gaussian beams.

Mathematically, Gaussian beams are one of the solutions to the paraxial wave equation. The equation for the two-dimensional electric field propagation along z can be found elsewhere (Alda et al., 2003; Garcia-ortiz et al., 2017) and is expressed as:

$$E(r, z) = A_0 \sqrt{\frac{w_0}{w(z)}} \exp\left(\frac{-r^2}{w(z)^2}\right) \exp\left[-i\left(kz + k \frac{r^2}{2R(z)} - \varphi(z)\right)\right], \quad (1)$$

where r is the radial component of the electric field, $w(z)$ is the beam width or radius (at $1/e$ field amplitude or $1/e^2$ of the Intensity), and $R(z)$ is known as the radius of curvature of the wavefront of the Gaussian beam. A_0 and w_0 are the field amplitude and the beam waist at the origin ($z = 0$), respectively. The free-space wavenumber is denoted by $k = 2\pi/\lambda$, where λ is the wavelength and, $\varphi(z)$ is the 2D Gouy phase shift.

The beam radius $w(z)$ is a function of the propagation coordinate z . This dependence is extracted from the evolution of the amplitude distribution and can be expressed as:

$$w(z) = w_0 \sqrt{1 + \left(\frac{z\lambda}{\pi w_0^2}\right)^2}, \quad (2)$$

The graphical representation of the beam radius along the propagation axis z is plotted in **Figure 2a**. At the beam's waist, it reaches a minimum ($w(0) = w_0$), but it becomes an infinite beam radius at infinite distances instead. Note that the divergence angle, defined as $\theta \approx \frac{\lambda}{\pi w_0}$, describes the spreading of the beam, and when z tends to infinity, the beam spreads asymptotically.

The radius of curvature $R(z)$ also depends on z and is expressed as:

$$R(z) = z \sqrt{1 + \left(\frac{\pi w_0^2}{z\lambda}\right)^2}, \quad (3)$$

Like the beam radius, when z tends to infinity, the radius of curvature in equation (3) presents a linear variation with z , representing a spherical wavefront originated at $z = 0$. However, the radius of curvature is infinite at the beam waist position, meaning that at the beam waist, the wavefront is plane.

Finally, the distance along z where the beam with radius is $\sqrt{2}$ times larger than the beam waist w_0 , is an important parameter known as the Rayleigh distance and is defined as:

$$z_R = \frac{\pi w_0^2}{\lambda}, \quad (4)$$

Notice that when $z = z_R$, there is one-half of the beam peak intensity (at $z = 0$), and the distance between the negative and positive Rayleigh distances, $z = \pm z_R$, is the so-called the *confocal parameter* or *depth of focus* of a Gaussian beam.

It should be noted that the beam radius, the radius of curvature, the divergence angle, and the Rayleigh ranges depend on λ . Therefore, Gaussian beams parameters evolve differently for different wavelengths during propagation.

2.2.1 Depth of focus of Gaussian beams is the depth of field of an optical system

It is worth emphasizing that the depth of focus definition for Gaussian beams is not technically the depth of focus of an optical imaging system but rather its depth of field. For "single lens" imaging systems, like those in photography or microscopy, the depth of focus is the distance between the camera's lens and its sensor (see **Figure 2b**). To keep the image focused, the sensor should be located at the principal image plane of the optical image system (i.e., at the film plane in traditional SRL cameras). It is related on how the image focus changes when the sensor is moved back and forth off the image plane. In contrast, the depth of field has to do with how the image focus changes when the object moves closer and farther from the front focal plane while keeping the camera sensor at the image plane (Liu & Hua, 2011). In other words, the depth of field is the optical system's distance range to maintain the desired amount of image quality (in terms of spatial frequency and contrast). Therefore, the confocal parameter definition is more likely the depth of field definition of an optical system and will be used in this work to define the light sheet thickness homogeneity and LSFM field of view.

2.3 Bessel beams

Bessel beams are an exact solution to the Helmholtz equation proposed by Durnin in 1987 (Durnin et al., 1987). The electric field of a theoretical Bessel beam is given by (McGloin & Dholakia, 2005):

$$E(r, \phi, z) = A_0 \exp(ik_z z) J_n(k_r r) \exp[\pm in\phi], \quad (5)$$

Where A_0 is the field amplitude, k_z and k_r are the longitudinal and radial wavevectors, J_n is the Bessel function of n -th order, r , ϕ and z are the radial and azimuthal and longitudinal components, respectively. The zero-order Bessel beams ($n = 0$) have a transverse profile whose center is a bright spot surrounded by infinite concentric rings of decreasing peak energy but distributed equally between the rings, as shown in **Figure 1b**. Higher-order Bessel beams ($n > 0$) have zero amplitude on the central region; the hole size increases as the Bessel order increases (McGloin & Dholakia, 2005). The present work utilizes zero-order Bessel beams.

It is important to emphasize that a Bessel beam is a mathematical idealization impossible to recreate experimentally. For an “ideal Bessel” beam simulation, the propagation intensity along z is described by $I(x, y, z \geq 0) = I(x, y)$, which represents a cross-section of the unchanged beam as it propagates, i.e., it is considered propagation invariant or invariant over distance (and time) and is “diffraction-free.” Therefore, an ideal Bessel beam needs infinite energy (Durnin et al., 1987).

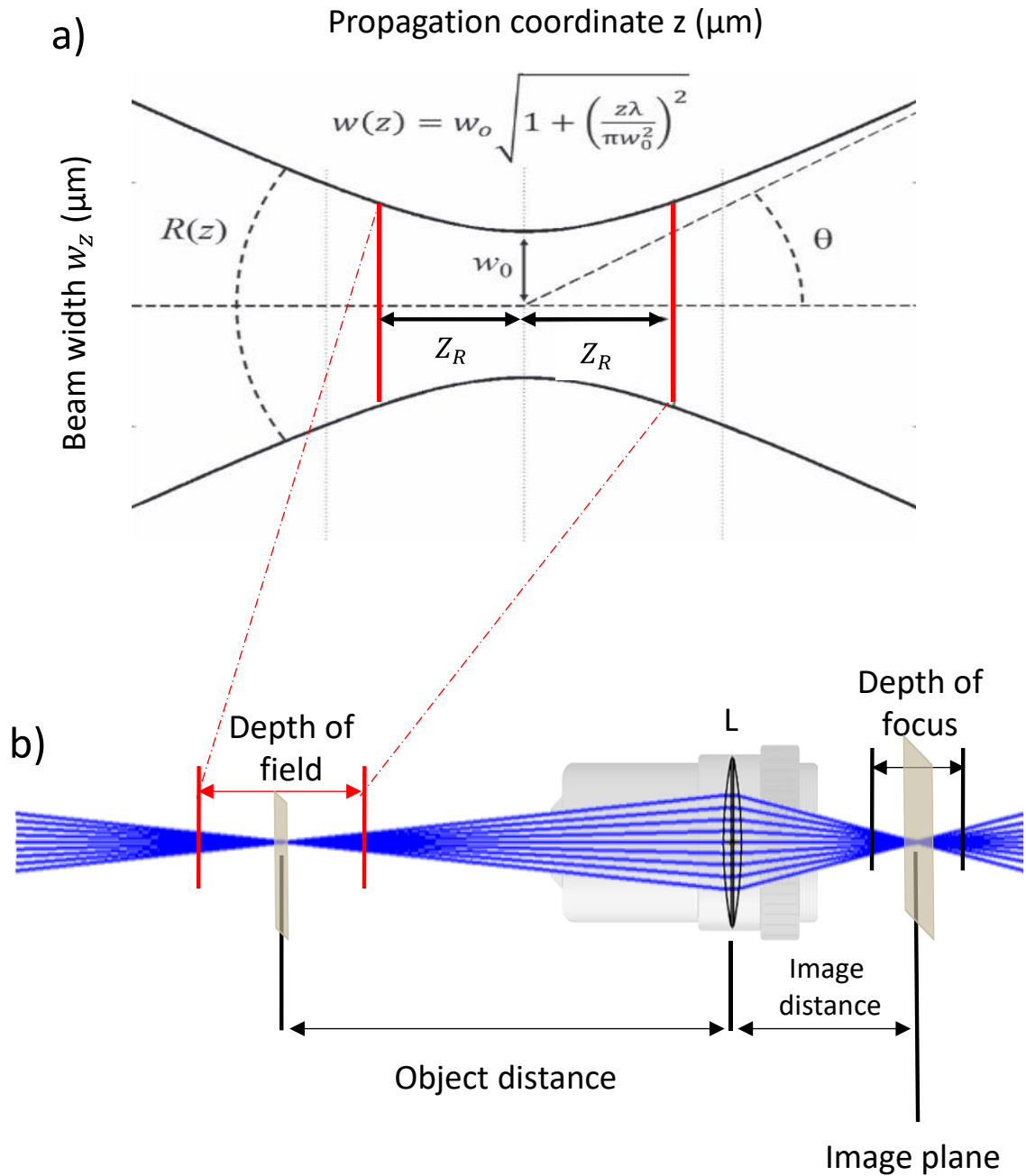


Figure 2 Gaussian beam propagation as a function of the propagation coordinate z . a) Beam width of a Gaussian beam as a function of the propagation coordinate z , The beam waist w_0 , Rayleigh range Z_R , divergence angle θ and the radius of curvature $R(z)$, the image is a modified version of Figure 1 from (Garcia-ortiz et al., 2017). b) Depth of field and depth of focus from a lens (L).

Such an ideal Bessel beam cannot be generated experimentally, and all the generation methods can only create beams with a limited propagation length (Z_{max}). Although the ideal Bessel does not exist, the experimental Bessel beams have been widely applied in biology manipulation as optical tweezers (McGloin & Dholakia, 2005), among other applications (Khonina et al., 2020). In addition, Bessel beams have self-healing properties that allow its reconstruction beyond obstructions placed in their path propagation, making them desirable as an illumination source in Light-Sheet Microscopy (Mazilu et al., 2010; Olarte et al., 2012; Fahrbach, Gurchenkov, et al., 2013a; Gao et al., 2014). Next, the generation of these Bessel beams and the non-diffracting and reconstructing properties are described.

2.3.1 Bessel beams generation

In practice, Bessel beams are generated by the interference of plane waves with rotational symmetry. The simplest method to generate a Bessel beam involves the use of an annulus mask with a diameter d and a small width (Δd) localized at the focal distance (f) of the lens with a radius R (Durnin et al., 1987). In this way, a conical wavefront is generated after the lens, and these waves interfere to produce a Bessel beam (see **Figure 3**).

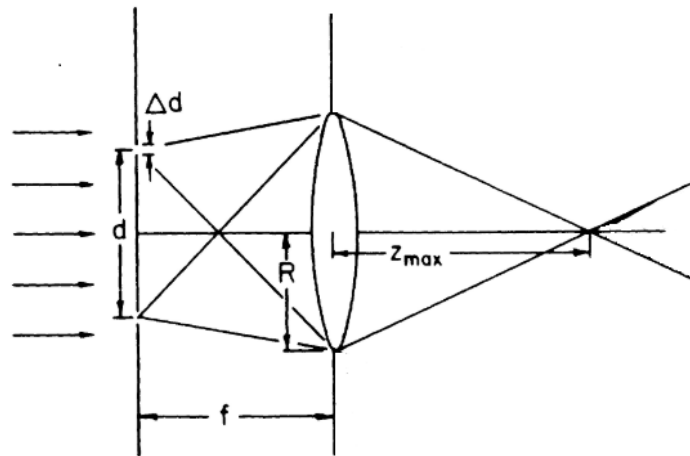


Figure 3 Experimental arrangement to create a zero-order Bessel beam. The image is a modified version of Figure 2 from (Durnin et al., 1987).

The maximum propagation distance is given by $Z_{max} = R/\tan\theta$, where $\theta = \tan^{-1}(d/2f)$, and the Rayleigh range for a Bessel beam generated for this method can be approximated as (Duocastella & Arnold, 2012)

$$Z_{RBessel} \approx \frac{\pi 2Rr_0}{4\lambda}, \quad (6)$$

Here, r_0 is the central lobe size of the beam, which is the radial distance from the core (central lobe intensity) to the first minimum intensity and can be approximated as (McGloin & Dholakia, 2005)

$$r_0 \approx \frac{2.405}{kn\sin\theta}, \quad (7)$$

where the value 2.405 is derived from the first root of the zeroth-order Bessel function. The n is the refraction index of the medium where the beam propagates and the r_0 is the equivalent of the Gaussian beam waist (w_0) and is usually much smaller than R .

Notice, however, that generating a Bessel beam using an annulus mask is inefficient since most light is blocked or absorbed by the mask. A more efficient way to generate a Bessel beam is to use a conical lens known as an axicon, which only changes the direction of light passing through it without changing the amplitude of the incident wave, depending on the axicon angle τ (see **Figure 4**). Here, in contrast to the ring mask method, the maximum propagation distance over which the Bessel beam propagates depends on the incident beam radius r being $Z_{max} = r / \tan \alpha_0$, so that the minimum radio is also calculated by the same equation (7) but using the angle α_0 instead.

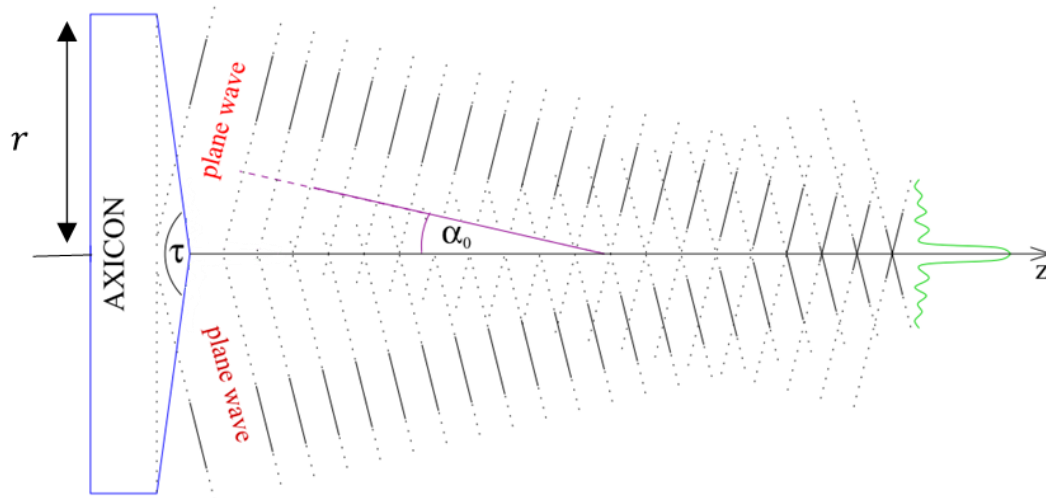


Figure 4 The demonstration of Bessel beam generation using an axicon prism (Cizmar, 2006).

2.3.2 Bessel beams self-reconstruction property

Bessel beams possess the self-reconstruction property (McGloin & Dholakia, 2005; Fahrbach, Gurchenkov, et al., 2013b). When an object is placed at the center of the beam, the outer converging waves that create the beam can interfere despite the obstruction. The interference will reconstruct the intensity of the profile beyond such a block. The minimal distance which the beam can self-reconstructed after the obstacle is given by

$$Z_{min} \approx \frac{ak}{2k_z}, \quad (8)$$

where a is the obstruction width measured from the center beam.

The self-reconstructing effect can be seen in **Figure 5**. The figure shows an xz-plane of a Bessel beam propagating from left to right. The axicon that creates the beam is traced in a yellow line at the hard left of the figure. Note how the intensity of the Bessel beam is reconstructed even after encountering an obstruction depicted by the green circle. It can be appreciated from the figure that the reconstruction is due to the conical wavefronts of the beam.

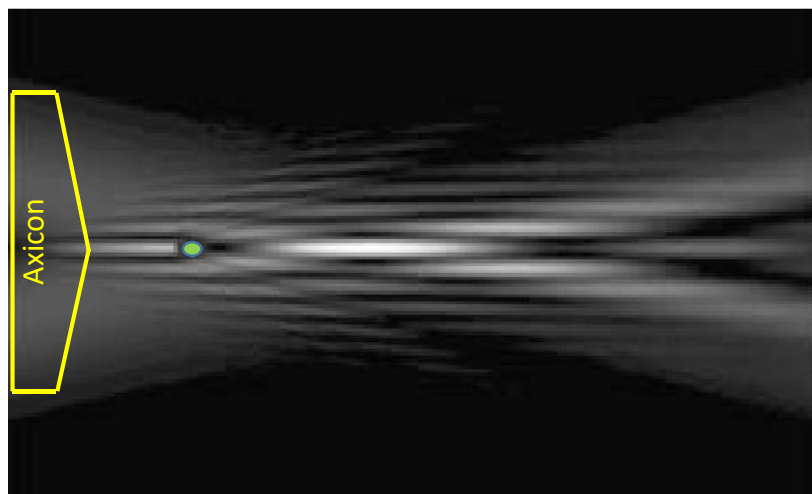


Figure 5 Bessel beam reconstruction. The figure shows a cross-section of the Bessel beam as it propagates from left to right. The intensity profile of the Bessel beam is seen to reform even after encountering an obstruction (green circle). The image is a modified version of Figure 3 from (McGloin & Dholakia, 2005).

2.4 Light Sheet Fluorescence Microscopy

Light Sheet Fluorescence Microscopy (LSFM) is an imaging technique that utilizes a thin light sheet to illuminate a single thin section of the sample at one time to reduce the out-of-focus signal (Power & Huisken, 2017; Olarte et al., 2018). Compared to confocal laser scanning microscopy (CLSM), LSFM reduce photobleaching in the sample and possesses higher acquisition rates, making light-sheet microscopy desirable for long-term imaging studies. Another LSFM advantage is its design flexibility to be easily adapted to visualize various specimens' sizes, from single-cell structures (Hoyer et al., 2016) to rat brains (Stefaniuk et al., 2016). In contrast to CLSM, LSFM allows volumetric imaging over many length scales at a high spatial resolution.

A complete history of the LSFM technique is published in detail in "The light-sheet microscopy revolution" (Girkin & Carvalho, 2018) and it is briefly summarized here. The light-sheet microscopy technique was first introduced in 1903 by Richard Zsigmondy and Henry Siedentopf (Siedentopf & Zsigmondy, 1903) to visualize gold particles in colloidal solutions, using a high-intensity sheet of non-coherent light to visualize the scattered signal from such sub-micrometer particles (Siedentopf & Zsigmondy, 1903). It took several years for light-sheet microscopy to switch to coherent light to generate fluorescence imaging. In 1993 the first 3D reconstruction of a fully cleared and stained guinea pig cochlea using a fluorescence light sheet (named at the time "orthogonal-plane fluorescence optical sectioning technique") was published (Voie et al., 1993). However, it took decades for the scientific community to become interested in this technique. In 2004, Huisken *et al.* implemented LSFM under a selective plane illumination microscopy (SPIM) scheme. SPIM allowed visualizing *in vivo* a Medaka's fish heart and *Drosophila melanogaster* embryogenesis (Huisken et al., 2004).

Since then, the use of SPIM has been applied in different areas of biology. Nowadays, many groups around the globe have contributed to this technique, and in Mexico, the first LSFM system was implemented at CICESE. The light sheet microscope at CICESE has demonstrated its application in different areas of biology and materials characterization (Can-Uc et al., 2018; Licea-Rodriguez et al., 2019; Alejandra et al., 2021; Barrón Ortiz, 2021; Luna-Palacios et al., 2022). So far, the LSFM in CICESE has worked in the SPIM modality. However, as already mentioned, using a cylindrical lens has some limitations. First, the optical sectioning is poor when it is desired to observe organisms smaller than 15 μm as *Neurospora crassa* (Licea-Rodriguez et al., 2019). Second, shadowing artifacts are notorious when images are taken for large samples such as brains (Alejandra et al., 2021). Therefore, DSLM implementation was essential for our group to obtain images with better optical sectioning and increase the images' quality. In addition, as demonstrated in this

dissertation, the self-healing properties of Bessel beams make it possible to have larger and colocalized FOVs which is essential for large samples imaging. As mentioned above, the chromatic properties of the objectives is sometimes not considered. Despite this, it is emphasized that this is a latent problem for the new implementation of LSFM with limited optical components.

2.4.1 Different LSFM arrangements (SPIM, DSLM).

It is possible to implement LSFM by using two primary arrangements which differ in how the light sheet is formed. The first method is the so-called Selective Plane Illumination Microscopy, SPIM for short, which uses a cylindrical lens to focus a Gaussian beam onto the sample. The second method is the Digitally Scanned Light-sheet Microscopy or DSLM, which uses galvanometric mirrors located at the image plane of the back focal plane of the illumination objective creating a "virtual light-sheet". The fluorescence signal is detected at 90 degrees from the illuminated plane using an objective microscope, filter, tube lens, and CMOS camera, as depicted in **Figure 6**.

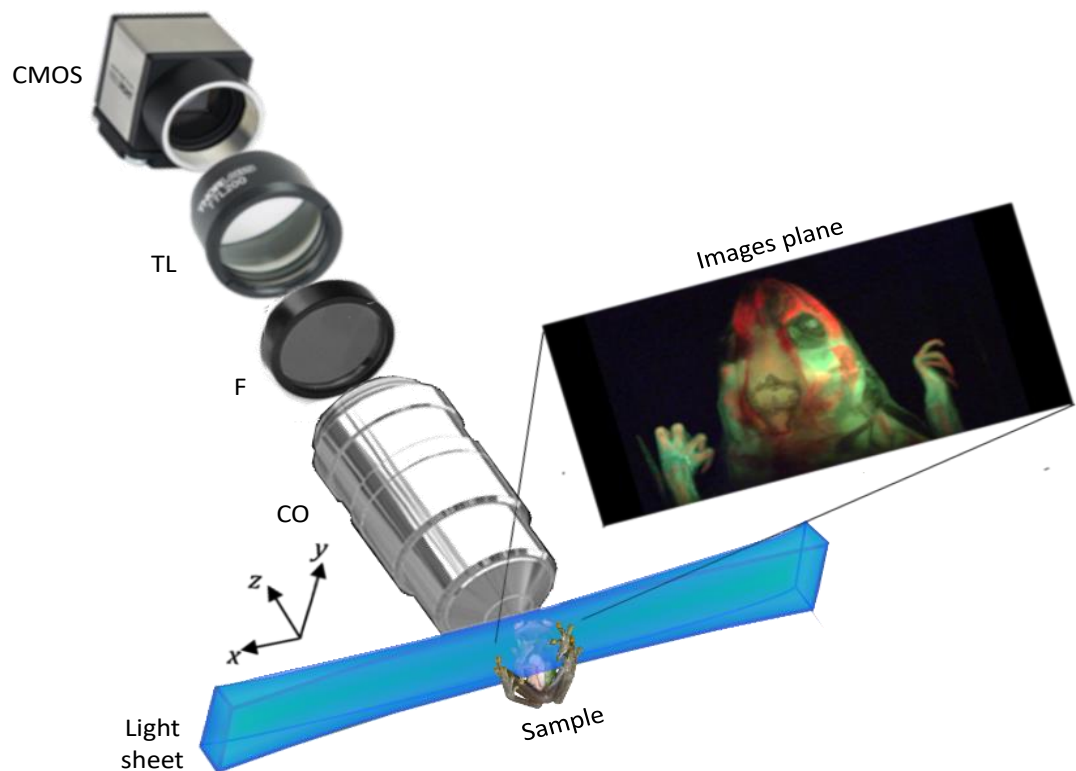


Figure 6 General LSFM configuration; CO, collection objective; F, filter; TL, tube lens; CMOS, camera; and xyz, laboratory coordinate system.

Each illumination method has its positive and negative aspects; SPIM does not need moving parts to generate the light sheet, and the images can be produced at high-speed. However, high-power lasers are necessary to distribute the intensity along the sheet volume, and the shadowing artifacts are notorious in the images, reducing the image quality. In contrast, DSLM can choose different beam types to generate the light sheet, from Gaussian beams (the most common) to more sophisticated structured light like Bessel or Airy beams, which minimize shadowing artifacts (Gao et al., 2014; Vettenburg et al., 2014).

SPIM

SPIM's principal characteristic is that the light sheet is generated using a cylindrical lens and a collimated Gaussian beam passing through it. As shown in **Figure 7**, the light plane, formed between the (positive and negative) Rayleigh ranges of the focused beam, is imaged by the orthogonally placed detection objective. Notice that because the collection and the excitation arms are uncoupled, the position of the light sheet can be shaped and positioned independently of the collection objective with different numerical apertures (NA) and working distances.

The sample is placed at the intersection of the illumination- and the detection-optical axes. Note that the light-sheet illuminates the specimen from one side, exciting fluorescence at a specific sample plane. Then, the signal is collected by the detection objective, which projects the fluorescent image onto a CMOS camera. For 3D image generation, an image stack taken at different sample planes is performed by moving the sample along the z-axis of the detected object. After the stacks are taken, the 3D images are computationally reconstructed. Meanwhile, for 2D images at a single sample plane, i. e. without depth scanning, rapid videos as fast as the camera frame rate can be taken to study the dynamics of biological samples.

Although SPIM has proven to be a good technique for studying biological phenomena, there are some limiting drawbacks of illuminating an entire plane at once from the side. For instance, the presence of striped artifacts in the resulting data, which arise from refraction, scattering, absorption, or loss of a significant fraction of illumination, affects the height and thickness of the light sheet.

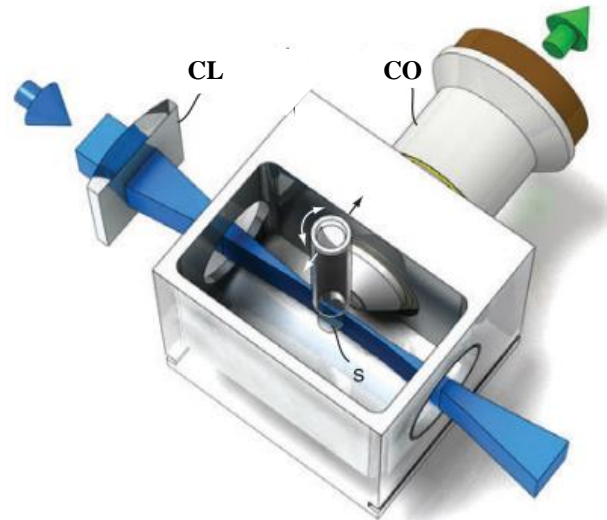


Figure 7 SPIM diagram. A single cylindrical lens (CL) is used to form the light-sheet inside to sample (S); the collection objective (CO) collects the fluorescent image at a determined sample plane. Image adapted from (Huisken & Stainier, 2009).

DSLIM

Digital Scanning Light-sheet Microscopy, known as DSLM, is another method to generate the light-sheet and was proposed by Keller *et al.*, in 2008. In contrast to SPIM, a focused beam is scanned rapidly vertically through the sample. Scanning mirrors or galvanometric mirrors are used to scan the beam generating a "virtual light sheet." The oscillation of these mirrors is at least two times faster than the images acquisition rate (< 100 Hz)(Keller & Stelzer, 2008). For DSLM, it is necessary to add a conjugated plane system using two lenses: a scanning lens and a tube lens behind the excitation objective (EO) (see **Figure 8**). In DSLM, the EO typically has a lower NA than the collection objective (CO) (Power & Huisken, 2017).

DSLIM has vital advantages over SPIM. First, the shadowing artifacts are minimized because the scanned beam cannot interfere with coherent photons between neighboring regions in the sample, reducing the speckle and shadows (Keller & Stelzer, 2008; Power & Huisken, 2017). In addition, DSLM has higher illumination efficiency; the power of the light is concentrated in only one line in the sample at a given time so that the sample is better excited at lower exposition times. It also increases the signal-to-noise ratio and reduces the photodamage (Power & Huisken, 2017). DSLM's light source power requirements are lower than SPIM because the former requires the power of a single line to generate a plane by scanning the line, having a light sheet more homogeneous in intensity. It is worth mentioning that using DSLM is more possible to carry out two-photon excitation experiments than SPIM; because DSLM concentrates

more energy in a single light line. This line is scanned afterward to generate the light sheet which inherits the energy of the single line all over the plane. Finally, the adaptation of structured beams such as Bessel beams is possible due to DSLM configuration.

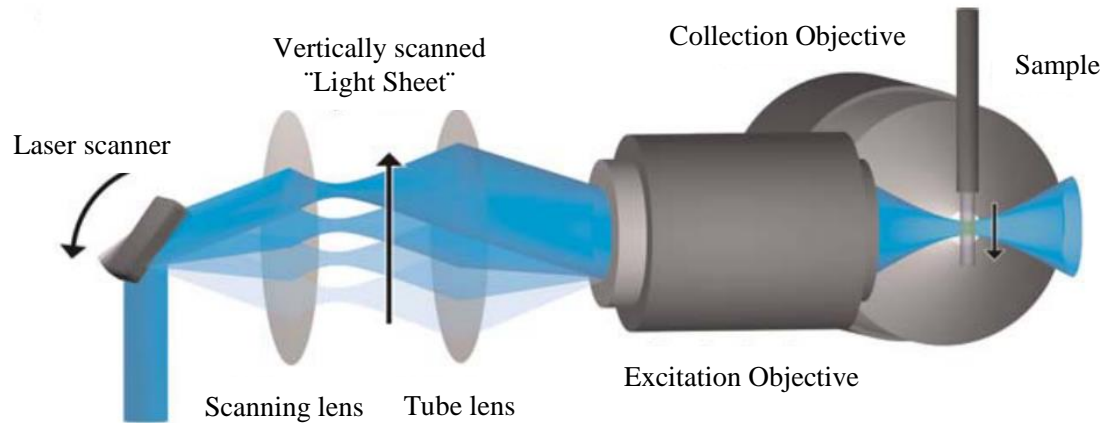


Figure 8 DSLM diagram. A galvanometric mirror oscillates at the Nyquist frequency vertically along the sample forming a virtual light sheet. A conjugated plane lens is used to pivot the laser into the back focal aperture of the objective excitation. Figure modified and taken from (Keller et al., 2011).

To give an idea of LSFM performance over other similar imaging techniques, a brief comparison of standard parameters in DSLM, confocal, and two-photon microscopy is shown in **Table 1** (Keller & Stelzer, 2008).

Table 1. Performance comparison of DSLM with other fluorescence microscopies

Parameters	DSLM	Confocal	Two-photon
Energy ^a	E	$\sim 10^3 \cdot E$	$\sim 10^6 \cdot E$
Lateral resolution	r	$r/\sqrt{2}$	$r \cdot \sqrt{2}$
Axial resolution ^b	$\sim 5 \mu m$	$\sim 10 \mu m$	$\sim 18 \mu m$
Acquisition rate	63 Mpixel/s	2-6 Mpixel/s	1 Mpixel/s
Signal-to-noise ratio	1000:1	60:1	10:1
Cost efficiency ^c	$\geq 70K$ US\$ ^d	$\geq 100K$ US\$	$\geq 200K$ US\$

E is the energy for a single plane to get the images ($1.7 \mu m$ at 488 nm). r is the lateral resolution calculated using $\frac{0.61\lambda}{NA}$ and without the deconvolution process. When the images are deconvolved, DSLM lateral resolution is theoretically equal to confocal microscopy's lateral resolution. ^a Considered for taking images of entire zebrafish embryos (Keller et al., 2008). ^b the axial resolution was obtained using beads with a diameter of $1 \mu m$ and a CO 10x with NA 0.3 (Engelbrecht & Stelzer, 2006) ^c "Considering costs for additional optical components in confocal and two-photon microscopes and the costs for high-performance lasers (particularly for two-photon microscopes)" (Keller & Stelzer, 2008). ^d Considering the costs of a single high-performing CMOS camera and additional optical components. The table was extracted from (Keller & Stelzer, 2008).

The table shows that DSLM has several advantages over other microscopy techniques. For instance, the light energy to get a single plane is three and six orders of magnitude less than for confocal and two-

photon microscopy, respectively. Also, the acquisition rate is about ten times higher than in confocal and two-photon microscopy. Finally, better axial resolution performance is achieved using DSLM, which could be improved by at least 50% compared to than the other microscopies (for a CO 10x with NA 0.3) (Engelbrecht & Stelzer, 2006).

2.4.2 LSMF parameters

In LSMF, three principal parameters characterize the light sheet and the system: lateral resolution, optical sectioning (axial resolution), and the field of view (FOV). **Figure 9** illustrates such three parameters for better understanding.

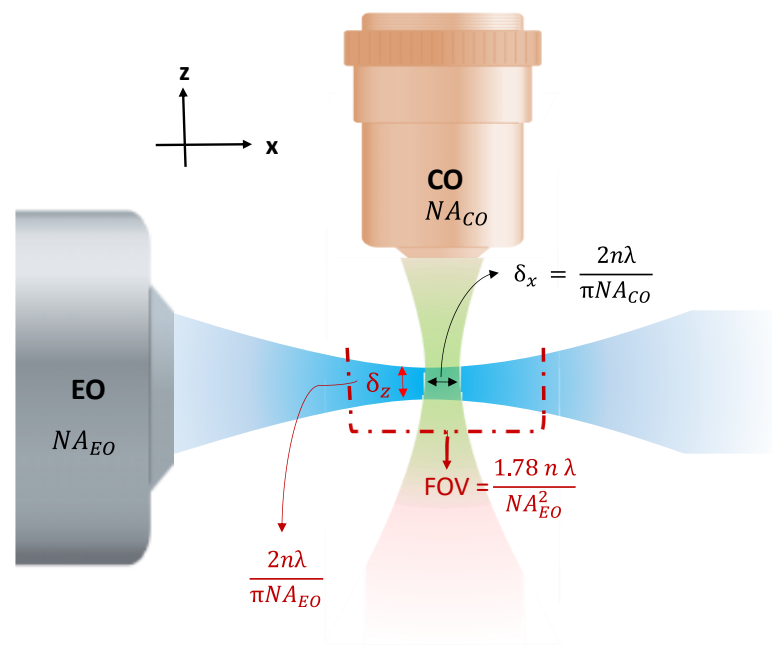


Figure 9 Three LSMF important parameters. The image represents the top view of an LSMF. EO, excitation objective, CO collection objective, NA_{EO} numerical Aperture from EO, NA_{CO} numerical Aperture from CO, n refraction index of the sample. The excitation beam (blue). The collection beam (green). The dotted lines indicate the field of view of the sheet. The red arrow the axial resolution or the optical sectioning (δ_z). The black arrow the lateral resolution for LSMF (δ_x).

Lateral resolution

The lateral resolution of LSFM is dictated by the collection objective as

$$\delta_x = \frac{2n\lambda_e}{\pi NA_{CO}}, \quad (9)$$

In other words, just as in epifluorescence microscopy, the lateral resolution depends on the NA of the collection objective (NA_{CO}) and the fluorescence emission wavelength (λ_e) coming from the sample and its refraction index. Notice that the lateral resolution depends on more factors, such as contrast, noise, and sampling. However, for LSFM, it is slightly better because of the improved image contrast due to the fluorescence coming selectively from a thin plane of the sample (Huisken & Stainier, 2009).

Optical sectioning

Optical sectioning in LSFM is the ability to section a sample along the z-axis and is related to the thickness of the light sheet. When Gaussian beams are used to generate the light sheet, the thickness is no other than the lateral resolution of the excitation objective (EO)

$$\delta_z = \frac{2n\lambda_i}{\pi NA_{EO}} = \frac{2n\lambda_i f}{\pi D}, \quad (10)$$

Here, λ_i is the excitation wavelength, NA_{EO} is the EO numerical aperture, f is the EO focal length, and D is the input beam diameter at the back focal aperture of the EO. Notice that the EO back focal aperture is not illuminated in the totality in the practice so that the final δ_z may vary depending on the size of the input beam. Therefore, at a first approximation, the axial resolution in LSFM is the lateral resolution of the excitation objective (Olarie et al., 2018). But a more accurate definition of the axial resolution in LSFM is determined by the thickness of the light sheet and the point spread function of the collection objective (Engelbrecht & Stelzer, 2006).

Field of view

The FOV in LSFM is associated with the excitation objective's depth of field (DoF). For a Gaussian beam the DoF is defined in terms of the Rayleigh length as $DoF = 2 \times z_R$, where z_R is given by equation (4). It is the length where the minimum beam thickness ($2\omega_0$, at the beam focus) increases back and forth by a factor of $\sqrt{2}$ (see **Figure 2**). In practice, however, the FOV for LSFM is taken as the FWHM width of the focusing beam intensity profile along its propagation direction (x-direction) (Olarte et al., 2012, 2018; Remacha et al., 2020; Xiong et al., 2020); i.e., when seen from the collection objective's point of view. When a beam is focused through a lens, the focused intensity is modulated by a $sinc^2$. Therefore, considering the width at the FWHM of such a modulating function, a modified definition is obtained for the LSFM field of view FOV (Olarte et al., 2018).

$$FOV \approx 1.78 \frac{n\lambda_i}{NA_{EO}^2} = 1.78 \frac{\lambda_i n D^2}{f^2}, \quad (11)$$

For Gaussian beams, the excitation objective NA determines both the light sheet thickness and the FOV. If low NA is utilized for achieving a large FOV, the light-sheet thickness is widened, and, therefore, a low axial resolution is obtained in the LSFM system. In contrast, the FOV length is not ruled by equation (11) for the Bessel beams case. Instead, it depends on the beam annulus width formed at the EO back focal aperture (which creates the Bessel beam at the lens focal plane), as will be explain later.

2.4.3 LSFM drawbacks

There are different drawbacks in LSFM associated with the light's intrinsic properties utilized to form the light sheets.

First, there is a constant trade-off between the FOV and optical sectioning. Maintaining an extended FOV ($> 10 \mu\text{m}$) with a thin light sheet is a problem due to the rapid divergence of the Gaussian beams. Under such circumstances, axial resolutions better than $1 \mu\text{m}$ are challenging to achieve (Power & Huisken, 2017). While the short FOV achieved with Gaussian beams is typically employed (and possibly good enough) to

image subcellular structures, it is not ideal for large samples in all three dimensions without sacrificing axial resolution (Welf et al., 2017).

Another problem of LSFM is the striping patterns obtained in the image due to scattered structures present in the sample. Although DSLM minimizes such a problem, it continues since the Gaussian beams employed to form the light sheet are highly diffractive.

Also, when high numerical aperture objectives are required either in the collection (for high lateral resolution) or the excitation (for high axial resolution), the commonly short working distance requires consideration for the bulky CO and EO objectives do not physically overlap (Power & Huisken, 2017). Therefore, the optical design is limited when both the highest axial and lateral resolutions are desired.

The chromatic effect of the optics utilized in LSFM is also a problem when multiple lasers are used for the light sheet excitation. Colocalizing the FOV of different wavelengths is challenging and requires either adding extra optics or structured non-diffracting excitation beams (or both) to minimize such a chromatic problem, as shown later in this work.

2.5 Fluorescence

In general, the LSFM is based on detecting the fluorescence coming from the illuminated sample plane. Fluorescence is the spontaneous emission of a photon during the relaxation of molecules from an excited state. Fluorescence is the combination of three consecutive events that occur within the nanoseconds scale and are depicted in **Figure 10**.

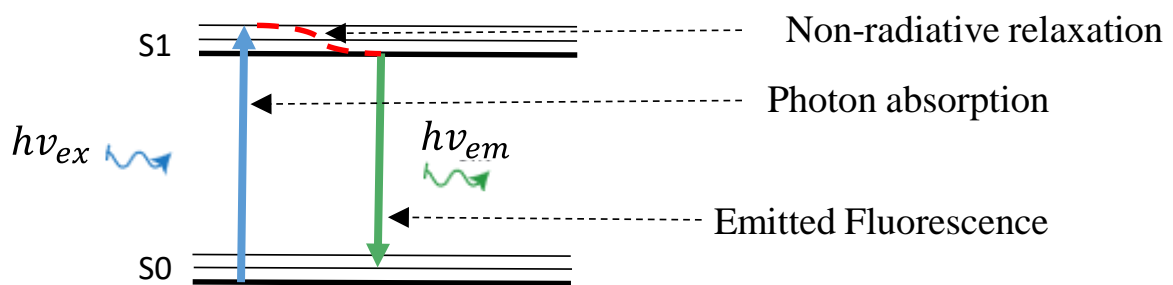


Figure 10 Jablonski diagram for a green fluorescent molecule. $h\nu_{ex}$ excitation light (ex) and $h\nu_{em}$ emission light. A molecule in state S0 absorbs energy from blue light (488 nm); this causes the molecule to pass to state S1. From S1, the molecule loses energy non-radiatively and emits a green photon (507 nm) when relaxing back to S0.

First, the molecule absorbs light energy (a photon with energy $h\nu_{ex}$) higher than the energy difference between the excited state (S_1) and the ground state (S_0); that is, $h\nu_{ex} > S_1 - S_0$. Second, once the molecule is at the excited state band, it relaxes to lower vibrational energy states within the excited band without radiating. Essentially, this non-radiative relaxation process transfers tiny amounts of energy through molecular or atomic collisions, resulting in the generation or transfer of heat energy, but does not cause the light emission of an infrared or visible photon. Third, the molecule returns to the ground state (S_0), emitting a photon with energy $h\nu_{em} < h\nu_{ex}$, i. e., with less than the energy necessary to pass to the excited state. The difference between the exciting and emitted energy, known as the Stokes shift, is the property that makes fluorescence a powerful effect in taking images. By filtering the excitation photon in the collection path, without blocking the emission photon, it is possible to see only the fluorescent objects.

2.5.1 Fluorochromes, photodamage, and photobleaching

A molecule capable of fluorescing is called a fluorochrome. However, there are few fluorochromes in nature, so the samples have to combine with specific labeling (Lichtman & Conchello, 2005), allowing the acquisition of signals from particular proteins, cells, or tissues. It is usually achieved by introducing fluorochrome (or fluorophores) from an external source (staining) or genetic encoding into the specimen's genome, an essential tool for *in vivo* imaging. Although fluorescence labeling has been tested as an excellent technique to take fluorescence images, the energetic difference between excitation and emitted photons is deposited on the sample, resulting in heat damage (photodamage). The heat production can also damage the fluorophore irreversibly, in a process known as photobleaching (Lichtman & Conchello, 2005; Olarte et al., 2018).

Photodamage and photobleaching are the main problems in fluorescence microscopy when taking long-time images. In confocal microscopy, for example, the illumination beam is not only present at focus within the sample; the exciting light that passes through the sample while the beam is focused also produces photodamage at the out-of-focus parts of the sample which are not observed. In that way, volumetric damage is induced. In contrast, in LSFM, the illumination is localized at a thin sample section, so the damage occurs only in the illumination plane, and the fluorescence signal is efficiently collected, maximizing the sample viability (Olarte et al., 2018).

2.6 Beam propagation

The propagation of light beams commonly utilized for the light sheet formation (Gaussian or Bessel, OE focal length, input diameter) can be modeled using the Huygens-Fresnel diffraction theory (Becker et al., 2019). The transversal beam (at a xy -plane) field at a determined distance (along the z -axis) is given by the Huygens-Fresnel integral equation in cartesian coordinates as

$$E(x, y, z) \cong -i \frac{e^{ikz} e^{\frac{ik(x^2+y^2)}{2z}}}{\lambda z} \iint E_0(x_0, y_0, z=0) e^{\frac{ik(x_0^2+y_0^2)}{2z}} e^{\frac{-k(xx_0+yy_0)}{z}} dx_0 dy_0 \quad (12)$$

Where $E(x, y, z)$ is the field propagated after a distance z , $E_0 = E(x_0, y_0, z=0)$ is input field in the input plane, and k is the wavevector.

Notice, however, that Gaussian and Bessel beams are azimuthally symmetric in the xy -plane along the z -axis; therefore, it is convenient to transform the Huygens-Fresnel integral to cylindrical coordinates. This transformation equations is found elsewhere (W. Goodman, 1996; Becker et al., 2019) and can be performed by defining φ , φ , $y_0 = r_0 \sin(\theta)$, $y = r \sin(\phi)$, with $r_0 = \sqrt{x_0^2 + y_0^2}$ and $r = \sqrt{x^2 + y^2}$ as the beam radius at $z=0$ and a specifics z , and θ the azimuthal angle at $z=0$ (see **Figure 11**).

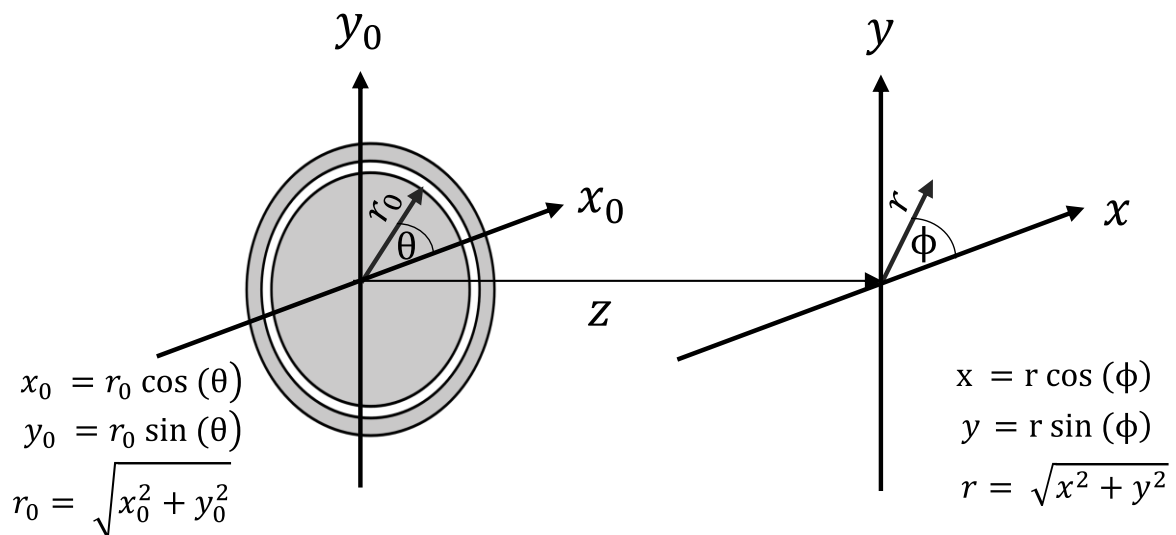


Figure 11 Cartesian coordinates to cylindrical coordinate's transformation.

After some algebraic steps equation (12) changes to

$$E(r, z) \cong \frac{-2\pi i e^{ikz} e^{\frac{ikr^2}{2z}}}{\lambda z} \int r_0 E_0(r_0, z=0) e^{\frac{ikr_0^2}{2z}} J_0\left(\frac{kr r_0}{z}\right) dr_0, \quad (13)$$

The field amplitude is now expressed as $E(r, z)$, where the incident field amplitude $E_0 = E(r_0)$ occurs at $z = 0$, and has an initial beam radius r_0 .

Equation (13) is used later in chapter 3 for simulating the free-space propagation of a focused (Bessel or Gaussian) beam. For that, it is necessary to multiply the field E_0 by the phase mask of a thin lens ($e^{\frac{ikr^2}{2f}}$); that is, at the beam field “immediately behind” resulting in the following expression (Brzobohatý et al., 2008):

$$E(r, z) \cong \frac{-2\pi i e^{ikz} e^{\frac{ikr^2}{2z}}}{\lambda z} \int r_0 E_0(r_0, z=0) e^{\frac{ikr_0^2}{2z}} e^{\frac{ikr^2}{2f}} J_0\left(\frac{kr r_0}{z}\right) dr_0, \quad (14)$$

where E_0 is the field at $z = 0$, and f is the focal length. **Figure 12** depicts the focused beam in cylindrical coordinates.

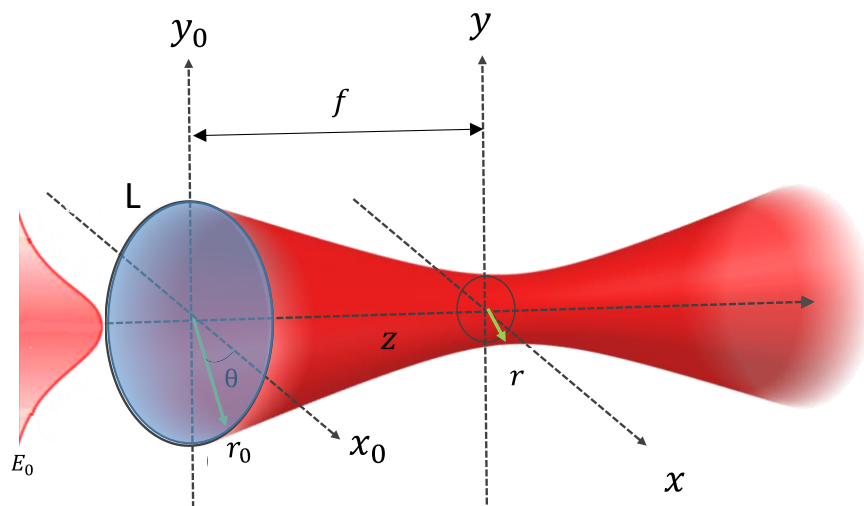


Figure 12 focusing beam in cylindrical coordinates.

2.7 *Sordaria macrospora*

Sordaria macrospora is a filamentous fungus that serves as a model system for understanding the development of perithecia (sexual fruiting bodies) in Ascomycetes. The success of *S. macrospora* as a model organism is due to easy and safe manipulation in the laboratory. Its life cycle is completed in seven days. It is homothallic, i.e., self-fertile, which means a single strain can produce fruiting bodies without a mating partner. *S. macrospora* is easily genetically tractable, and well-suited for large-scale genomic, transcriptomic and proteomic studies (Teichert et al., 2020).

The *S. macrospora* life cycle is shown in **Figure 13**; it starts with an ascospore (the only spores produced with a size about 28 μm long) which germinates and produces a mycelium, which after 2–3 days forms ascogonia, the female gametangia which are enveloped by sterile hyphae to generate spherical bodies with a size of about 20–55 μm . After 4–5 days, the mature fruiting bodies with an outer pigmented peridial membrane are differentiated (about 30–50 μm). After seven days, mature fruiting bodies are formed that discharge ascospores through the ostium at the tip of the perithecial neck (Engh et al., 2010; Teichert et al., 2014).

Although *S. macrospora* has been a model organism for over 25 years, little is known about molecular determinants for tissue differentiation inside the perithecium and the formation of the Dikaryon (i.e., a collection of cells with exactly two nuclei that are vital for meiosporangium formation) (Teichert et al., 2020). This is mainly because *S. macrospora* forms black fruiting bodies and ascospores, making the interior visualization challenging to reach by conventional microscopy techniques. In 2007 Engh *et al.* generated a mutant strain of *S. macrospora* capable of generating fruiting bodies without melanin, opening the door to monitoring its behavior.

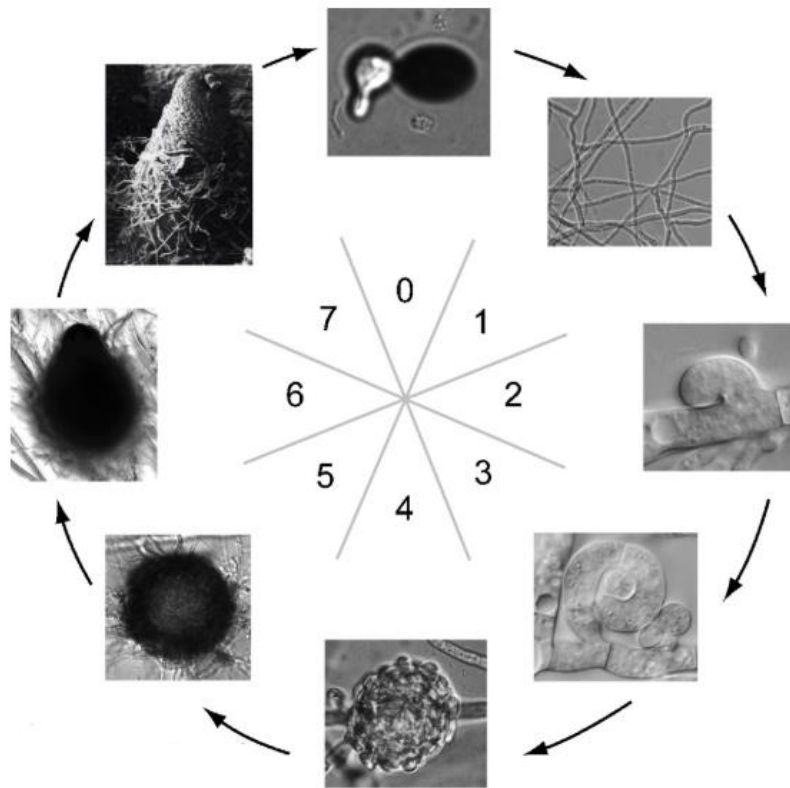


Figure 13 Life cycle of *Sordaria macrospora*. Figures represent different stages observed at different days of incubation (0 to 7 days). The final stage, the perithecium, is shown as a scanning electron micrograph. The figure was taken from (Engh et al., 2010).

Chapter 3. Methodology

This chapter describes the experimental methods utilized in this thesis project. The chapter starts by explaining the axicon properties of generating Bessel beams. Then, the multicolor Light Sheet Fluorescent Microscopy (LSFM) setup is described using three types of light sheets configurations (SPIM-Gaussian, DSLM-Gaussian, and DSLM- Bessel). The computational methods to acquire and process the images taken in the experiments and simulate Gaussian and Bessel beams are also boarded. Finally, the samples to characterize the light sheets and optical resolution and the preparation method of the biological samples are also presented.

3.1 Axicon lens

An axicon is a refracting cone lens with the property to refract all rays at the same angle relative to the optical axis. As depicted in **Figure 14**, when a collimated Gaussian beam passes through the axicon, the linear superposition of all the beam rays gives rise to a transverse intensity profile in the form of a Bessel function (Brzobohatý et al., 2008). As a result of such self-diffraction process, the Bessel beam intensity varies over the axial range of the beam's propagation, forming a bright ring at large propagation distances that decreases as z increases (Y. Zhang, 2007). The uniform intensity distribution along the z -axis has a limited range given by (Brzobohatý et al., 2008).

$$Z_{max} = rcot\alpha_0 , \quad (15)$$

Where r is the beam radius of the incident beam and α_0 is the axicon semi-apex angle described by

$$\alpha_0 = \arcsin\left(\frac{n}{n_0} \cos \frac{\tau}{2}\right) + \frac{\tau - \pi}{2} , \quad (16)$$

Where n and n_0 are the axicon refractive index and the media refractive index around it, respectively; while τ is the axicon apex angle (see **Figure 14**). The semi-apex angle is the refraction angle of the

wavevectors of the plane waves with the z axis (see **Figure 14**) (Brzobohatý et al., 2008). In the experiments presented here, the incident beams diameters are 7.8 mm, 8.1 mm, and 8.2 mm for 445 nm, 488 nm, and 561 nm, respectively. The axicon factory specifications are: model Thorlabs AX252-A, Physical Angle $\alpha = 2.0^\circ$, $\tau = 176^\circ$ and index of refraction n at d-Line (587.6 nm) = 1.458. Therefore, the resulting distances Z_{max} are 244 mm, 250 mm, and 256 mm for 445 nm, 488 nm, and 561 nm, respectively.

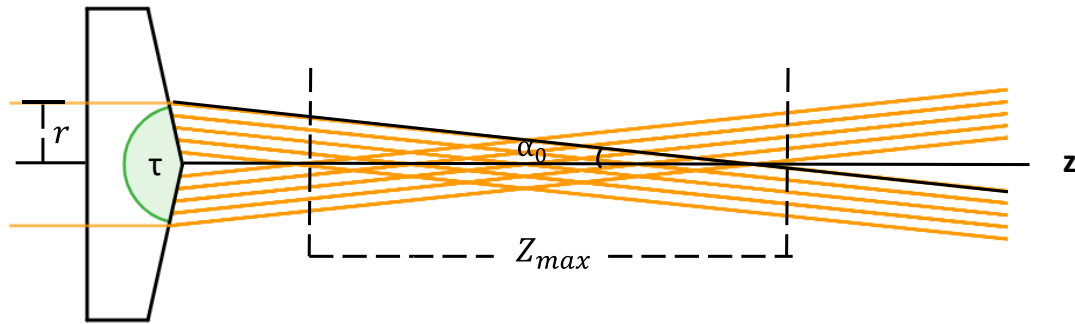


Figure 14 Schematics for an axicon lens.

However, axicons are not perfect lenses; the round axicon tip makes the intensity profile vary smoothly along the propagation axis. It also creates low-frequency components in the spatial-frequency spectrum at the Fourier plane when a lens is utilized for Fourier transforming the Bessel beam (Brzobohatý et al., 2008). Therefore, the characterization of the axicon lens is crucial to obtain the desired Bessel beams and to know the correct position to be placed in the LFSM setup.

In this work, the axicon characterization was performed numerically and experimentally. A Matlab code was developed to calculate the intensity profile numerically along the z -axis, applying equation (13) as shown by Becker et al., 2019. A general flow diagram for the Beam propagation simulation is described later in **Figure 19** in Section 3.3.2. Meanwhile, **Figure 15a** depicts the experimental layout to characterize the Bessel beam generated by the axicon. The beams' intensity distribution was measured using a CCD camera (Thorlabs, DCC1545M with pixel size $5.2 \mu\text{m}$) positioned in front of the axicon. The camera was mounted onto a motorized linear translation stage (Newport, MTN200BLHS), so the intensity profiles were taken by moving the camera along the z -axis. A neutral density filter (OD=4) was utilized, and an exposition time of 50 ms was used in the camera to adjust the beam intensity. The laser wavelength used was 488 nm with a beam diameter of 8.1 mm.

Using a similar layout, the intensity distributions at the Fourier plane were taken. For that, a 50 mm focal length lens was placed at this distance in front of the focused Bessel beam waist (see **Figure 15 b**). ImageJ software was utilized to process the images, where only the background signal and the hot and NaNs pixels were removed. The Fourier plane images were used to build a home-made spatial filter to remove the low-frequency components.

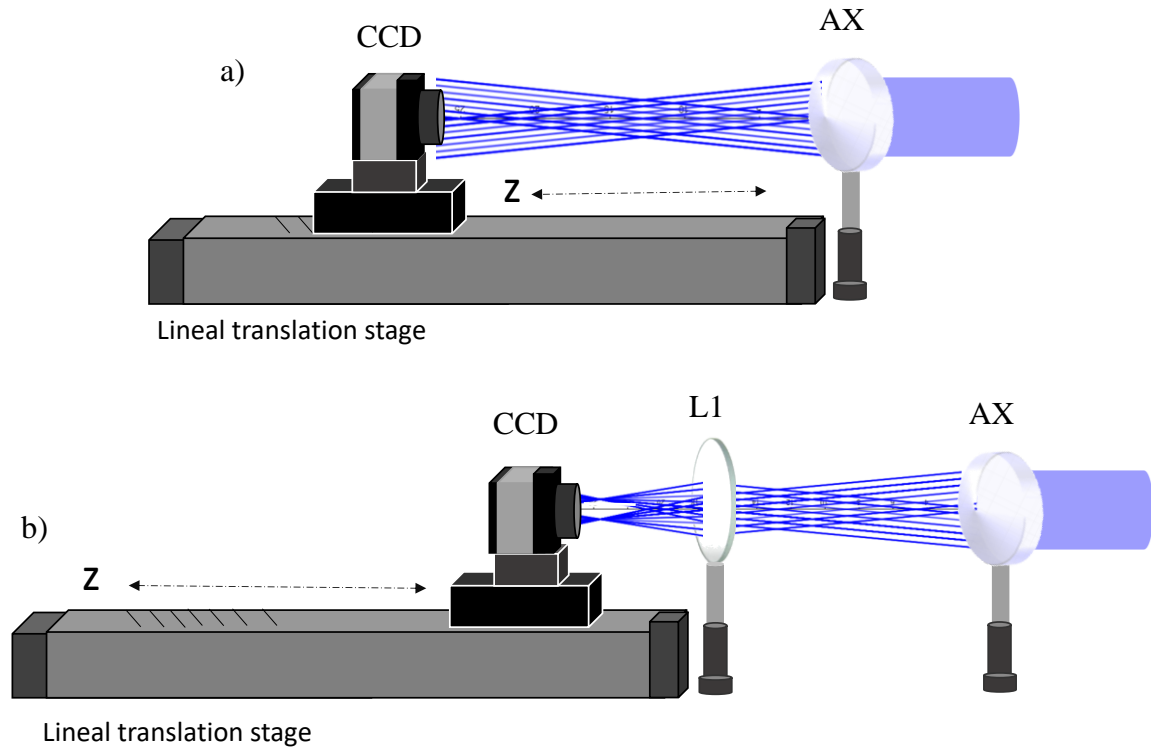


Figure 15 Experimental layout for the Bessel beam characterization after the axicon. a) Characterization of the Bessel beam generated by the axicon. b) Bessel beams at the Fourier plane characterization. Axicon (AX), Lens $f = 50$ mm (L1).

3.2 Multicolor LSFM optical setup

The experimental setup for a multicolor LSFM is shown in **Figure 16**. It consists of three different cw-lasers (Coherent, Obis; operating at 445, 488, and 561 nm) sequentially turned on/off and synchronized with a single camera's acquisition frame rate for rapid multicolor image acquisition (Licea-Rodriguez et al., 2019). The system can work either under the SPIM configuration, using Gaussian beams for the fluorescence excitation, or under the DSLM configuration, using Bessel or Gaussian beams for the excitation.

3.2.1 Excitation system

The excitation lasers at 445 nm, 488 nm, and 561 nm wavelengths were intensity-modulated using an Arduino board, as shown in J. Licea-Rodriguez *et al.*, (Licea-Rodriguez et al., 2019). Two dichroic filters recombined the lasers (Thorlabs, MD499, and MD480). The recombined beams were spatially filtered using an aspheric lens ($f = 8$ mm) and a 50 μm pinhole. Then, the filtered beams were collimated using an achromatic 50 mm focal length lens. Afterward, the beams were split into three paths A, B, or C (see **Figure 16**), using polarizing beam splitter cubes and achromatic half-wave plate retarders (not shown in the figure). Path A corresponds to the DSLM-Bessel configuration and path B to the DSLM-Gaussian one.

Path A uses a single axicon AX (Thorlabs AX252-A) to form the three-color Bessel beams at around 78 mm in front of it. Afterward, an achromatic Fourier lens L_1 ($f_1 = 50$ mm) transforms the Bessel beams, producing three different ring-shaped beams at the Fourier plane (shown in **Figure 23**). The transformed beams had non-zero intensity peaks at the rings' center (not shown) but were much lower against the corresponding rings' intensity. Notice that such peaks and undesired intensity modulations at the rings, formed by low spatial frequencies (due to the axicon round tip), affected the Bessel beams' axial and lateral intensity distributions (Brzobohatý et al., 2008). Therefore, a homemade spatial filter (represented by the black square) is placed at the Fourier plane to filter out the undesired low spatial frequencies and get cleaner ring-shaped beams. The spatial filter was fabricated using photolithography on black and white photographic film based on the results obtained in **Section 4.1.1**.

A second achromatic lens, L_2 ($f_2 = 100$ mm), projects the images of the filtered ring beams on the galvanometric mirrors (GM, Thorlabs GVS201, and GVS202) to scan the beams to create the light-sheet. A polarizing cube recombined the beams coming from paths A and B. either of these paths was blocked to switch between these two configurations. A telescope system composed of the achromatic scanning lens (SL, Thorlabs LSM03-VIS) and the tube lens (TL, Thorlabs TTL200) projects and pivots the scanned beams at the back focal plane of a Plan Achromat excitation objective EO (Olympus, 10x; NA: 0.25; WD: 13 mm); which finally forms the multiple Bessel (or Gaussian) light-sheets at the sample plane, i. e., along the XY-plane according to the XYZ coordinate system as shown in **Figure 16**.

Path C is used for SPIM, where a simple achromatic cylindrical lens (Thorlabs ACY254, 50-mm focal length) is used to form the light-sheets. A flip mirror was used to direct the beam to path B or C.

3.2.2 Collection system

The fluorescence signal generated in the illuminated sample plane is collected in a direction orthogonal to the sample plane, i.e., along the z-direction, by one of the following collection objectives CO: Mitutoyo, 50x; NA: 0.55; WD: 13 mm, Mitutoyo, 20x; NA: 0.40; WD: 20 mm WD and Olympus, 10x; NA: 0.25; WD: 13 mm. Then a tube lens (TL, Thorlabs TTL200) forms the image onto the CMOS camera (Thorlabs, DCC3240N). An interferometric multiband filter IMF (Semrock, Em01-R488/568-25) is used to block the excitation lasers of the fluorescence signal. The sample was carefully mounted over a computer-controlled XYZ linear translational stage (Thorlabs, NanoMax 300), allowing to take images from different planes and regions of interest.

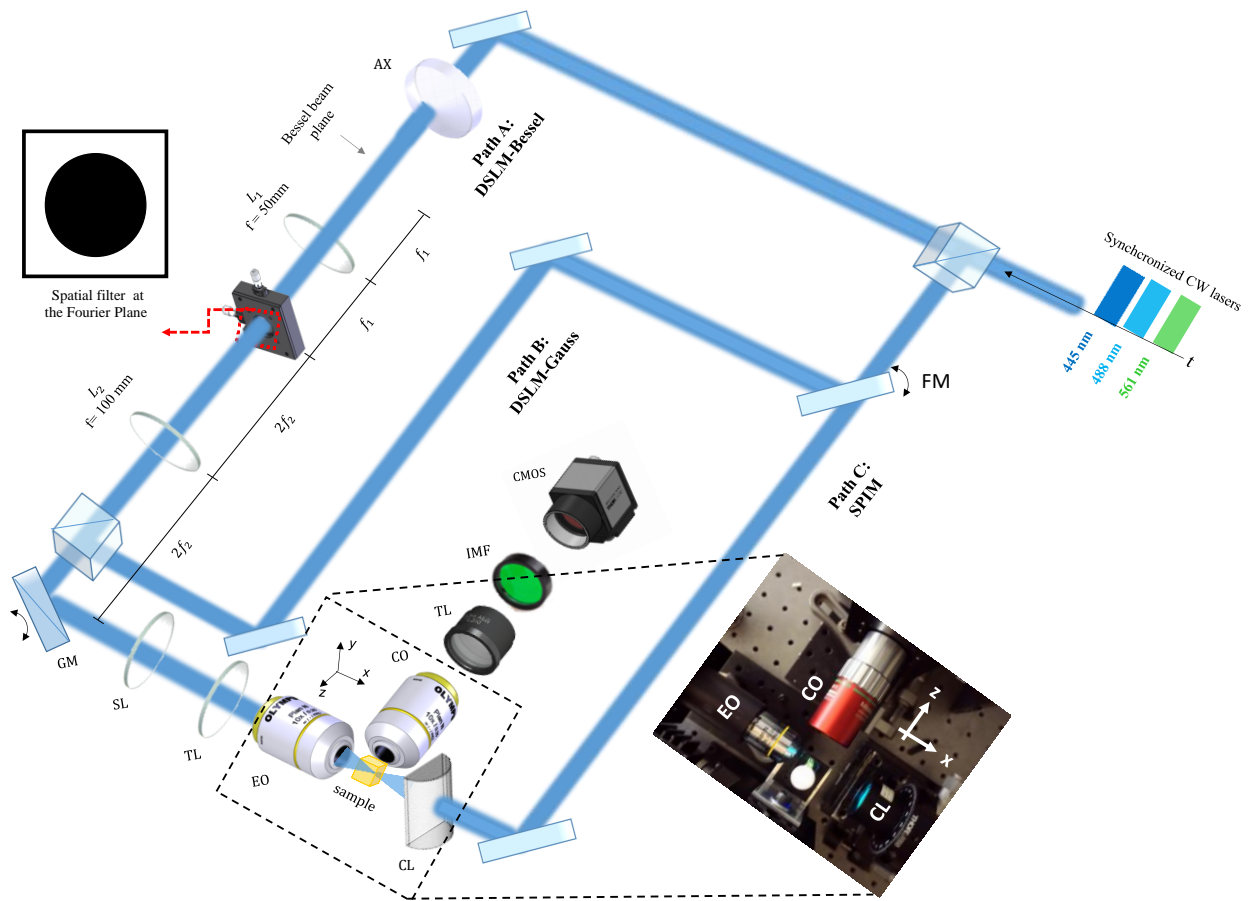


Figure 16 Multicolor LSFM layout for DSLM and SPIM configuration using Gaussian and Bessel beams. AX, axicon; FL and L1, achromatic lenses; GM, galvanometric mirror; SL, scanning lens; TL, tube lens; EO, excitation objective; CO, collection objective; IMF, interferometric multiband filter; CMOS, camera; CL: achromatic cylindrical lens; and xyz, laboratory coordinate system.

3.3 Computational methods

3.3.1 Image processing and data storage

The images were acquired using an implemented MatLab interface program that synchronizes the cw lasers excitation with the CMOS camera acquisition. The format to save the images was “TIFF.” The image acquisition parameters such as the integration time (int), frames per second (fps), and depth-scanning step size along z were adjusted accordingly for each sample. ImageJ (a free software created by Wayne Rasband from “National Institute of Health,” USA) was used to analyze the images and perform the 3D reconstruction.

Figure 17 shows the image processing analysis workflow utilized to process the taken image stacks. It consists of five main computation modules describing the image processing protocol (see **Figure 17**). First, the background noise was subtracted from the raw images or stacks (which consisted of 2D images recorded for each of the three-color channels). The background noise was an image taken without lasers excitation. Hot and NaNs pixels were also removed in the first step, replacing them by the median value of the surrounding pixel if the threshold value is >1 . If the stack is composed of two or three colors channels, the stack was split to get stacks at a single color. The second module removed the noise from the front and back images for each plane n of the image stack Im containing $n = 1, 2 \dots N$ planes. Here, $\Delta 1_n = Im_{n-1} - Im_n$ represent the noise from the front image, while $\Delta 2_n = Im_{n+1} - Im_n$ describe the noise from the back image. The resulting $Im2$ image is, therefore, $Im2 = Im - \Delta 1 - \Delta 2$. Notice that the first and the last images are lost in the process because there are no front and back images, respectively. Therefore, the end $Im2$ stack contains $N-2$ planes

For the third module, the stack was deconvolved using the Lucy–Richardson algorithm included in the plugin DeconvolutionLab2 in ImageJ. The number of interactions was adjusted to 10 for this process, and a fitted PSF from an experimental PSF was used. Notice that the light-sheet illuminating the sample is static, i. e., at a constant distance from the CO. The sample is moved backward and forward from this image plane to obtain the different z -planes. Therefore, the central PSF is utilized to deconvolve all the z -plane images. **Figure 18** depicts how the volumetric PSF is defined to deconvolve the image stack. The deconvoluted stacks undergo a second back- and forward- image noise subtracting process in the fourth module. Finally, the stacks are merged and projected in 3D for each color.

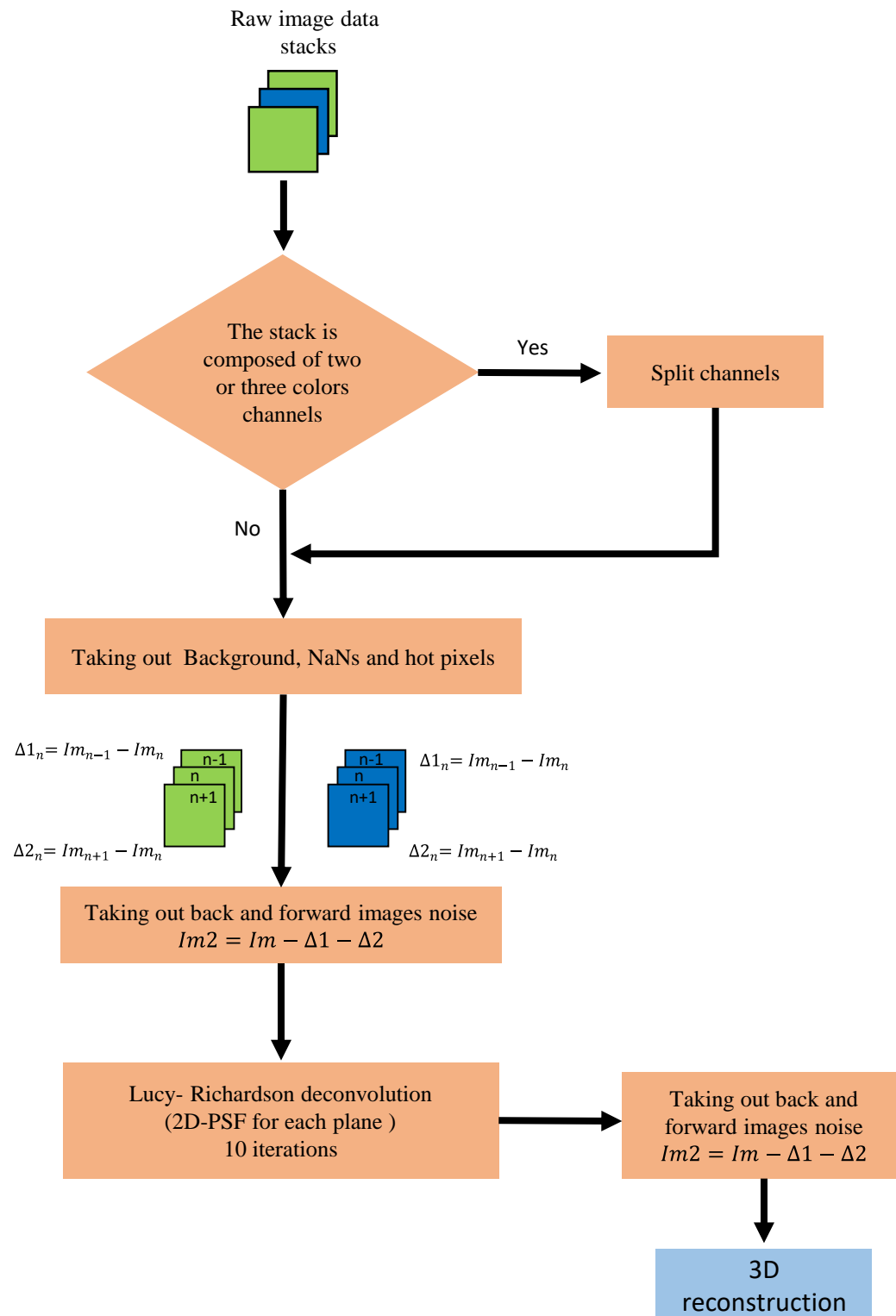


Figure 17 Image processing analysis workflow.

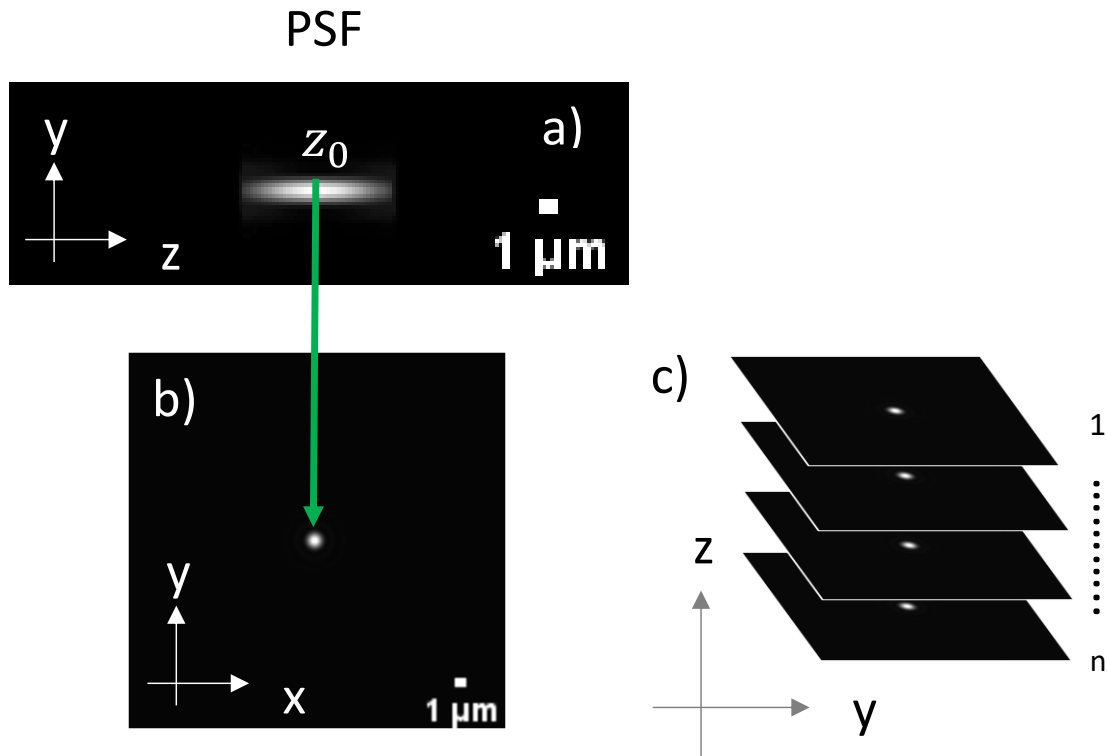


Figure 18 Fit PSF used in the LSFM deconvolution process. a) PSF along zy axis, b) PSF central plane along yx axis, c) PSF central plane duplicate the number of images from the stack.

3.3.2 Beam propagation simulation

A beam propagation computational calculation was executed using MATLAB to simulate the DSLM-Bessel and DSLM-Gaussian configurations. The MATLAB code was based on the Huygens-Fresnel diffraction integral method using cylindrical coordinates (see equations (13) in section 2.6). The algorithm calculates the intensity distribution along x , y , and z (r, θ, z) generated by a thin lens, ignoring diffraction effects on the edges. The field's radius behind the lens and the effective focal length determines the NA. The focal distance was obtained from the EO used in the experiments (Olympus, 10x; NA: 0.25, $f = 18 \text{ mm}$,). The radius of the input beams was experimentally measured at the plane behind the EO back focal plane using a Canon EOS Rebel T6 camera (without the objective lens) with a pixel size of $4.30 \mu\text{m}$.

Figure 19 shows the flow diagram for the program. First, the input parameters as the focal length (f), the beam wavelength (λ), the input beam radius (r_0), the maximum propagation in the axial direction (z), the sampling resolution in μm (N), and the XY matrix size (square matrix) are assigned. For DSLM-Gaussian

configuration, the input radio beam was considered at FWHM. Meanwhile, for DSLM-Bessel, a ring intensity was used with a radio 6 mm and a ring thickness 160 μm was considered. The ring intensity was constant and equal to 1 (but the intensity may have other distribution in the experiment). In either case, the field (E_0) is then multiplied by a thin lens phase mask and propagated (see equation (14)). Since $E(r, z)$ is rotationally symmetrical, a final 360° rotation generates a 3D field. The planes obtained at different z values were saved in ".tiff" or ".mat" files. For more information and application of this algorithm, see Enrique Romero Martinez's 2022 master thesis (thesis in progress).

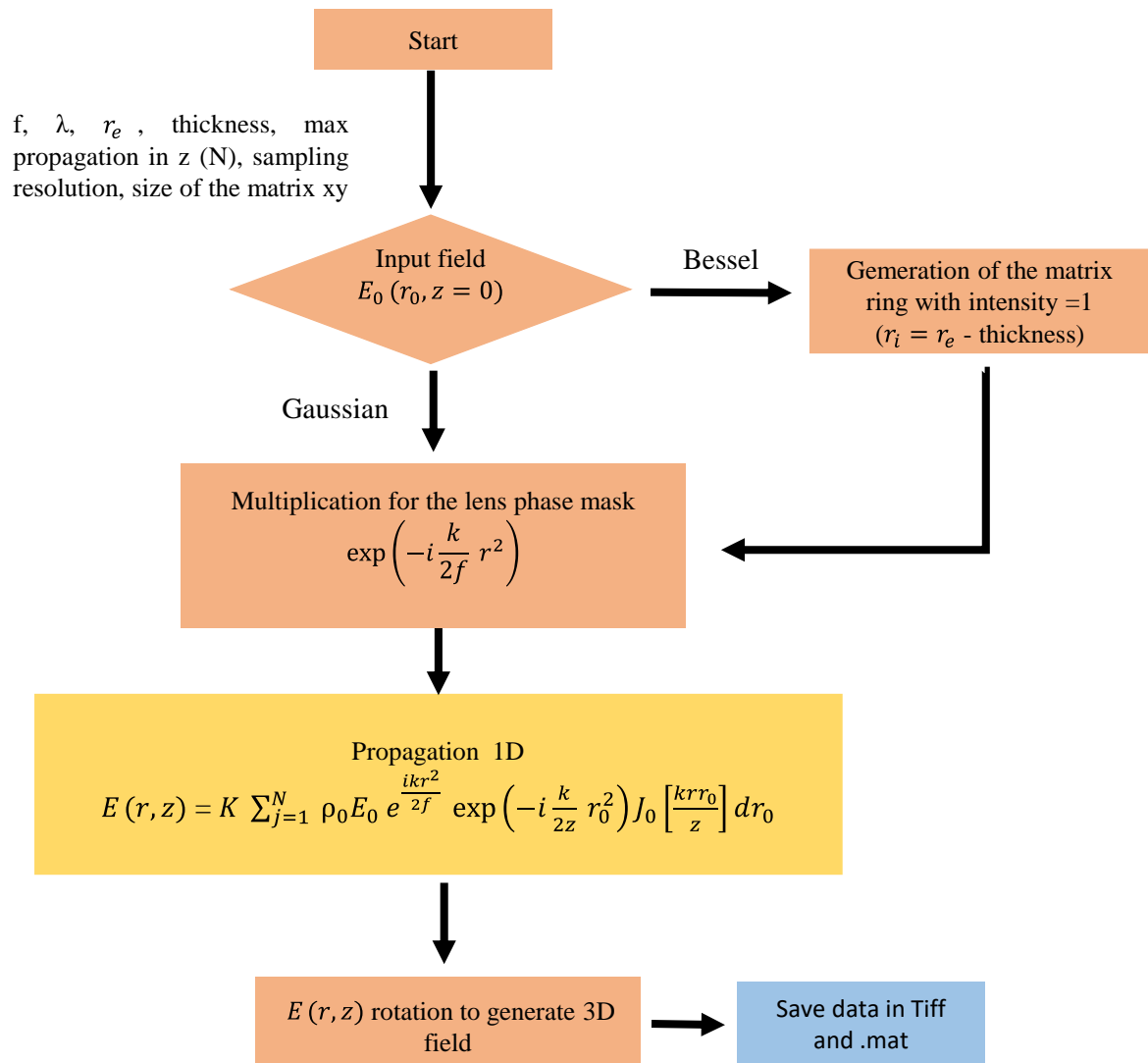


Figure 19 Beam propagation program flow diagram.

3.4 LSFM system characterization

3.4.1 Light-sheets characterization

For the light-sheet characterization, a mixture of fluorescein and rhodamine was used. A dilution of fluorescein and rhodamine was prepared using distilled water to a concentration of 0.5 mM. Then a quartz cell (Hellma Analytics, 100-QS) was filled with a 1:30 rhodamine-fluorescein mixture. The fluorescence of fluorescein was used to characterize the light-sheet excited with the 445 and 488 nm laser sources. In contrast rhodamine was used to characterize the light sheet excited with the laser at 561 nm.

3.4.2 Optical resolution characterization

For the different LSFM configurations' optical resolution characterization, fluorescent beads of 0.16 μm (Dye XC, concentration 1%, Estapor Microspheres) were employed. Their fluorescence excitation wavelength range is from 440 to 520 nm (with excitation maxima at 470, 480, and 490 nm) with an emission range from 500 to 600 nm (with two maxima at 525 and 560 nm). Similarly, fluorescent beads of 1 μm (Fluoresbrite® Polychromatic Red microspheres, 2.5% w/v) were utilized for the light-sheets colocalization. These last beads are internally dyed with different fluorophores (R-PE, Rhodamine, Nile Red, CyTM3, Alexa Fluor® 532 Alexa Fluor® 546, and SYTOX Orange), resulting in a broad excitation band with a wavelength range from 440 to 570 nm and an emission wavelength range from 540 to 615 nm (with maxima at 569 nm). Solid samples containing fluorescent beads were prepared separately for 0.16 μm and 1 μm beads. A 1:10 bead-water solution was mixed with melted 1.5% agarose at 1:100. Afterward, 300 μl of the still melted bead-agar mixture was added into a quartz cuvette, and it was let to cool down at room temperature for 5 min until solidification. Finally, the quartz cuvette was mounted onto a custom-designed holder attached to the computer-controlled XYZ translational stage with the sample facing toward the CO.

3.5 Biological samples: *Sordaria macrospora*

To compare the multicolor LSFM system's performance using Bessel beams against Gaussian beams for the fluorescence excitation, we performed multicolor imaging on perithecia of *Sordaria macrospora* strain

TIT29D- kindly provided by Dr. Ines Teichert from the University of Böchum, Germany. This mutant strain does not produce melanin and expresses TdTomato-tagged histone 2B as a nuclear marker.

The strain was inoculated in Petri dishes containing Vogel's minimal medium solidified with 1.5% agar and grown for 13 days at 30°C. For imaging, a 1 cm² block of solidified agar containing perithecia was cut out and carefully mounted into a quartz cuvette for imaging (see **Figure 20**). To visualize the cell wall, a 0.1% w/v solophenyl flavine 7GFE 500 (SF7) stock solution was prepared, diluted 10-fold in deionized and sterilized water (100 µg/ml), and applied directly to agar with perithecia using a pipette. The time elapsed between applying SF7 to the sample and imaging was ~ 1 min. To visualize the nuclei, an excitation wavelength of 561 nm was used, and emission range from 580 nm to 675 nm was collected. To visualize the cell wall, the excitation wavelength was 445 nm and an emission wavelength range from 400 to 630 nm (with a maximum at 491 nm) was collected.

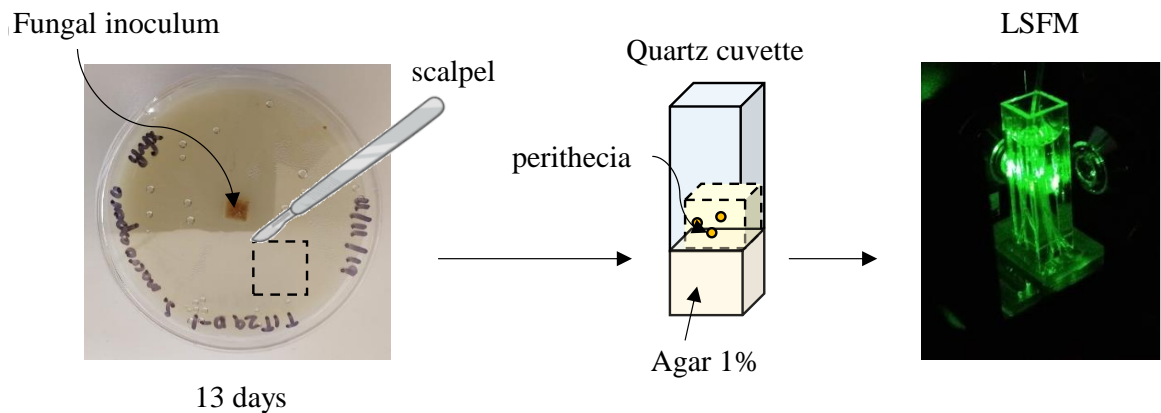


Figure 20 Sample preparation for LSFM. After 13 days of growth, a block of 1 cm² was cut using a sterile scalpel. The block was mounted into a quartz cuvette. Then the quartz cuvette was mounted onto a custom-designed holder attached to the computer-controlled XYZ translational stage with the sample facing toward the CO.

Chapter 4. Results and Discussion

This chapter presents the results and discussions obtained in this research project. First, the different wavelength Bessel beam formation using an axicon lens is characterized experimentally and supported with numerical simulations. Next, the characterization for each LSFM configuration (DSLIM- Bessel, DSLIM- Gaussian, and SPIM-Gaussian) is described. Here, the multicolor FoV, optical sectioning, optical sectioning vs. FoV ratio, and the lateral and axial resolution are discussed, considering the effects produced in the end LSFM images due to the chromatic light-sheet shifts and beam types. To show the differences between DSLIM-Bessel and -Gaussian imaging, biological samples of *Sordaria macrospora* are utilized. Finally, the results of simulating Bessel and Gaussian beams for light-sheet microscopy excitation using the same excitation objective are presented and discussed for the cases when the same FOV or NA is utilized.

4.1 Bessel beams formation using an axicon lens

4.1.1 Bessel beams characterization after the axicon

The effects of passing a collimated Gaussian beam through an axicon to form Bessel beams are visualized in **Figure 21**. Experimental and simulated transversal XY-beam profiles at different distances along the z-axis are shown. The images were taken and simulated at 1 cm steps starting from the nearest position to the axicon lens for the experimental images. **Figure 21** shows only representative images for discussion purposes. Notice that a typical Bessel transverse profile was observed at $z \geq 3$ cm propagation distances for the experiment. Meanwhile, the Bessel rings are formed practically after passing the ideal axicon for the simulated images.

Figure 22 shows the simulated and experimental XZ-image plane of the Bessel beam propagation. **Figure 22a** shows a ray tracing of the axicon utilized in the experiments simulated using Zemax software. In contrast, **Figure 22b** shows the 2D images of the Bessel beam intensity projected at the XZ-plane simulated with MATLAB using Huygens-Fresnel diffraction integral. For the simulations, the axicon parameters are $\alpha = 2^\circ$, $\tau = 176^\circ$, and $n_{587.60nm} = 1.458$, respectively. Meanwhile, **Figure 22c** shows the 2D images of the Bessel intensity reconstructed from experimental images similar to those shown in **Figure 21** but at shorter steps (0.2 cm).

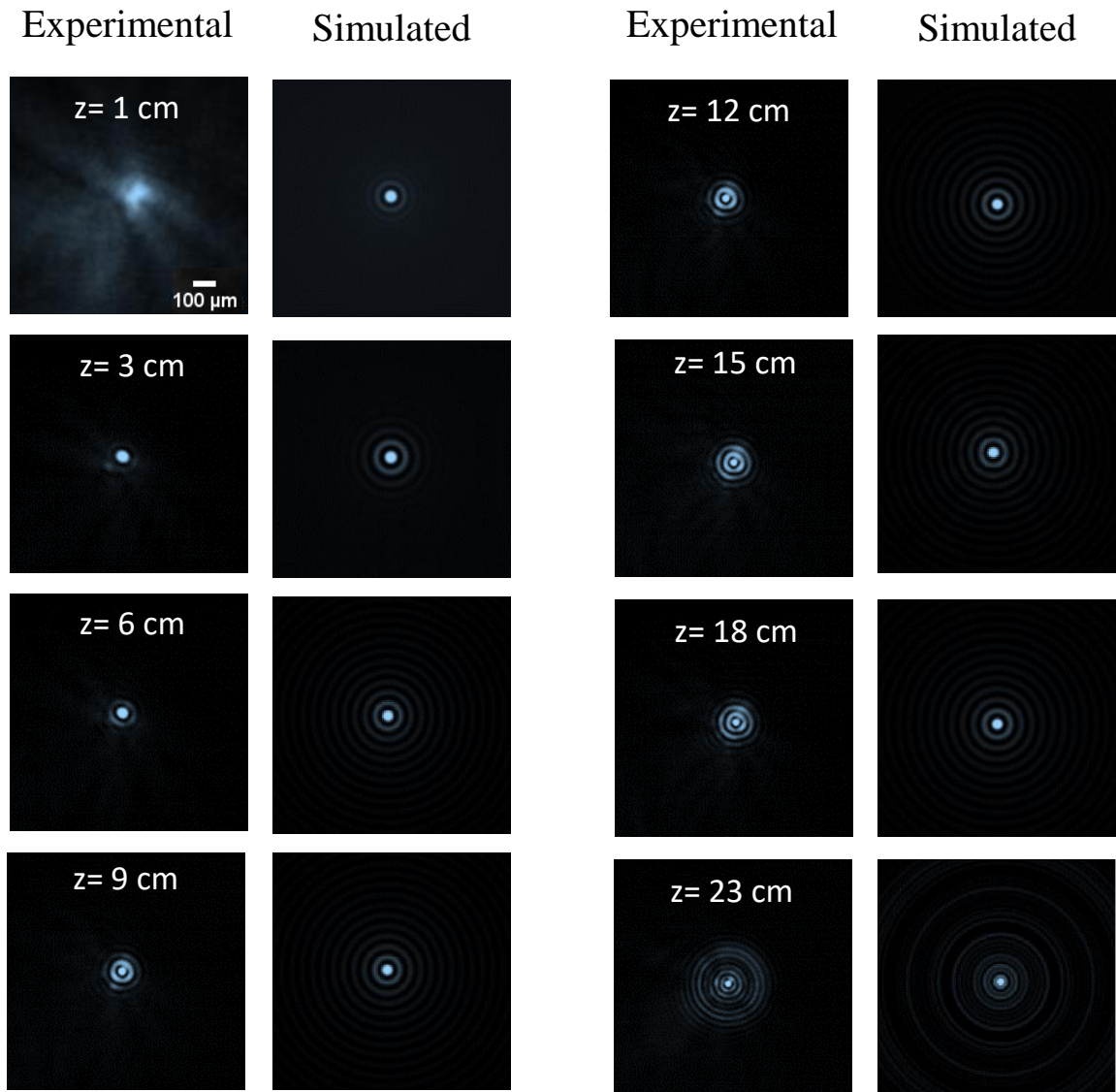


Figure 21 Experimental and simulated xy transverse images generated by an axicon lens at different distances along the z axis.

According to equation (15), the propagation length for considering a uniform intensity distribution of the Bessel beams is $z_{max} = 25$ cm, while for the experiment results to be $z_{max} = 240$ cm.

However, because axicons do not possess a perfectly sharp tip and the input beam passing through it is a naturally diffracting (Gaussian) beam, the intensity of the experimental results (**Figure 22c**) varies periodically along the propagation axis, attributed to diffraction effects. The round end produces a lens effect close to the axicon's optical axis, focusing the incident beam's central part at short propagating distances and generating a divergent wavefront (see **Figure 21** at $z = 1$ cm). This diverging wave interferes

with the converging waves coming from the outer part of the axicon, producing the modulated beam intensity along the z-propagation with a period $(1 - \cos\alpha_0)$ (Verveer et al., 2007) decreasing for distances $z \geq 18$ cm.

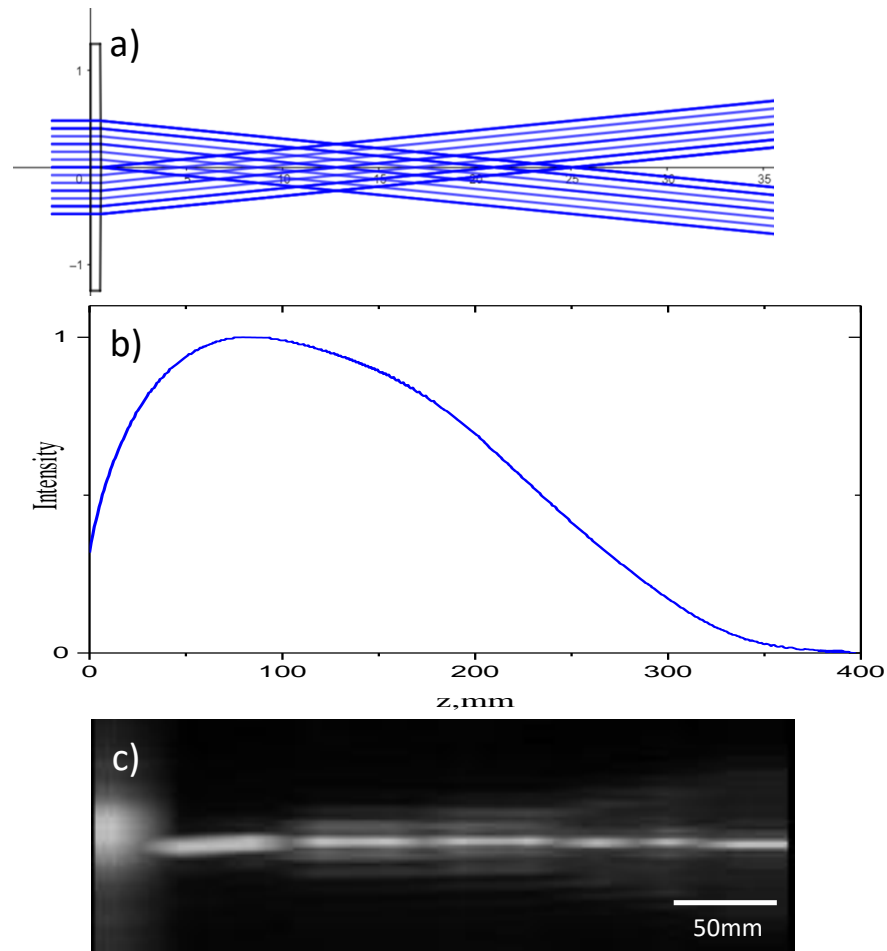


Figure 22 Beam propagation of an axicon lens along z axis. a) Propagation of rays coming from axicon lens using the geometric optics approximation a) Intensity profile obtained using the model implemented by Brzobohat' 2008 in MATLAB, c) Intensity profile obtained from a 3D reconstruction of an experimental data. All the calculations were performed considering an excitation wavelength of 488 nm and a beam radius (ω_0) of 4.1 cm.

The optical Fourier transform (FT) was performed using a lens (F1) (see **Figure 23 a**) with a focal length $f = 50$ mm. The resulting spatial frequencies were optically filtered using a custom-made spatial filter. This transformation allows visualize the Bessel beam's low-frequency component to fabricate the corresponding spatial filter. Images of the angular spectra for the three different wavelength Bessel beams were taken using a CCD located right at the FT plane (*i.e.*, at L1 focal distance). **Figure 23** shows the Zemax simulation and the angular spectra resulting from an optical Fourier transformation. The typical ring-shaped patterns that result from the Fourier transformed Bessel beams are observed in both the Zemax

simulation (**Figure 23 b-d**) and experimental results (**Figure 23 e-g**). From the experiment, the ring diameters are $1574\ \mu\text{m}$, $1575\ \mu\text{m}$, and $1577\ \mu\text{m}$ for $445\ \text{nm}$, $488\ \text{nm}$, and $561\ \text{nm}$, respectively, where the reported diameter is the internal ring. These measurements were used to fabricate an appropriated single opaque circular obstacle (spatial filter) at the Fourier plane.

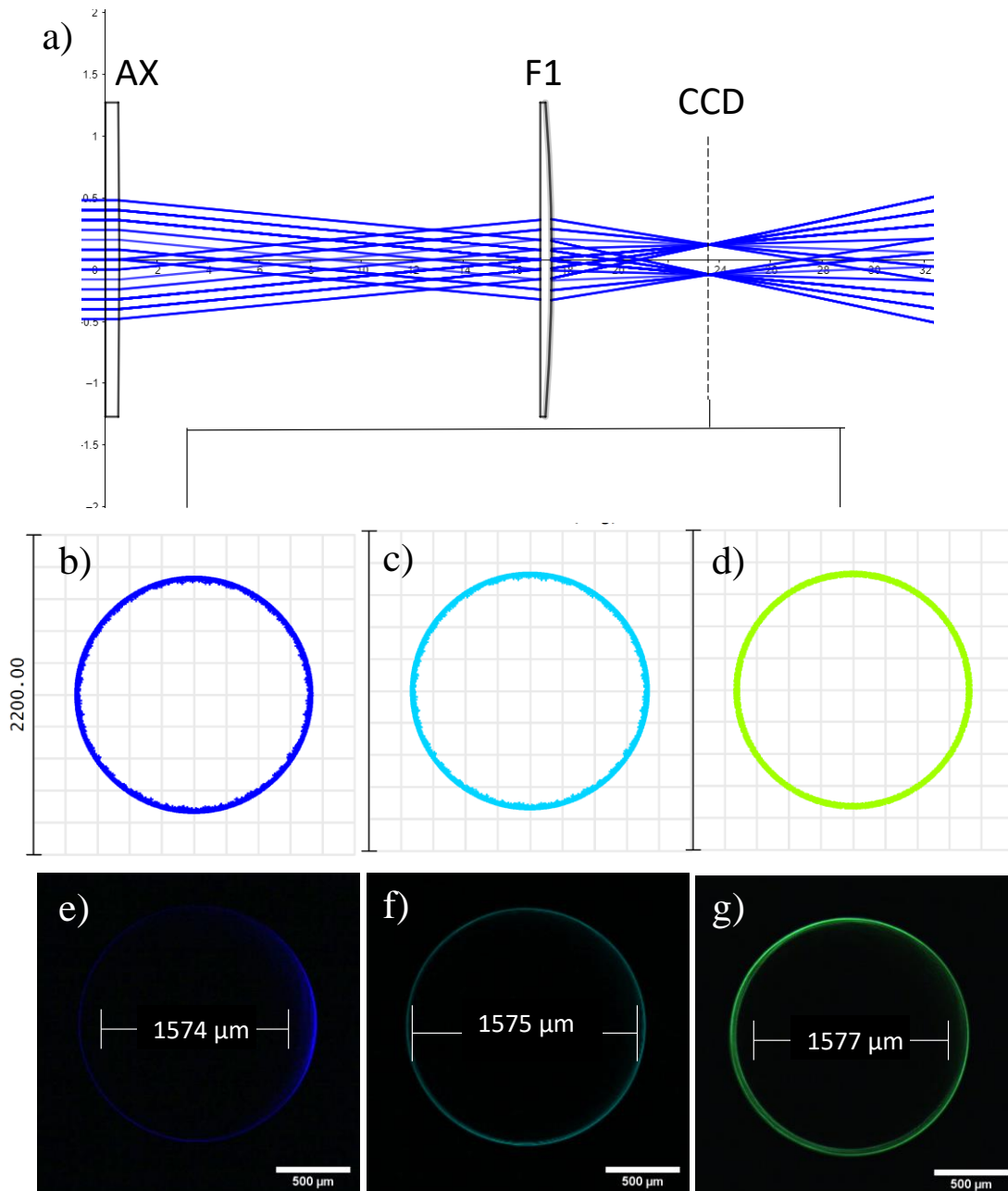


Figure 23 Fourier transform of an axicon lens. a) diagram of an axicon and a lens used to generate the Fourier transform at the focus plane, where a CCD camera was used to obtain the images (model using geometric optics). (b, c, and d) Simulated Fourier transform for a wavelength of $445\ \text{nm}$, $488\ \text{nm}$, and $561\ \text{nm}$, respectively. (e-g) Experimental Fourier transform images for a wavelength of $445\ \text{nm}$, $488\ \text{nm}$, and $561\ \text{nm}$, respectively.

4.1.2 Bessel beams characterization at the excitation objective back focal plane

The ring-shaped Fourier transformed Bessel beam patterns, imaged at the plane between the two galvanometer mirrors (shown in **Figure 24e-g**), were further amplified (5X) and imaged at the back focal plane of the EO utilizing the lenses SL and TL of the optical layout (shown in **Figure 16**). In that way, the multicolor Bessel beams can finally be reproduced at the sample plane after passing through the EO. **Figure 24** shows the magnified rings with ending diameters sizes of 8.271 mm, 8.776 mm, and 8.977 mm for the 445nm, 488 nm, and 561 nm wavelengths, respectively (see **Figure 24 a-c**). Notice that unfiltered rings are also shown in the figure; therefore, it was possible to observe the lower-frequency components provoked by the axicon round-tip as observed in the zoomed image in **Figure 24 d** (see also the intensity profile traced in **Figure 24 e**). Peaks with lower intensity values (< 80) are undesired since they affect the Bessel beams' axial and lateral intensity distributions (Brzobohatý et al., 2008). Therefore, the spatial filter (the opaque circle) placed at the back focal plane of lens L_2 blocked those low-frequency components resulting in more uniform Bessel beams.

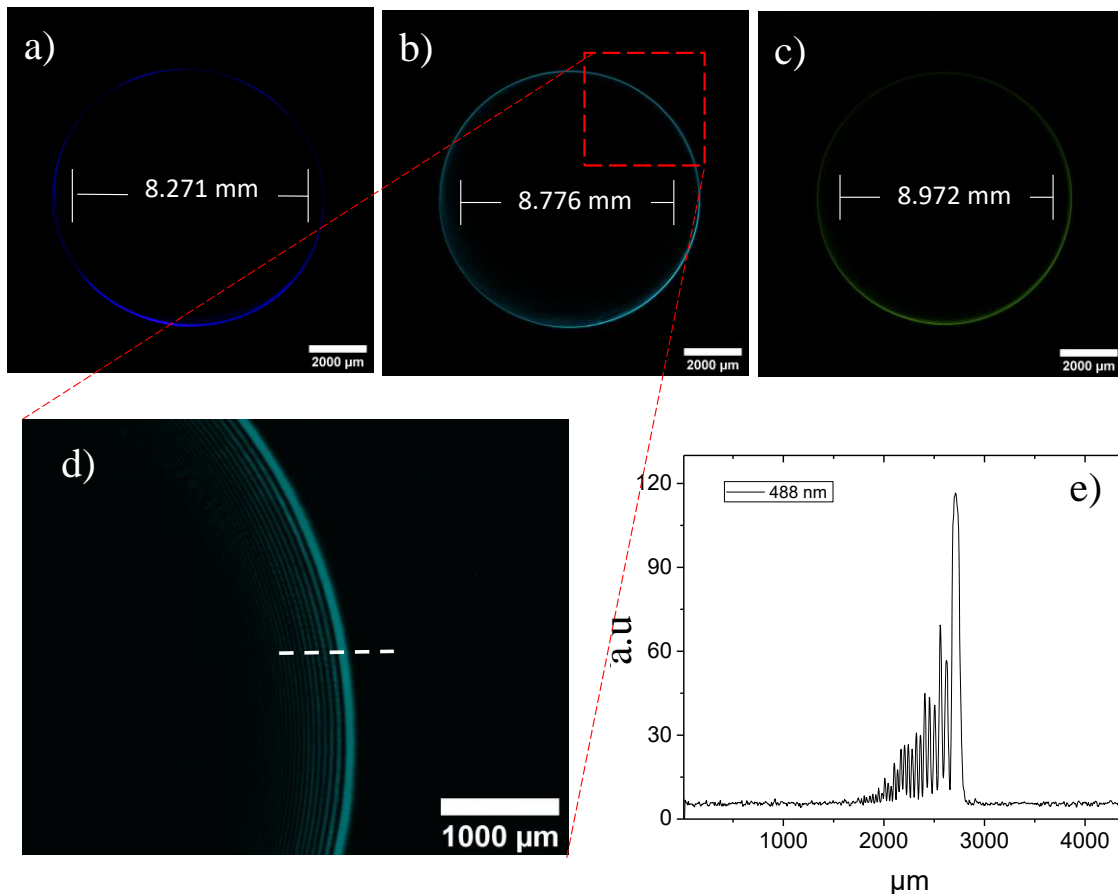


Figure 24 Input Bessel beam profile at the excitation objective back focal aperture in the LSM. a-c) Fourier transform at the back focal aperture of the excitation objective for 445nm, 488 nm and 561 nm, respectively. d) Zoom of the ring from picture b. e) Intensity profile corresponding to the dashed line in picture d).

4.2 Optical setup characterization

4.2.1 Multicolor light-sheets

The static (non-scanned) focused beams dimensions were measured using their fluorescence excitation when passing through the quartz cuvette containing the rhodamine-fluorescein solution to characterize the light-sheets. The three fluorescent beams generated into the sample were individually imaged using the Plan Achromat 10× (0.25 NA) CO and the CMOS camera, covering approximately 560 x 450 μm^2 . **Figure 25** shows the focused beams at 445, 488, and 561 nm for DSLM-Bessel (a) and DSLM-Gaussian (b) configurations. Notice DSLM-Bessel and DSLM-Gaussian configurations are produced under the same EO to compare Bessel vs. Gaussian light-sheet excitation under similar NA conditions.

Figure 25c shows the SPIM-focused beams; for that, the cylindrical lens was rotated 90°. The beams propagation direction for the three configurations is indicated with the white arrows. Meanwhile, **Figure 25 d-f** and **23 g-i** show the intensity profile traces along the x-direction and y-direction, respectively. Δx and Δy are the width of the beams along x and y measured at the FWHM (full width at half maximum) value of their intensities. These values are the *light-sheet FOVs* and the *light-sheet thickness*, associated, but not equal, to the excitation objective DoF and the light-sheet optical sectioning capability, respectively (Remacha et al., 2020). The gray area in **Figure 25 d-f** shows the effective field of view (FOV_{eff}) for the three configurations. The FOV_{eff} is defined as the FWHM where the three beams are overlapped. **Table 2** summarizes the values for all the FOVs (Δx), thickness (Δy), and $\Delta y/\Delta x$ ratios for the three LSFM configurations and excitation wavelengths of **Figure 25**. Based on these results, DSLM-Bessel is a better option for multicolor LSFM in terms of FOV_{eff} and the axial resolution over this whole FOV, as explained next.

Table 2. Lateral and axial FWHM widths for the different LSFM configurations and wavelengths *

LSFM Configurations	Δx (μm)			Δy (μm)			$\Delta y/\Delta x$			FOV_{eff} (μm)
	λ_1	λ_2	λ_3	λ_1	λ_2	λ_3	λ_1	λ_2	λ_3	
<i>DSLM Bessel</i>	341	351	314	8.8	9.2	8.4	0.025	0.022	0.026	283
<i>DSLM-Gaussian</i>	35	37	40	2.1	2.3	2.5	0.061	0.062	0.062	10
<i>SPIM</i>	246	247	278	12.8	14.3	16.2	0.052	0.058	0.058	224

* $\lambda_1=445$ nm, $\lambda_2=448$ nm, $\lambda_3=561$ nm

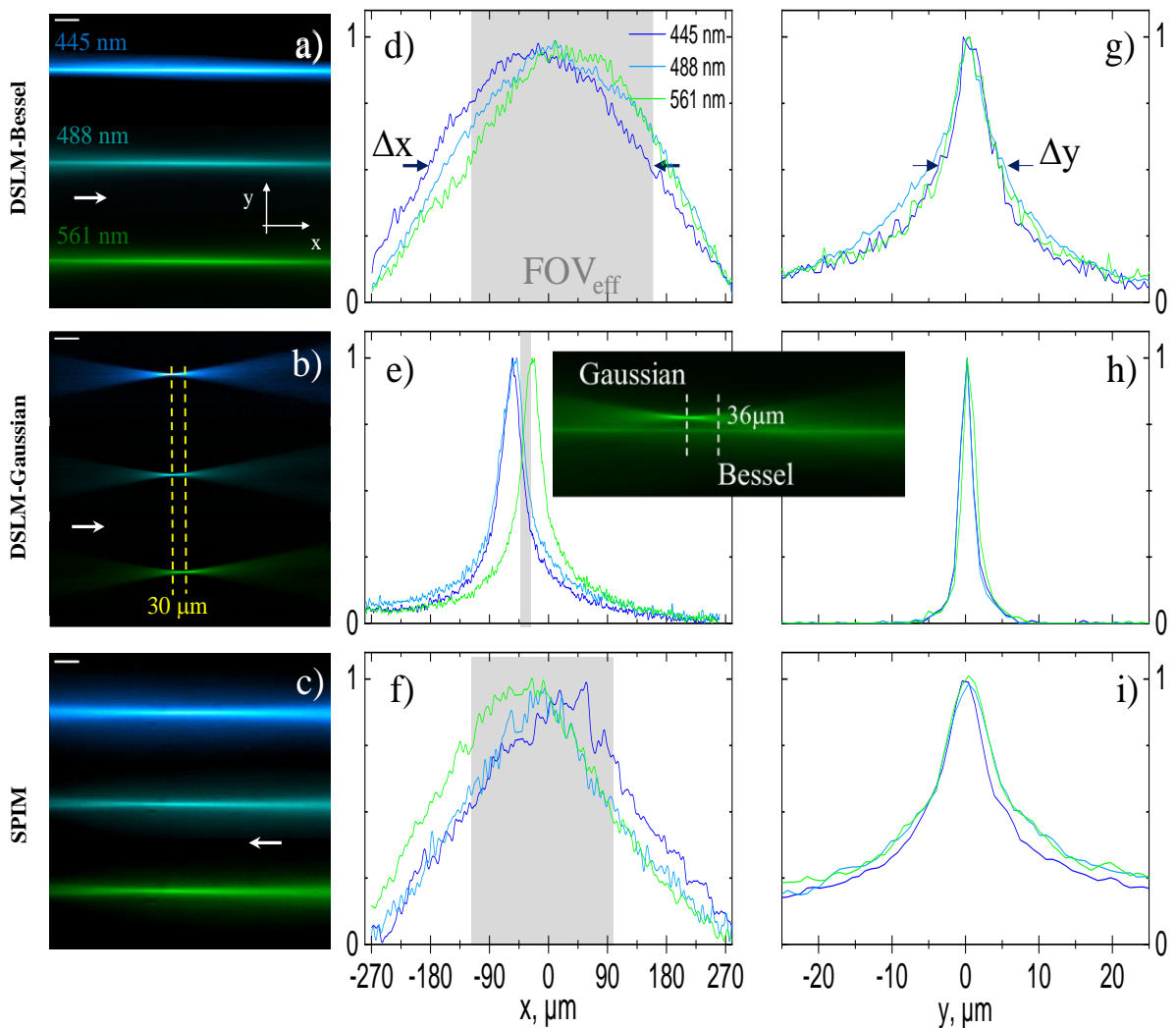


Figure 25 Characterization of the multicolor light sheets for the different configurations. Fluorescence images of the static (non-scanned) focused beams at 445, 488, and 561 nm for DSLM-Bessel (a), DSLM-Gaussian (b), and SPIM (c). The white arrows in (a-c) indicate the beam propagation. Normalized intensity profile traces along x-direction for DSLM-Bessel (d), DSLM-Gaussian (e), and SPIM (f); and y-direction for DSLM-Bessel (g), DSLM-Gaussian (h), and SPIM (i). The FWHM widths values are shown in Table 2. The shadowed gray area in Figures. (d-f) indicates the effective FOV. The yellow dash lines in Figure b indicate the achromatic shifting between 445 and 561 nm of DSLM-Gaussian. The inset image in Figure (e) shows the focal shift between DSLM-Bessel and -Gaussian beams for 561nm.

4.2.2 Multicolor light-sheets FOVs

The FOV in LSFM is associated with DoF's excitation objective. From the Gaussian beams propagation theory, the DoF is defined in terms of the Rayleigh length ($z_R = \pi\omega_0^2/\lambda$) (Power & Huisken, 2017) as $DoF = 2 \times z_R$, i.e., is the length where the minimum beam thickness ($2\omega_0$, at the beam focus) increases back and forth by a factor of $\sqrt{2}$. In practice, however, the FOV for LSFM is taken as the FWHM width of

the focusing beam intensity profile along its propagation direction (x-direction) (OlarTE et al., 2012, 2018; Remacha et al., 2020; Xiong et al., 2020); i.e., when seen from the collection objective. The focus intensity is modulated by a sinc^2 function in the beam propagation direction; therefore, the analytical expression FWHM is obtained from equation (11) in section 2.4.3. Because this relationship is meant for Gaussian beams, we estimate the different FOVs from the experimental intensity profiles shown in **Figure 25**, which are also useful for discussing the chromatic issues for multicolor LSFM.

From the Δx -values of **Table 2** (see the second column), measured for the different light-sheets configurations, it is deduced that the FOV of DSLM-Bessel is on average nine times larger than for DSLM-Gaussian and 1.3 times larger than for SPIM, regardless of the excitation wavelength. For instance, the FOV of the central wavelength ($\lambda_2 = 488 \text{ nm}$) is $351 \mu\text{m}$ for DSLM-Bessel, $37 \mu\text{m}$ for DSLM-Gaussian, and $247 \mu\text{m}$ for SPIM.

The chromatic implications on the multicolor LSFM FOVs are observed in **Figure 25 a-f**. When utilizing the same microscope objective for Gaussian and Bessel light sheets formation, two different kinds of shifts between their corresponding focusing beams occurs. Firstly, a shift of approximately $36 \mu\text{m}$ can be observed from the beam waist of the 561 nm Gaussian beam to the focal point of the Bessel beams (see inset image between **Figure 25 e** and **h**). The non-diffractive nature of Bessel beams provokes such focusing retardation. Consequently, the FOVs of DSLM-Bessel and DSLM-Gaussian configurations are not colocalized.

Secondly, additional shifts between the different wavelengths beams (on each configuration) also occur. Such chromatic displacements are unavoidably inherited by the objective's chromatic aberration, as observed in **Figure 25 d-f**. So the different light-sheet FOVs are not colocalized even within the same configuration, mainly for the DSL-Gaussian configuration as observed in **Figure 25e**. Therefore, a reduced effective field of view FOV_{eff} needs to be considered when performing multicolor imaging, like those depicted by the shadowed gray area in **Figure 25 d-f**. In DSLM-Gaussian, such FOV_{eff} is drastically reduced (approx. 75%), mainly because of the 445 nm and the 561 nm light-sheets FOV distance (see **Figure 25e**). For SPIM and DSLM-Bessel configurations, the FOV_{eff} were $224 \mu\text{m}$ and $283 \mu\text{m}$, respectively; that are large enough. However, DSLM-Bessel had better optical sectioning than SPIM. Therefore, the large DoF of DSLM-Bessel alleviates the beam's focus mismatches problems due to the objective chromatic aberrations without sacrificing optical sectioning.

4.2.3 Multicolor light sheets optical sectioning

The optical sectioning thickness could be defined as the axial distance containing 63% of the total fluorescence generated by the light sheet (Remacha et al., 2020) or FWHM of the beam waist. As mentioned before, the FWHM of the beam waist was used like other works (Olarde et al., 2012, 2018). The third column in **Table 2** shows the Δy -values corresponding to the different color light-sheet thicknesses measured on each LSFM configuration. In principle, a better optical sectioning capability is expected for DSLM-Gaussian with averaged Δy 's values around 2.3 μm , followed by DSLM-Bessel with average thicknesses values of 8 μm . The optical sectioning capability of DSLM-Gaussian is three times better than the one obtained with DSLM-Bessel, while this last is around twice better than SPIM, as observed in **Figure 25 g-i**. However, Bessel light-sheet thickness measurement can also be affected when a CO with large DoF is utilized since fluorescence excited from Bessel side lobes adds to the image taken to trace the Δy beams profile (as discussed in Section 4.4).

4.2.4 Optical sectioning vs. FOV ratio

The ratio $\Delta y/\Delta x$ gives the optical sectioning vs. FOV ratio. This value is the percentage at which an object can be fractionated axially in terms of the FOV length for a determined light-sheet configuration. Here the best scenario is that such a ratio be small (i.e., the smaller, the better), and its value keeps about the same for each color. From **Table 2**, DSLM-Bessel gives a better $\Delta y/\Delta x$ ratio, around 0.024 on average, followed by 0.055 for SPIM and 0.062 for DSLM-Gaussian. In other words, an object imaged under DSLM-Bessel configuration, with a size as big as its FOV, could be optically sectioned down to 2.4% of such FOV size. Meanwhile, the object could be fractionated up to 5.5% and 6.2% of their corresponding FOV sizes for SPIM and DSLM-Gaussian configurations.

4.2.5 The chromatic axial focal shifts limitation of Gaussian beams for multicolor LSFM

As mentioned above, the excitation objective chromatic aberration and the short DoF of DSLM-Gaussian configuration produce additional axial shifts between the focal positions of the different color beams. As discussed in **Section 4.3**, two focal shifts could be observed in the experiment (see **Figure 25b** and inset

picture in **Figure 25e**). A shift of 6 μm between the 445 nm and the 488 nm beams, and other shifts of 24 μm between the 488 nm and the 561 nm beams; a total difference of 30 μm between 445 and 561 nm (indicated by the vertical lines in **Figure 25b**). Such axial delays are either due to intrinsic chromatic offsets (present in any microscope objective type) or to the non-optimized alignment of the Gaussian beams. In either case, having chromatic offsets between different color light sheets is not practical for multicolor imaging since colocalized or uniformly illuminated FOVs are required.

In principle, one can either play with the beam's collimation before entering the objective or use an Achromatic (APO) objective lens to correct these focal shifts. However, the former case implies utilizing different optics to adjust each beams' divergence independently and minimize their axial mismatch at focus (International Organization for Standardization., 2013), ending with an undesired complex and expensive optical system. In the latter case, despite being the most highly corrected objectives for chromatic aberrations, slight separation between foci of different wavelengths exists and is compared to the LSFM FOV length, as shown in **Table 3**.

Table 3 shows the axial focal shift tolerances for different objective types according to the International Organization for Standards *ISO 19012-2* (International Organization for Standardization., 2013), which defines the minimum requirements regarding the chromatic correction. This table summarizes the computed DoF, the light-sheet FOV, and the chromatic axial focal shift tolerances for the different excitation objectives used in the LSFM systems cited in this work. The absolute value of the focus differences between the blue (F' -line) wavelength at 479.99 nm, and the red (C' -line) wavelength at 643.85 nm, define the axial shift tolerances (i.e., the focus difference, $|\delta_{C'} - \delta_{F'}|$, between the extreme wavelengths). The green (e -line) wavelength at 546.07 nm is the reference (central) wavelength.

As can be observed in **Table 3**, the focal shift tolerances depend on the microscope objective class. Even though the difference $|\delta_{C'} - \delta_{F'}|$ may fulfill the minimum distance accepted by the *ISO 19012-2*, note that it is in the order of the FOV length. For instance, see that the estimated tolerance for an ACH objective of 0.25 NA (as the one used in this work) is around 12 μm , and its average FOV is 16 μm . Since ACH objectives are not corrected for green wavelengths (Abramowitz et al., 2002), their usage in LSFM should be limited to blue and red Gaussian beams excitations for axial focal shifts within the FOV. Semiapochromat (FLU) objectives have a chromatic correction either for two or three lines (Abramowitz et al., 2002), despite that, both the estimated tolerance and FOV are around 11 μm for a 0.3 NA. It is worth noting that, although utilized for single wavelength excitation, many of the LSFM systems found in the literature use

semiapochromat (FLU) objectives (Cella Zanacchi et al., 2011; Olarte et al., 2012; Lavagnino et al., 2013; Gualda et al., 2014; Bassi et al., 2015; Stefaniuk et al., 2016; Müllenbroich, Turrini, et al., 2018).

Table 3. Axial focal shifts of different objectives class in LSMF.

Excitation Objective Class	Magnification/N A	DoF* (δ_{ob})	Light-sheet FOV**	Standard 19012-2 Axial Focal Shift tolerance	References
Achromatic (ACH)	10×/0.25	5.85 μm [†]	16.9 μm [‡] 18.6 μm [†] 21.4 μm [§]	$ \delta_{C'} - \delta_{F'} \leq 2 \times \delta_{ob}$ = 11.71 μm	[1]
ACH	10×/0.3	4.07 μm [†]	11.8 μm [‡] 12.9 μm [†] 14.9 μm [§]	$ \delta_{C'} - \delta_{F'} \leq 2 \times \delta_{ob} = 8.14 \mu m$	[2]
ACH	20×/0.4	2.29 μm [†]	6.3 μm [‡] 7.3 μm [†] 8.4 μm [§]	$ \delta_{C'} - \delta_{F'} \leq 2 \times \delta_{ob} = 4.58 \mu m$	[3]
Semiapochromat (FLU)	4×/0.13	21.65 μm [†]	62.8 μm [‡] 68.9 μm [†] 79.2 μm [§]	$ \delta_{C'} - \delta_{F'} \leq 2.5 \times \delta_{ob}$ = 54.12 μm	[4]
FLU	10×/0.3	4.07 μm [†]	11.8 μm [‡] 12.9 μm [†] 14.9 μm [§]	$ \delta_{C'} - \delta_{F'} \leq 2.5 \times \delta_{ob}$ = 10.16 μm	[5]
Apochromatic (APO)	5×/0.16	14.29 μm ^{††}	41.5 μm [‡] 45.5 μm [†] 52.3 μm [§]	$ \delta_{C'} - \delta_{F'} \leq \delta_{ob} = 14.29 \mu m$	[6]
APO	10×/0.30 10×/0.28	4.67 μm [†]	13.5 μm [‡] 14.8 μm [†] 17.1 μm [§]	$ \delta_{C'} - \delta_{F'} \leq \delta_{ob} = 4.67 \mu m$	[7]
APO	20×/0.4	2.29 μm [†]	6.6 μm [‡] 7.3 μm [†] 8.4 μm [§]	$ \delta_{C'} - \delta_{F'} \leq \delta_{ob} = 2.29 \mu m$	[8]
APO	40×/0.8	0.57 μm [†]	1.7 μm [‡] 1.8 μm [†] 2.1 μm [§]	$ \delta_{C'} - \delta_{F'} \leq \delta_{ob} = 0.57 \mu m$	[9]
APO	50×/0.55	1.21 μm [†]	3.5 μm [‡] 3.8 μm [†] 4.4 μm [§]	$ \delta_{C'} - \delta_{F'} \leq \delta_{ob} = 1.21 \mu m$	

* $\delta_{ob} = n\lambda_e/2NA^2$ as the optical depth of field as defined in ref. (International Organization for Standardization., 2013)

[†] e-line: 546.07 nm, [‡] F'-line: 479.99 nm, and [§] C'-line: 643.85 nm;

** FOV $\approx 1.78 \times n\lambda/NA^2$, as defined in Ref. (Olarte et al., 2018) considering the water refractive index of $n = 1.34$.

[1](Jorand et al., 2012; Di Domenico et al., 2018; Xiong et al., 2020), [2] (Kafian et al., 2020), [3] (Fahrbach & Rohrbach, 2010), [4] (Gualda et al., 2014; Stefaniuk et al., 2016; Müllenbroich, Turrini, et al., 2018), [5] (Cella Zanacchi et al., 2011; Olarte et al., 2012; Lavagnino et al., 2013; Bassi et al., 2015), [6] (Keller et al., 2010), [7] (Ritter et al., 2011; Fahrbach, Voigt, et al., 2013), [8] (Vettenburg et al., 2014; Meinert & Rohrbach, 2019; Suchand Sandeep et al., 2019), [9] (Dean et al., 2015; P. Zhang et al., 2016; Wu et al., 2016; Jia et al., 2019).

Finally, because APO objectives are chromatically corrected for red, green, and blue colors, one may suppose they are a good option for multicolor excitation LSMF (Ritter et al., 2011; Fahrbach, Gurchenkov, et al., 2013b; Fahrbach, Voigt, et al., 2013; Vettenburg et al., 2014; Dean et al., 2015; P. Zhang et al., 2016;

Wu et al., 2016; Jia et al., 2019; Meinert & Rohrbach, 2019; Suchand Sandeep et al., 2019) even when using Gaussian beams. However, the focus difference $|\delta_{C'} - \delta_{F'}|$ ranges from 2.29 to 14.29 μm , when using low NA's from 0.4–0.16. Those differences are significant enough for simultaneous imaging of structures below 6 μm , like the intracellular nuclei and microtubules differently tagged with fluorescent proteins in filamentous fungi like *Neurospora crassa* (Licea-Rodriguez et al., 2019) or *Sordaria macrospora*.

Therefore, based on the above discussion, there is no doubt that using different wavelength Gaussian beams for implementing multicolor LSFM is not ideal regardless of the objective chromatic correction. Additionally, it is worth mentioning that **Table 3** values are computed based on the nominal NA of each objective, but, in practice, the excitation beam does not fill the objectives' back aperture worsening the chromatic focal shifts. The above observations about the FOV's mismatches have not been discussed in the LSFM literature; therefore, this information must be considered when using focused Gaussian beams for multicolor LSFM imaging.

4.2.6 Lateral and axial resolution

The lateral and axial resolutions of each LSFM configuration were measured using the 0.16 μm fluorescent microbeads excited at 488 nm. Stacks of 200 planes were acquired in the axial direction (z-axis) with a step of 0.1 μm between each plane. The image stacks were taken near the edge of the quartz cuvette containing the agar-beads sample facing the detection objective to minimize possible image deterioration due to the refraction mismatch index. Several beads (~50) were selected as the ROI (not shown) to measure their volumetric intensity distributions.

Figure 26 shows the three LSFM configurations optical resolution measurements using the same microbead of a selected ROI. The microbead size was much smaller than the lateral resolution of the CO (around 0.48 μm); therefore, **Figure 26 a-c** and **g-i** show the measured lateral and axial point spread functions (PSFs), respectively. In **Figure 26 d-f**, the intensity profile traces at the central (z=0) plane confirms a similar lateral resolution of around 0.97 μm (on average) for the three configurations; this was expected since the lateral resolution depends mainly on the collection objective's optical properties. In contrast, the axial resolutions were expected to differ for each configuration because the PSF light-sheet microscopy is determined by the collection objective PSF and the light-sheet thickness (Engelbrecht &

Stelzer, 2006). The higher axial resolution was obtained for DSLM-Gaussian (**Figure 26 k**), and the lower was obtained for SPIM (**Figure 26 l**).

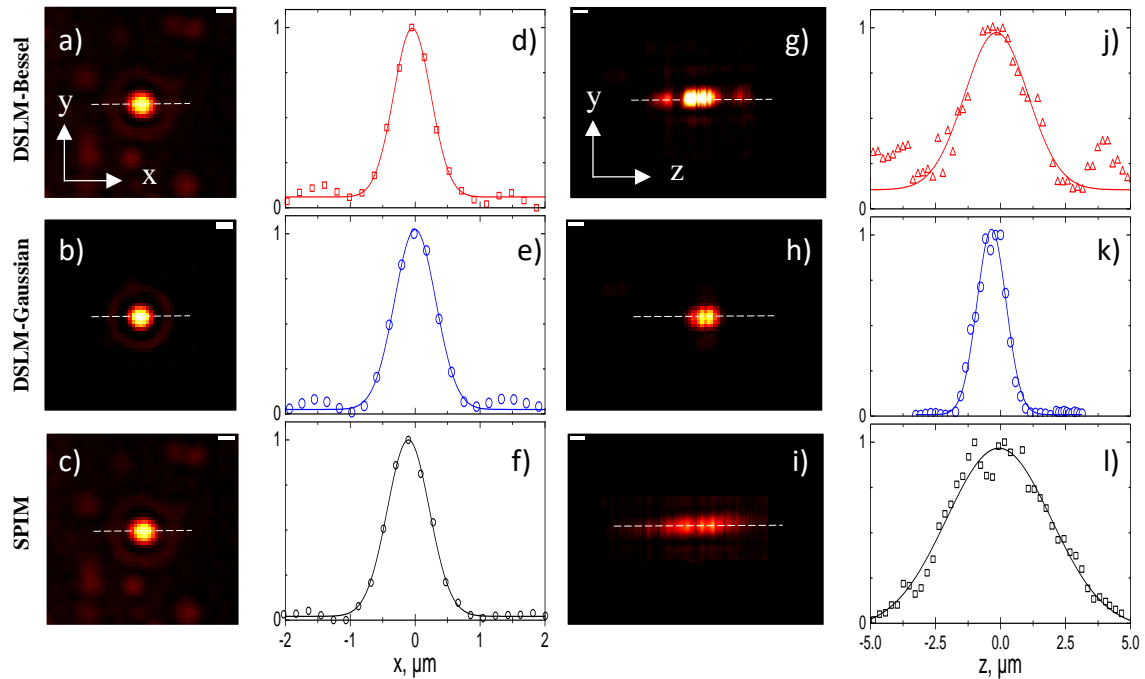


Figure 26 Lateral and axial resolution measurement for the three LFSM configurations using $0.16\ \mu\text{m}$ fluorescent beads excited with the laser at $488\ \text{nm}$. Images of the point spread functions (PSFs) measured in both directions: a-c) lateral and g-i) axial. Normalized intensity profiles of the PSF in the d-f) lateral and j-l) axial directions measured along the dashed lines indicated in Figures. a-c) and g-i), respectively. The solid lines represent the corresponding fits of the experimental intensity profile traces. The lateral and axial average PSF widths measured at the FWHM value are summarized in table 3. Scale bar $1\ \mu\text{m}$

Meanwhile, the axial resolution of the DSLM-Bessel (**Figure 26 j**) was between the first two configurations. The lateral and axial resolution values measured at FWHM for the three LFSM modalities are summarized in **Table 4**. Notice that the resolutions were also measured using the same $0.16\ \mu\text{m}$ fluorescent microbeads excited at $445\ \text{nm}$ (images not shown).

Table 4. Lateral and axial average PSF widths at the FWHM for the different LFSM configurations.

LFSM Configurations	CO	Lateral PSF (μm)	Axial PSF (μm)
<i>DSLM Bessel</i>	50X/NA 0.55	$0.98\pm 0.02^*$ / $0.98\pm 0.02^\dagger$	$3.2\pm 0.2^*$ / $2.9\pm 0.4^\dagger$
	20X/NA 0.40	$1.90\pm 0.02^*$ / $1.90\pm 0.02^\dagger$	$5.2\pm 0.2^*$ / $5.4\pm 0.2^\dagger$
<i>DSLM-Gaussian</i>	50X/NA 0.55	$0.98\pm 0.03^*$ / $0.97\pm 0.2^\dagger$	$1.3\pm 0.3^*$ / $1.2\pm 0.3^\dagger$
	20X/NA 0.40	$1.90\pm 0.02^*$ / $1.90\pm 0.02^\dagger$	$2.3\pm 0.3^*$ / $2.6\pm 0.2^\dagger$
<i>SPIM</i>	50X/NA 0.55	$0.95\pm 0.05^\dagger$	$4.5\pm 0.2^\dagger$

* $488\ \text{nm}$, $^\dagger 445\ \text{nm}$. Measured using fluorescent microbeads of $0.16\ \mu\text{m}$.

4.2.7 Axial resolution variation over the FOV

LSFM resolution strictly depends on the PSF of the collection objective and the excitation light-sheet thickness (Engelbrecht & Stelzer, 2006), which is not preserved over the entire objective FOV. Therefore, both the optical sectioning and the axial resolution depend on the sample's location over the FOV. **Figure 27** shows the axial resolution variation over the FOVs of the different LSFM configurations. **Figure 27 a-c** shows maximum intensity projection (MIP) images of the 0.16 μm fluorescent beads. The MIPs are produced from 200 planes acquired at 0.1 μm -steps along z-direction using a 50X (0.55 NA) collection objective; the imaged area was 122 x 100 μm^2 . Three zones over the maximum FOV, i.e., around the FWHM of the Bessel beam axial profile, are selected and tagged as Z_1 , Z_2 , and Z_3 . The zones are located at the left, center, and right of the FOV, respectively. The non-uniform light-sheet thickness of Gaussian beams induces lateral image deformations due to higher axial blurring (see **Figure 27 b** and **c**); i.e., the axial PSF of the CO increases at the FOV side locations. While this effect is mainly observed when imaging large samples, for instance, beyond DSLM-Gaussian FOV size (Dean et al., 2015), it is still present to a minimum extent for smaller samples, as shown next.

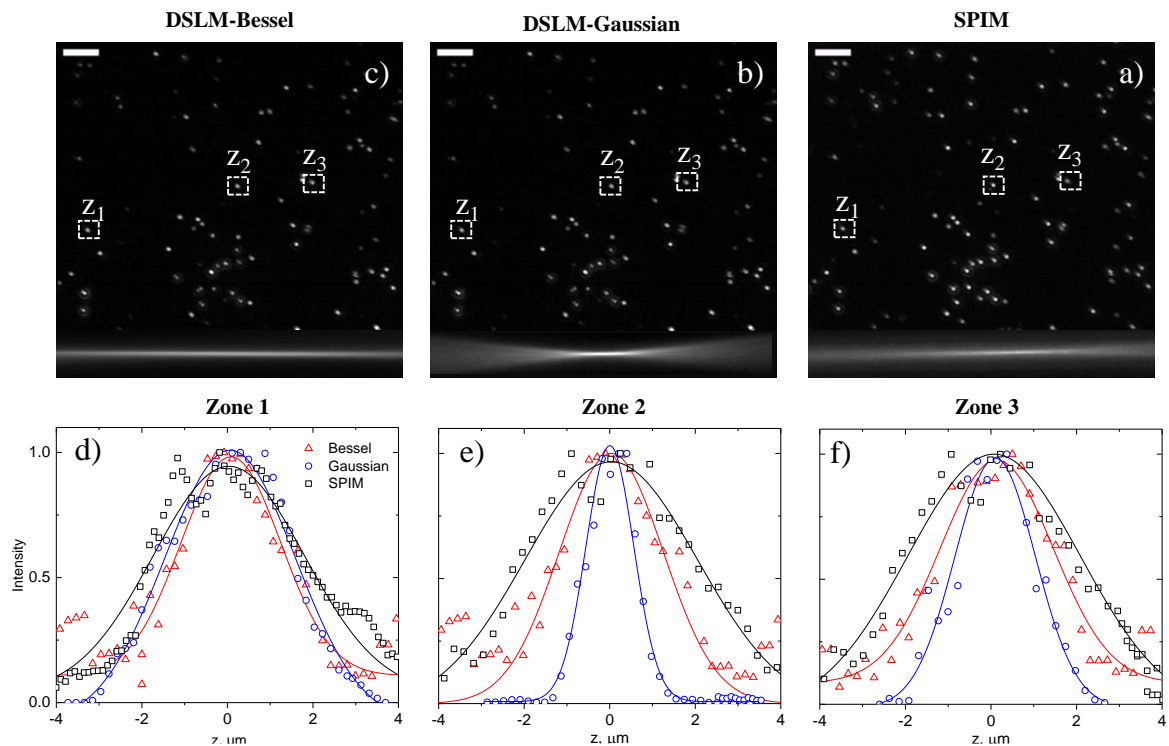


Figure 27. Axial resolution variation over the different LSFM configurations FOV. Maximum intensity projection images for DSLM-Bessel (a), DSLM-Gaussian (b), and SPIM (c). A total of 200 planes are acquired with a step of 0.1 μm along the z-direction. The axial PSF profile traces were obtained at Zone 1 (d), Zone 2 (e), and Zone 3 (f); these zones are indicated with white squares in (a-c). The red open triangle traces correspond to DSLM-Bessel; the blue open circles are for DSLM-Gauss, and the black open squares for SPIM. The fits of the experimental intensity profile traces are represented by the solid lines with the corresponding color. Scale bar 10 μm .

Figure 27 d-f compares the axial PSF intensity profile traces obtained at the three zones for DSLM-Bessel (red open triangles), DSLM-Gaussian (blue open circles), and SPIM (black open squares), configurations, respectively. The fits of the experimental intensity profile traces are represented by the solid lines with the corresponding color. The better axial resolution is around $1.3\ \mu\text{m}$ achieved by DSLM-Gaussian at the central Z_2 zone (see the blue trace in **Figure 27e**); however, such a fair resolution drops three and two times at the lateral zones Z_1 and Z_3 (see the blue traces in **Figure 27 d** and **f**). In contrast, both SPIM and DSLM-Bessel preserve considerably their axial resolution at about $4.5\ \mu\text{m}$ and $3.2\ \mu\text{m}$, respectively. Therefore, the DSLM-Bessel configuration is better for imaging large samples even over SPIM and overcomes the possible lateral image deformations due to axial deblur.

4.3 Light Sheet *Sordaria macrospora* imaging

Sordaria macrospora is a model fungus that has been used to study fruiting body development over the last decades (Teichert et al., 2020). However, little is known about molecular determinants for tissue differentiation inside the perithecium and the formation of the Dikaryon (a collection of cells with exactly two nuclei vital for meiosporangium formation). Here, we proposed that using LSFM in combination with marker proteins would be of great value to visualize the 3-D dynamics of nuclei inside the pear-shaped perithecia with a size of about $300\ \mu\text{m}$.

To compare the three LSFM configurations imaging on the fruiting bodies of *Sordaria macrospora* was carried out at different stages during sexual development. The first sample, with dimensions around the DSLM-Gaussian FOV size (named small sample), was collected after eight days of development. Meanwhile, with dimensions beyond the DSLM-Gaussian FOV size (called large sample), the second sample had 16 days of development. Notice that the small samples are taken at early development stages while the large samples are taken at later stages.

4.3.1 Small samples

Figure 28 compares the three LSFM imaging configurations using the small sample. The images shown are a maximum intensity projection (MIP) taken under similar conditions as in **Figure 27**. Projections over 200 planes were acquired at $0.1\ \mu\text{m}$ steps using the 50X CO, and the total imaged area was $122 \times 100\ \mu\text{m}^2$.

Figure 28 a-b shows the MIP images of the cell wall (blue) and nuclei (magenta) acquired with DSLM-Bessel configuration. **Figure 28 c** is the corresponding merged image. Similarly, the MIP images acquired with DSLM-Gaussian and SPIM configurations are shown in **Figure 28 d-f** and **Figure 28 g-i**, respectively. The white arrows in **Figure 28 b, e, and h** indicate the incoming light-sheet direction.

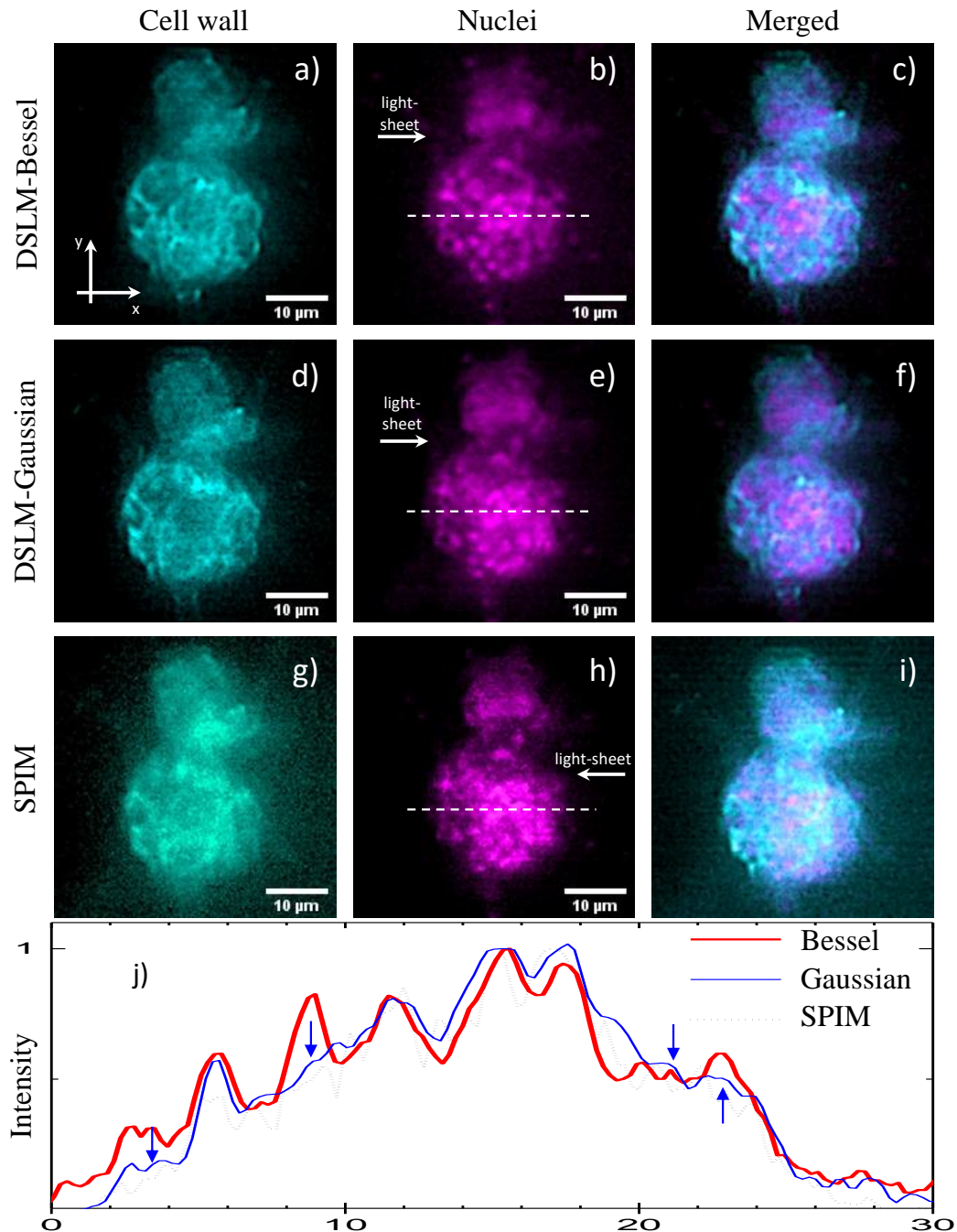


Figure 28 MIP images of a living perithecium of *Sordaria macrospora* after eight days of growth expressing the tdTomato fluorescent protein in the nuclei and the cell walls stained with SF7 acquired with the different LSFM configurations. a-c) DSLM-Bessel, d-f) DSLM-Gaussian, and g-i) SPIM; j) Intensity profile obtained from the dotted lines in figures b), e), and h). The white arrows in b), e), and h) indicate the incoming light-sheet direction and the blue arrows indicate structures with lower contrast in figure j).

Similar results were obtained with DSLM-Bessel and -Gaussian configurations for the perithecial cell wall (**Figure 28 a and d**) within the short FOV of the latter. However, the images are slightly better defined for the nuclei when using DSLM-Bessel due to the exciting beams' self-healing properties and larger FOV. **Figure 28j** shows the intensity profiles of **Figure 28 b and e** (at the white dotted horizontal lines), revealing their image contrast and resolution as the beam propagates through the sample. Notice how the contrast in DSLM-Bessel is slightly better than DSLM-Gaussian despite the well-known lateral intensity lobes contribution of the Bessel beams. Here, the light-sheets generated with Gaussian beams are diffraction-deformed when they penetrate deeper into the sample; thus, the image quality is compromised (see solid blue curve in **Figure 28j**). Meanwhile, for Bessel beams, the diffraction artifacts are minimized.

Even though the lateral resolution was approximately the same for the three configurations (see **Table 4**), the images acquired with SPIM (**Figure 28 g-i**) present the lowest quality in terms of contrast and resolution. This low quality can be attributed to the SPIM's low optical sectioning capability and the beam scattering occurring across the sample. In other words, since the sample size is comparable to the light-sheet thickness, the fluorescence signal coming from multiple nonselective planes is integrated at the image plane. Overall, **Figure 28** demonstrates that DSLM-Bessel competes fairly with DSLM-Gaussian configuration for multicolor imaging purposes of samples with dimensions comparable with the FOV size.

4.3.2 Large samples

Figure 29 compares the DSLM-Gaussian vs. DSLM-Bessel configuration using a larger sample. The images in **Figure 29a and b** are also MIPs of 200 planes, acquired with a step of 0.1 μm along the z-direction but using a lower magnification CO (20x, NA=0.40). The imaged area is around 315 X 250 μm^2 ; i. e., approximately eight times larger than the FOV of DSLM-Gaussian. **Figure 29b** shows how DSLM-Bessel covers a larger FOV and also how DSLM-Bessel resolves large and small structures such as the perithecium body and the surrounding hyphae. Instead, DSLM-Gaussian resolves only the perithecium body structures. Additionally, for DSLM-Bessel, the sample structures are well defined with a comparable optical axial resolution to DSLM-Gaussian all over the FOV (as discussed in **Figure 28 d-f**).

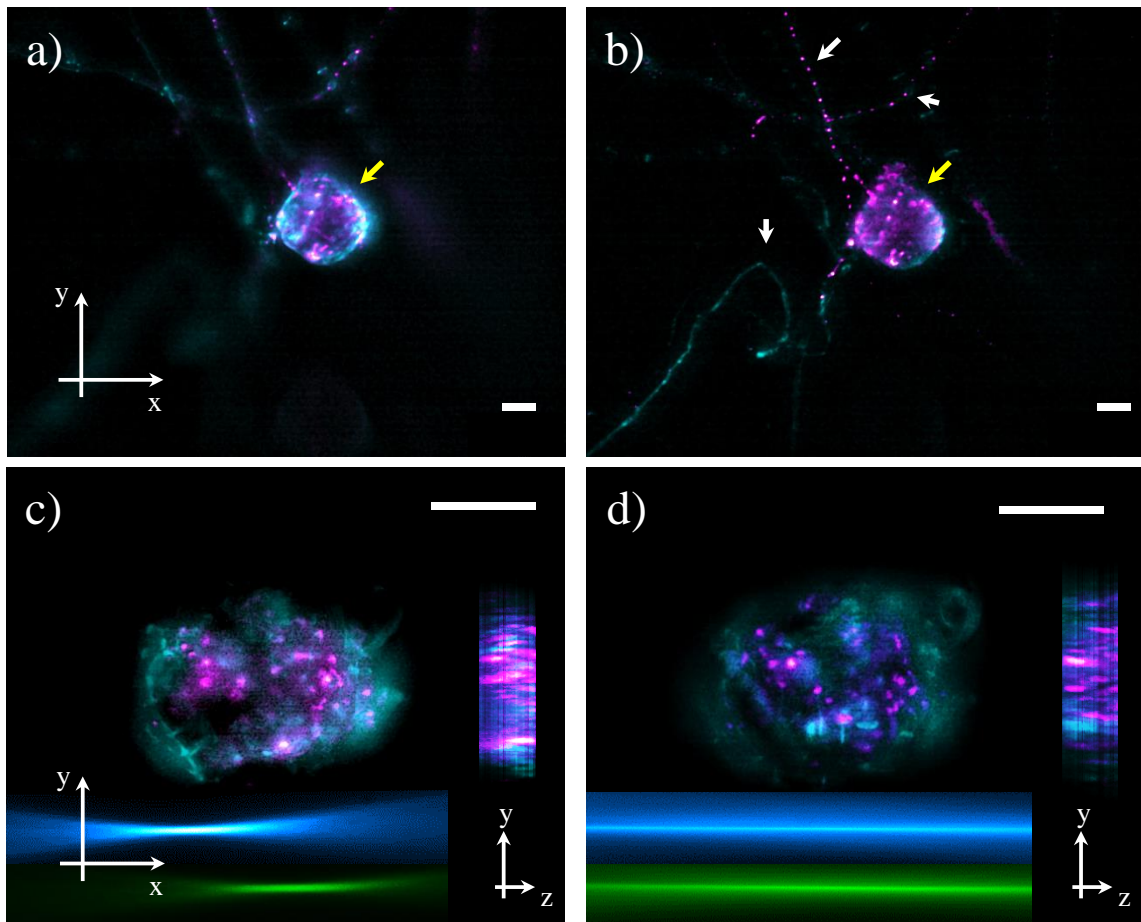


Figure 29 MIP images of a living perithecium of *Sordaria macrospora* of 16-days development expressing the tdTomato fluorescent protein in the nuclei and the cell wall stained with SF7 acquired with DSLM-Gaussian (a, c) and DSLM-Bessel (b, d) configurations. The collection objectives utilized were 20X (a, b) and 50X (c, d). In figures (c,d), the right and bottom insets are the in-depth yz-images and the focused Gaussian and Bessel beams, respectively. Scale bar 20 μm

Figure 29 c and **d** compare DSLM- Gaussian and Bessel images over a different perithecium body but using the higher magnification 50× collection objective. The inherent problems of the excitation Gaussian beams become more evident in **Figure 29 c** as they propagate through the sample. Their high diffractive properties distort the light sheets, and the chromatic focusing shifts of the 445 nm and 561 nm beams produce non-coincident focused images along the FOV. For the DSLM-Bessel images instead, those problems are noticeably minimized.

In summary, based on the presented results, large FOV multicolor imaging using Bessel-LSFM beams shows high potential for *in vivo* studies in developmental biology. Studies about the origin of the fungal Dikaryon and the internal structural and cellular dynamics of the fruiting bodies are anticipated.

4.3.3 *Sordaria macrospora* imaging with LSFM vs. confocal microscopy

To compare the multicolor Bessel LSFM system's capabilities against a commercial confocal laser scanning microscope (CLSM) Olympus FLUOVIEW FV1000. **Figure 30** shows the Z-projections of 3D images of growing perithecia. The confocal image (**Figure 30a**) was acquired using an oil immersion objective with a higher numerical aperture (NA=1.42), i.e., almost three times higher than that used in DSLM-Bessel (NA=0.40). Because the Bessel DSLM system's acquisition rate is around ten times faster than the confocal system, the obtained image under this system is less deblurred (see **Figure 30b**). While the confocal system integrates the moving structures in 8 images/sec (see white arrows), the LSFM system can acquire images at a rate of 200 images/sec; therefore, typical moving structures of 0.52 μm /sec are better resolved using LSFM.

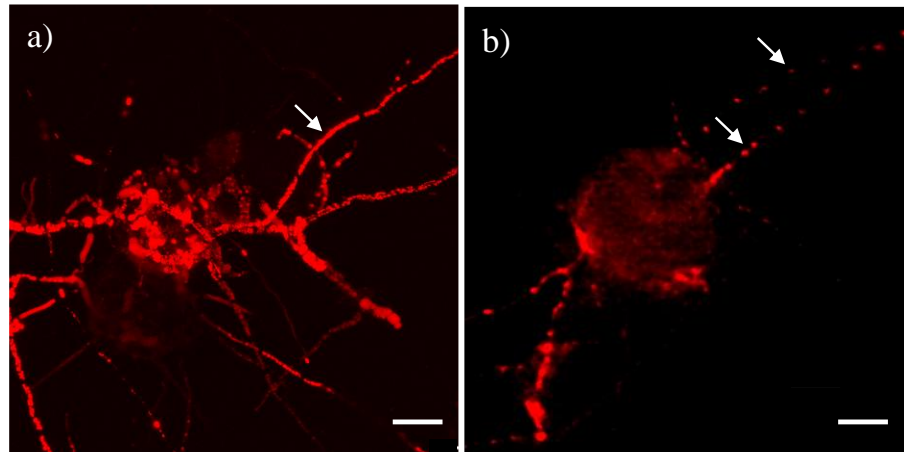


Figure 30 Z-projection images of a living perithecium of *Sordaria macrospora* acquired with a) commercial CLSM system (NA=1.42) and b) DSLM-Bessel configuration (NA=0.40). The scale bar is 20 μm .

4.4 Bessel vs. Gaussian beam focusing under the same objective lens

Beam propagation simulations were performed to study Bessel and Gaussian-light-sheets excitation under the same excitation objective. Two cases were considered for this study: *i*) when both beams are focused under the same NA, and *ii*) when both beams have the same DoF (same FOV when viewed from the CO). The simulations were performed using the propagation method implemented by Becker et. al. (Becker et al., 2019) (see Section 2.6 and 3.5). **Figure 31** summarizes the results for beam propagation simulations at a 488 nm wavelength using a NA of 0.16 for both Bessel and Gaussian beams and a 0.05 NA only for the Gaussian beam. The simulation for the other two wavelengths, at 445 nm, and 561 nm, are shown in Appendix C.

4.4.1 Bessel vs. Gaussian beam under the same NA

Figure 31 a and **b** compare the focused Bessel and Gaussian beams propagation with the same NA ($= 0.16$). Here, a ring aperture of 6 mm outer diameter and 5.84 mm internal diameter are placed at the lens entrance for the Bessel beam simulation. For the Gaussian beam simulation, a diameter of 6 mm (at the beam FWHM intensity) is utilized. Meanwhile, **Figure 31 d** traces the beam profiles along the z-axis to estimate the achieved FOVs of the LSFM system. For this case, the DoF of the Bessel beam (dash line) is nine times larger than the one obtained with a Gaussian beam (solid dark line), as observed in the experiments (see **Table 2**). Therefore, the FOV of the LSFM system is nine times larger for Bessel beams than for the Gaussian beams. Notice, however, that the beam waist at the focus, i.e., the light-sheet thickness, is very similar for the two beams, which is appreciated in **Figure 31e** if the Bessel beam's central lobe is considered. Therefore, a similar axial resolution would be expected for this case, as demonstrated below.

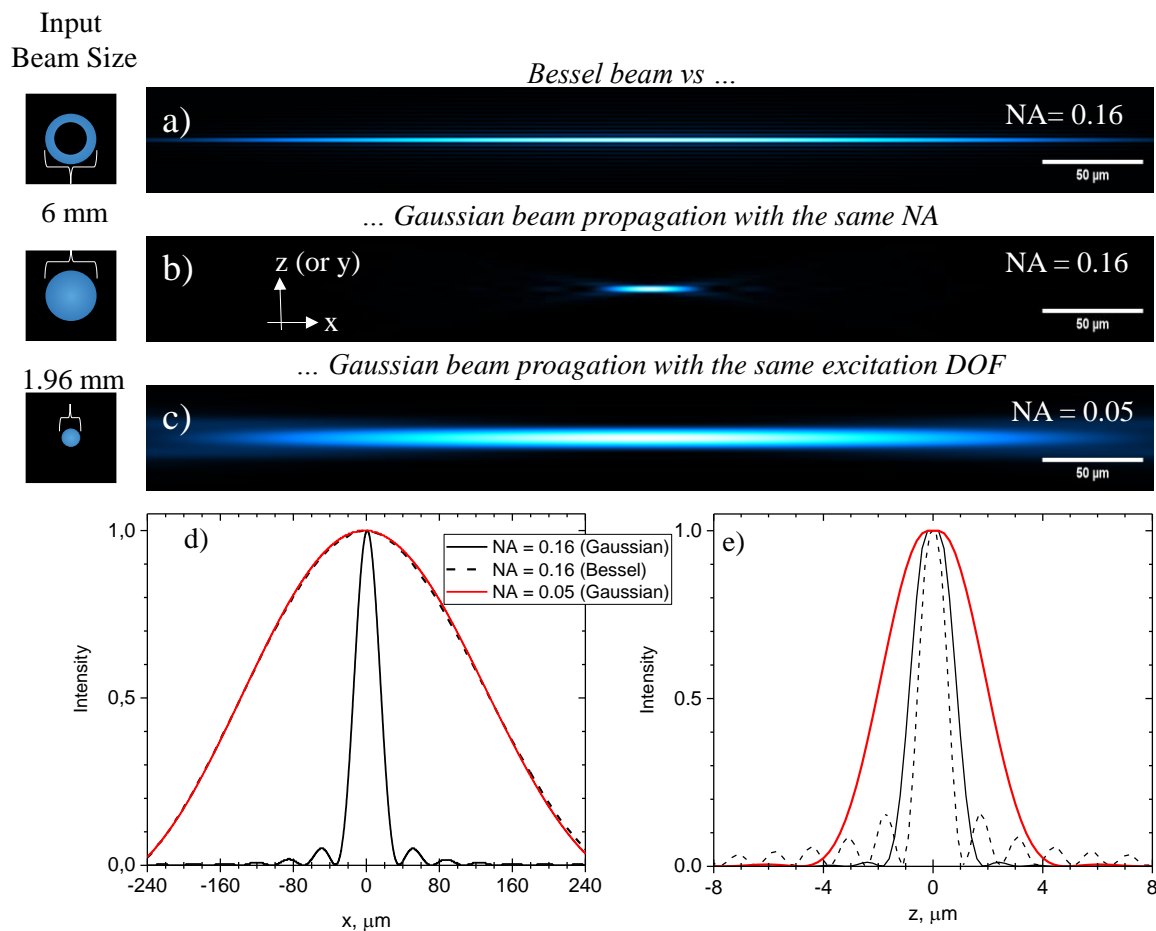


Figure 31 Bessel (a) and Gaussian (b) beam propagation under a 0.16 NA objective. Both cases are under experimental settings. (c) Gaussian beam propagation through a 0.05 NA for obtaining a similar DoF as in the focused excitation Bessel beam. Normalized intensity profile traces along the x-direction (d) and z-direction (e) of figures a, b and c. The beam's propagation is simulated at 488 nm in free space.

4.4.2 Bessel vs. Gaussian beam under the same FOV

Figure 31 a and **c** compare the focused Bessel and Gaussian beams propagation with equal DoF; so that the FOV of the LSFM system would be the same for both types of beams. Notice that, when using the same EO to implement both DSLM-Bessel and Gaussian configurations, the requirement to have the same FOV is to reduce the NA of the focused Gaussian beam. However, it is worth mentioning that achieving this in the experiment is challenging; it implies reducing the NA to 0.05 by reducing the Gaussian beam to 1.96 mm at the rear EO (around eight times smaller at the GM). Therefore, this scenario is simulated here instead. As expected, when the NA is reduced, the FOV increases and the lateral resolution decreases (see **Figure 31 d and e**, solid red lines) indicating that Bessel beams are a better option for large FOV imaging despite the background signal caused for the Bessel outer rings intensity.

4.4.3 LSFM axial resolution dependence on the collection objective DoF

Notice that Bessel light-sheet thickness measurements depend on the collection objective depth of field. The axial resolution is affected when a CO with larger DoF's is utilized since fluorescence excited from Bessel side lobes adds to the image taken to trace the Δy beams profile. **Figure 32** shows the simulation images for a Bessel beam at different collection objective NA's to investigate that. The images integrate the intensity of the planes that the CO would observe along its DoF.

Additionally, **Figure 33** shows simulations of Bessel and Gaussian beams' measured axial widths (Δy_s) for different collection objective NA. For Bessel beams, the axial width (and so the optical sectioning) is reduced as higher NA are employed. In other words, since the higher the NA, the shorter the DoF; therefore, less focused planes are integrated along the z-direction, discriminating the Bessel side lobes (see **Figure 33 a**). Meanwhile, the light-sheet thickness remains constant for Gaussian beams regardless of the collection the NA objective (see **Figure 33 b**). The CO DoF effect explains why a comparable optical axial resolution is obtained in **Figure 29 c** and **d** despite that Bessel beams have bigger Δy 's.

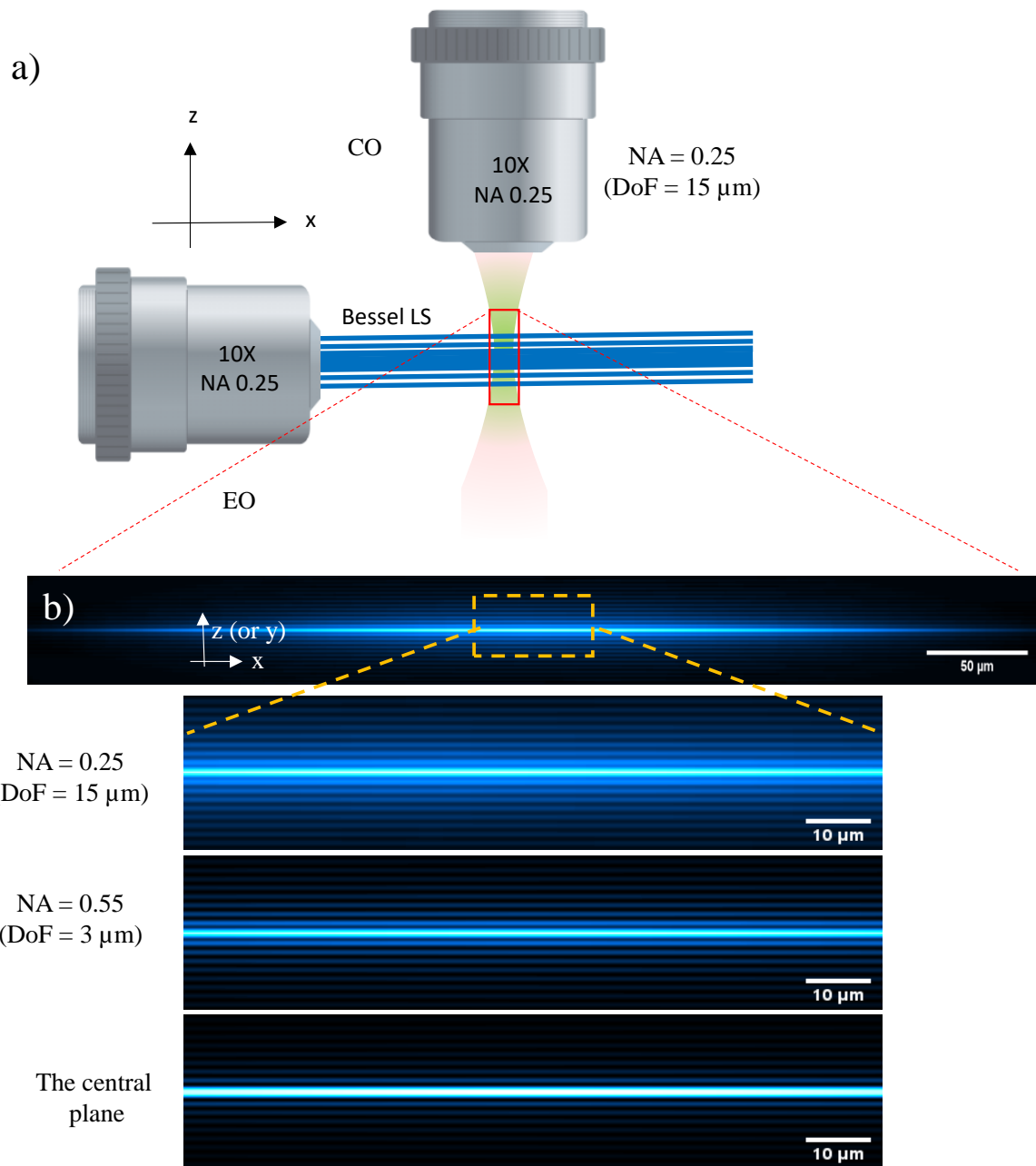


Figure 32. LSFM Image and axial beam profile dependence on the collection objective Numerical Aperture. (a) Experimental scheme to demonstrate the effect of the DoF (b) XY-plane of Bessel beam intensity image integrated over different collection objective Numerical Apertures (i.e., different DOF, as indicated).

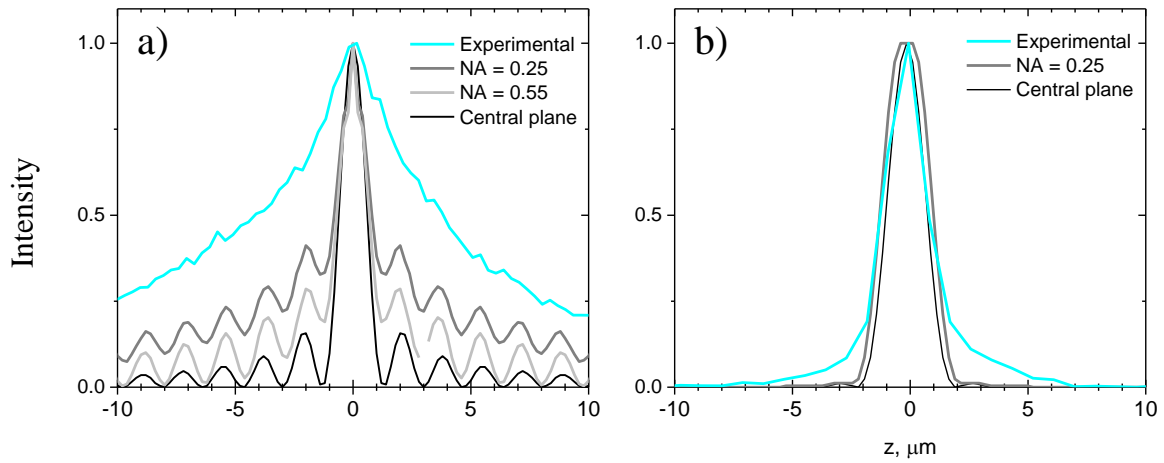


Figure 33 Beam profiles traced along the axial (z-direction) of the image simulation in **Figure 32** compared with the experimental results. (a) Bessel, (b) Gaussian. The cyan trace in (b) and (c) corresponds to the experimental axial beam profiles of **Figure 25 g** and **h**, respectively. Gray line: simulation of the axial beam profile from an objective with NA = 0.25. Light gray line: simulation of the axial beam profile from an objective with NA = 0.55 and the central plane black line.

Chapter 5. Conclusions

This doctoral project aimed to perform a comparative study between multiple Bessel and Gaussian light-sheet fluorescence excitations for a large field of view multicolor imaging. The study considered both light-sheet fluorescence excitations under the same excitation path utilizing the same excitation objective

Based on the results presented in Chapter 4, several conclusions can be drawn from the light-sheet characterization, the imaging of biological samples, and the beam propagation simulations.

5.1 Light-sheets characterization

- Multicolor Bessel light-sheet excitation is better suited for large FOV multicolor imaging than using Gaussian light-sheets excitation for the same purpose. Apart from the well-known property to overcome self-diffraction image artifacts, Bessel beams minimize the chromatic FOV mismatches effects and alleviate lateral image deformations.
- A different focus occurs between Gaussian and Bessel excitations when implementing multicolor DSLM imaging under the same microscope excitation objective. The focal shifts occur between the waist (at the focal points) of the Gaussian beams triplet and the corresponding waist of the Bessel beams. The non-diffractive nature of Bessel beams provokes such retardation. Consequently, the FOVs of DSLM-Bessel and DSLM-Gaussian configurations are not colocalized.
- Another shift occurs between the different colored beams within each DSLM configuration. Such chromatic displacements are unavoidably inherited by the excitation objective's chromatic aberration and are observed mainly for the DSL-Gaussian configuration. Our results indicate that such a shift occurs regardless of the excitation objective chromatic correction utilized. Therefore, a reduced effective field of view (FOV_{eff}) must be considered when performing multicolor imaging.
- Single-color Gaussian light-sheet excitation is better suited for LSFM imaging when a short FOV visualization is required. Under this configuration, the best axial resolution is obtained. However, precautions must be taken when attempting to perform multicolor LSFM imaging using multiple

Gaussian beams due to the reduction in the effective FOV_{eff} and the different focusing of the multicolor excitation light-sheets.

5.2 Biological samples imaging

- Our results demonstrate that multicolor DSLM-Bessel configuration is potentially applicable in cell biology studies of living organisms, including fungal multicellular development and host-pathogen interactions. In addition, this work represents a cost-effective LSFM system capable of performing large FOV imaging for up to three different colors using a single-camera detection.
- Although a better axial resolution is obtained under the DSLM-Gaussian configuration, the images acquired for small and large samples using DSLM-Bessel in *S. macrospora* demonstrated similar optical resolutions and image contrast comparable to DSLM-Gaussian but at larger FOVs.

5.3 Beam propagation simulations

- The simulation of the Bessel and Gaussian beams propagation and focusing under the same numerical aperture ($NA = 0.16$) utilized in the experiments yielded two fundamental results. First, Bessel's FOV size is nine times larger than that obtained with Gaussian beams. Second, the light-sheet thickness is very similar for both beams (when the Bessel beam's thickness is measured at the central beam lobe).
- The simulation comparing the focused Bessel and Gaussian beams propagation with equal depth of field shows that despite the FOV of the Gaussian beam increases, its lateral light-sheet thickness also increases, being higher than that obtained for the Bessel beam. This result demonstrates that Bessel beams are better for achieving large FOV imaging despite the background signal caused by the Bessel beam side lobes intensity.
- Finally, the simulations for the axial resolution dependence on the collection objective depth of focus indicate that the DSLM-Bessel axial resolution can be improved when a larger NA is

employed. As a higher NA is utilized for the collection objective, a shorter DoF is achieved; therefore, less planes are integrated along the axial direction, discriminating the Bessel beam side lobes. This result demonstrates that *S. macrospora* imaging under the DSLM configuration using Bessel and Gaussian beams showed similar optical axial resolutions and contrast when a 50X, NA:0.55 collection objective was employed.

5.4 Future work

Regarding the *S. macrospora* sample imaging, it would be interesting to continue the study involving the growth process by taking 4D images and 2D videos. For the LSFM collection path, increasing the collection objective's depth of field would be desirable while keeping high NA to take high-resolution images of thick specimens. For the excitation path, implement the super-resolution technique of stimulated emission depletion (STED), combining first-order with zero-order Bessel beam to increase the axial resolution. With respect to the images processing, use an adjusted PSFs according to the type of illumination to obtain a better axial resolution

5.5 Publications derived from the thesis

Peer-reviewed Papers:

1. **Luna-Palacios, Y. Y.**, Licea-Rodriguez, J., Camacho-Lopez, M. D., Teichert, I., Riquelme, M., Rocha-Mendoza, I., Multicolor light-sheet microscopy for a large field of view imaging: A comparative study between Bessel and Gaussian light-sheets configurations. *J. Biophotonics* 2022, e202100359. <https://doi.org/10.1002/jbio.202100359>
2. Rodríguez-Arzate CA, Martínez-Mendoza ML, Rocha-Mendoza I, **Luna-Palacios Y, Y** Licea-Rodríguez J, Martínez-Torres A. Morphological and Calcium Signaling Alterations of Neuroglial Cells in Cerebellar Cortical Dysplasia Induced by Carmustine. *Cells*. 2021; 10(7):1581. <https://www.mdpi.com/2073-4409/10/7/1581>

Press release paper:

Deep insights into a living fungus. <https://news.rub.de/english/press-releases/2022-03-15-biology-deep-insights-living-fungus>

Conference paper:

Y. Y. Luna-Palacios, M. D. Camacho-Lopez, J. Licea-Rodriguez, M. Riquelme, and I. Rocha-Mendoza, "Multicolor light-sheet microscopy using Bessel beams," in *Imaging and Applied Optics Congress*, OSA Technical Digest (Optica Publishing Group, 2020), paper IF3E.5.

Conferences:

Y. Y. Luna-Palacios, J. Licea-Rodriguez, and I. Rocha-Mendoza, "Multi-fluorescence light sheet microscopy using Bessel beams for biophotonics applications", ICFO-UNAM-UNIANDDES International School on the Frontiers of Light Queretaro. October 2019

J. Licea-Rodriguez, **Y. Y. Luna-Palacios**, and I. Rocha-Mendoza, "The light sheet fluorescence microscope at cicese: current studies", in X Iberoamerican Optics Meeting / XIII Latinamerican Meeting on Optics, Lasers and Applications/Mexican Optics and Photonics Meeting Cancún, México. September 2019.

References

- Abdeladim, L., Matho, K. S., Clavreul, S., Mahou, P., Sintes, J. M., Solinas, X., Arganda-Carreras, I., Turney, S. G., Lichtman, J. W., Chessel, A., Bemelmans, A. P., Loulier, K., Supatto, W., Livet, J., & Beaurepaire, E. 2019. Multicolor multiscale brain imaging with chromatic multiphoton serial microscopy. *Nature Communications*, 10(1), 1–14.
- Abramowitz, M., Spring, K. R., Keller, H. E., & Davidson, M. W. 2002. Basic Principles of Microscope Objectives. *BioTechniques*, 33(4).
- Alda, J., Alda, J., Alda, J., & Alda, J. 2003. Laser and Gaussian beam propagation and transformation. In *Encyclopedia of Optical Engineering* (1st ed., pp. 999–1013). Marcel Dekker, Inc.
- Alejandra, C., Lizeth, M., Rocha-mendoza, I., Luna-palacios, Y., & Licea-rodr, J. 2021. Morphological and Calcium Signaling Alterations of Neuroglial Cells in Cerebellar Cortical Dysplasia Induced by Carmustine. *Cells*, 10(1581), 1–18.
- Andilla, J., Jorand, R., Olarte, O. E., Dufour, A. C., Cazales, M., Montagner, Y. L. E., Ceolato, R., Riviere, N., Olivo-Marin, J. C., Loza-Alvarez, P., & Lorenzo, C. 2017. Imaging tissue-mimic with light sheet microscopy: A comparative guideline. *Scientific Reports*, 7(March), 1–14.
- Barrón Ortiz, D. 2021. *Caracterización bidimensional de la temperatura en un sensor térmico basado en la fluorescencia de conversión ascendente en compuestos poliméricos de tierras raras*. Tesis de Maestría. Centro de Investigación Científica y de Educación Superior de Ensenada, Baja California.
- Bassi, A., Schmid, B., & Huisken, J. 2015. Optical tomography complements light sheet microscopy for in toto imaging of zebrafish development. *Development (Cambridge)*, 142(5), 1016–1020.
- Becker, K., Saghafi, S., Pende, M., Sabdyusheva-Litschauer, I., Hahn, C. M., Foroughipour, M., Jährling, N., & Dodt, H. U. 2019. Deconvolution of light sheet microscopy recordings. *Scientific Reports*, 9(1), 1–14.
- Brzobohatý, O., Cižmár, T., & Zemánek, P. 2008. High quality quasi-Bessel beam generated by round-tip axicon. *Optics Express*, 16(17), 12688.
- Can-Uc, B., Montes-Frausto, J. B., Juarez-Moreno, K., Licea-Rodriguez, J., Rocha-Mendoza, I., & Hirata, G. A. 2018. Light sheet microscopy and SrAl₂O₄ nanoparticles codoped with Eu²⁺/Dy³⁺ ions for cancer cell tagging. *Journal of Biophotonics*, 11(6), 1–8.
- Cella Zanicchi, F., Lavagnino, Z., Perrone Donnorso, M., Del Bue, A., Furia, L., Faretta, M., & Diaspro, A. 2011. Live-cell 3D super-resolution imaging in thick biological samples. *Nature Methods*, 8(12), 1047–1050.
- Cizmar, T. 2006. *Optical traps generated by non-traditional beams*. Masaryk University.

- Dean, K. M., Roudot, P., Welf, E. S., Danuser, G., & Fiolka, R. 2015. Deconvolution-free Subcellular Imaging with Axially Swept Light Sheet Microscopy. *Biophysical Journal*, 108(12), 2807–2815.
- Di Domenico, G., Ruocco, G., Colosi, C., DelRe, E., & Antonacci, G. 2018. Cancellation of Bessel beam side lobes for high-contrast light sheet microscopy. *Scientific Reports*, 8(1), 1–7.
- Duocastella, M., & Arnold, C. B. 2012. *Bessel and annular beams for materials processing*. 15, 1–15.
- Durnin, J., Miceli, J., & Eberly, J. H. 1987. Diffraction-free beams. *Physical Review Letters*, 58(15), 1499–1501.
- Engelbrecht, C. J., & Stelzer, E. H. 2006. Resolution enhancement in a light-sheet-based microscope (SPIM). *Optics Letters*, 31(10), 1477.
- Engh, I., Nowrousian, M., & Kück, U. 2010. *Sordaria macrospora*, a model organism to study fungal cellular development. *European Journal of Cell Biology*, 89(12), 864–872.
- Fahrbach, F. O., Gurchenkov, V., Alessandri, K., Nassoy, P., & Rohrbach, A. 2013a. Light-sheet microscopy in thick media using scanned Bessel beams and two-photon fluorescence excitation. *Optics Express*, 21(11), 13824.
- Fahrbach, F. O., Gurchenkov, V., Alessandri, K., Nassoy, P., & Rohrbach, A. 2013b. Self-reconstructing sectioned Bessel beams offer submicron optical sectioning for large fields of view in light-sheet microscopy. *Optics Express*, 21(9), 11425.
- Fahrbach, F. O., & Rohrbach, A. 2010. A line scanned light-sheet microscope with phase shaped self-reconstructing beams. *Optics Express*, 18(23), 24229.
- Fahrbach, F. O., Simon, P., & Rohrbach, A. 2010. Microscopy with self-reconstructing beams. *Nature Photonics*, 4(11), 780–785.
- Fahrbach, F. O., Voigt, F. F., Schmid, B., Helmchen, F., & Huisken, J. 2013. Rapid 3D light-sheet microscopy with a tunable lens. *Optics Express*, 21(18), 21010.
- Gao, L., Shao, L., Chen, B. C., & Betzig, E. 2014. 3D live fluorescence imaging of cellular dynamics using Bessel beam plane illumination microscopy. *Nature Protocols*, 9(5), 1083–1101.
- Garcia-ortiz, C. E., Pisano, E., & Coello, V. 2017. Description and characterization of plasmonic Gaussian beams. *Journal of Optics (United Kingdom)*, 085001.
- Girkin, J. M., & Carvalho, M. T. 2018. The light-sheet microscopy revolution. *Journal of Optics (United Kingdom)*, 20(5).
- Gualda, E. J., Simão, D., Pinto, C., Alves, P. M., & Brito, C. 2014. Imaging of human differentiated 3D neural aggregates using light sheet fluorescence microscopy. *Frontiers in Cellular Neuroscience*, 8(08), 1–10.

- Hoyer, P., De Medeiros, G., Balázs, B., Norlin, N., Besir, C., Hanne, J., Kräusslich, H. G., Engelhardt, J., Sahl, S. J., Hell, S. W., & Hufnagel, L. 2016. Breaking the diffraction limit of light-sheet fluorescence microscopy by RESOLFT. *Proceedings of the National Academy of Sciences of the United States of America*, 113(13), 3442–3446.
- Huisken, J., & Stainier, D. Y. R. 2009. Selective plane illumination microscopy techniques in developmental biology. *Development*, 136(12), 1963–1975.
- Huisken, J., Swoger, J., Del Bene, F., Wittbrodt, J., & Stelzer, E. H. K. 2004. Optical sectioning deep inside live embryos by selective plane illumination microscopy. *Science*, 305(5686), 1007–1009.
- International Organization for Standardization. 2013. *ISO 19012-2:2013: Microscopes—designation of microscope objectives—Part 2: Chromatic correction*.
- Jia, H., Yu, X., Yang, Y., Zhou, X., Yan, S., Liu, C., Lei, M., & Yao, B. 2019. Axial resolution enhancement of light-sheet microscopy by double scanning of Bessel beam and its complementary beam. *Journal of Biophotonics*, 12(1).
- Jorand, R., Le Corre, G., Andilla, J., Maandhui, A., Frongia, C., Lobjois, V., Ducommun, B., & Lorenzo, C. (2012). Deep and clear optical imaging of thick inhomogeneous samples. *PLoS One*, 7(4), 1–9.
- Kafian, H., Lalenejad, M., Moradi-Mehr, S., Birgani, S. A., & Abdollahpour, D. 2020. Light-Sheet Fluorescence Microscopy with Scanning Non-diffracting Beams. *Scientific Reports*, 10(1), 1–12.
- Keller, P. J., Schmidt, A. D., Santella, A., Khairy, K., Bao, Z., Wittbrodt, J., & Stelzer, E. H. K. 2010. Fast, high-contrast imaging of animal development with scanned light sheet-based structured-illumination microscopy. *Nature Methods*, 7(8), 637–642.
- Keller, P. J., Schmidt, A. D., Wittbrodt, J., & Stelzer, E. H. K. 2008. *Reconstruction of Zebrafish Early Light Sheet Microscopy*. 322(November), 1065–1069.
- Keller, P. J., Schmidt, A. D., Wittbrodt, J., & Stelzer, E. H. K. 2011. Digital scanned laser light-sheet fluorescence microscopy (DSLIM) of zebrafish and drosophila embryonic development. *Cold Spring Harbor Protocols*, 6(10), 1235–1243.
- Keller, P. J., & Stelzer, E. H. 2008. Quantitative in vivo imaging of entire embryos with Digital Scanned Laser Light Sheet Fluorescence Microscopy. *Current Opinion in Neurobiology*, 18(6), 624–632.
- Khonina, S. N., Kazanskiy, N. L., Karpeev, S. V., & Butt, A. 2020. *Bessel Beam : Significance and Applications- A Progressive Review Bessel Beam : Significance and Applications — A Progressive Review. November*.
- Lau, S. C., Chiu, H. C., Zhao, L., Zhao, T., Loy, M. M. T., & Du, S. 2018. An integrated single- and two-photon non-diffracting light-sheet microscope. *Review of Scientific Instruments*, 89(4), 5–10.

- Lavagnino, Z., Cella Zancchi, F., Ronzitti, E., & Diaspro, A. 2013. Two-photon excitation selective plane illumination microscopy (2PE-SPIM) of highly scattering samples: characterization and application. *Optics Express*, 21(5), 5998.
- Li, S., Jiao, J., Boonruangkan, J., Toh, H. T., An, J., Su, P. C., Suchand Sandeep, C. S., & Kim, Y. J. 2021. Self-reconstructing Bessel beam created by two-photon-polymerized micro-axicon for light-sheet fluorescence microscopy. *Results in Physics*, 24, 104111.
- Licea-Rodriguez, J., Figueroa-Melendez, A., Falaggis, K., Plata Sánchez, M., Riquelme, M., & Rocha-Mendoza, I. 2019. Multicolor fluorescence microscopy using static light sheets and a single-channel detection. *Journal of Biomedical Optics*, 24(01), 1.
- Lichtman, J. W., & Conchello, J. 2005. *Fluorescence microscopy*. 2(12).
- Liu, S., & Hua, H. 2011. Extended depth-of-field microscopic imaging with a variable focus microscope objective. *Optics Express*, 19(1), 353.
- Luna-Palacios, Y. Y., Licea-Rodriguez, J., Camacho-Lopez, M. D., Teichert, I., Riquelme, M., & Rocha-Mendoza, I. 2022. Multicolor light-sheet microscopy for a large field of view imaging: A comparative study between Bessel and Gaussian light-sheets configurations. *Journal of Biophotonics*, January, 1–15.
- MacDonald, M. P., Reidt, S. L., Correia, R. B. C., Weijer, C. J., & Donnachie, M. 2017. *Gaussian vs. Bessel light-sheets: performance analysis in live large sample imaging*. 1034709(August 2017), 9.
- Mazilu, M., Stevenson, D. J., Gunn-Moore, F., & Dholakia, K. 2010. Light beats the spread: “Non-diffracting” beams. *Laser and Photonics Reviews*, 4(4), 529–547.
- McGloin, D., & Dholakia, K. 2005. Bessel beams : Diffraction in a new light. *Contemporary Physics*, 46(1), 15–28.
- Meinert, T., & Rohrbach, A. 2019. Light-sheet microscopy with length-adaptive Bessel beams. *Biomedical Optics Express*, 10(2), 670.
- Müllenbroich, M. C., Silvestri, L., Di Giovanna, A. P., Mazzamuto, G., Costantini, I., Sacconi, L., & Pavone, F. S. 2018. High-fidelity imaging in brain-wide structural studies using light-sheet microscopy. *ENeuro*, 5(6), 1–13.
- Müllenbroich, M. C., Turrini, L., Silvestri, L., Alterini, T., Gheisari, A., Vanzi, F., Sacconi, L., & Pavone, F. S. 2018. Bessel Beam Illumination Reduces Random and Systematic Errors in Quantitative Functional Studies Using Light-Sheet Microscopy. *Frontiers in Cellular Neuroscience*, 12(September), 1–12.
- Olarte, O. E., Andilla, J., Gualda, E. J., & Loza-Alvarez, P. 2018. Light-sheet microscopy : a tutorial. *Avances in Optics and Photonics*, 10(1), 111–179.

- Olarte, O. E., Licea-Rodriguez, J., Palero, J. A., Gualda, E. J., Artigas, D., Mayer, J., Swoger, J., Sharpe, J., Rocha-Mendoza, I., Rangel-Rojo, R., & Loza-Alvarez, P. 2012. Image formation by linear and nonlinear digital scanned light-sheet fluorescence microscopy with Gaussian and Bessel beam profiles. *Biomedical Optics Express*, 3(7), 1492.
- Planchon, T. A., Gao, L., Milkie, D. E., Davidson, M. W., Galbraith, J. A., Galbraith, C. G., & Betzig, E. 2011. Rapid three-dimensional isotropic imaging of living cells using Bessel beam plane illumination. *Nature Methods*, 8(5), 417–423.
- Power, R. M., & Huisken, J. 2017. A guide to light-sheet fluorescence microscopy for multiscale imaging. *Nature Methods*, 14(4), 360–373.
- Remacha, E., Friedrich, L., Vermot, J., & Fahrbach, F. O. 2020. How to define and optimize axial resolution in light-sheet microscopy: a simulation-based approach. *Biomedical Optics Express*, 11(1), 8.
- Ritter, J. G., Spille, J.-H., Kaminski, T., & Kubitscheck, U. 2011. A cylindrical zoom lens unit for adjustable optical sectioning in light sheet microscopy. *Biomedical Optics Express*, 2(1), 185.
- Siedentopf, H., & Zsigmondy, R. 1903. Über Sichtbarmachung und Größenbestimmung ultramikroskopischer Teilchen. *Annalen Der Physik*, 4(1), 1–39.
- Stefaniuk, M., Gualda, E. J., Pawlowska, M., Legutko, D., Matryba, P., Koza, P., Konopka, W., Owczarek, D., Wawrzyniak, M., Loza-Alvarez, P., & Kaczmarek, L. 2016. Light-sheet microscopy imaging of a whole cleared rat brain with Thy1-GFP transgene. *Scientific Reports*, 6, 1–9.
- Suchand Sandeep, C. S., Sarangapani, S., Hong, X. J. J., Aung, T., Baskaran, M., & Murukeshan, V. M. 2019. Optical sectioning and high resolution visualization of trabecular meshwork using Bessel beam assisted light sheet fluorescence microscopy. *Journal of Biophotonics*, 12(12), 1–6.
- Takanezawa, S., Saitou, T., & Imamura, T. 2021. Wide field light-sheet microscopy with lens-axicon controlled two-photon Bessel beam illumination. *Nature Communications*, 12(1).
- Teichert, I., Nowrousian, M., Pöggeler, S., & Kück, U. 2014. The Filamentous Fungus *Sordaria macrospora* as a Genetic Model to Study Fruiting Body Development. In *BS:ADGEN* (Vol. 87). Elsevier.
- Teichert, I., Pöggeler, S., & Nowrousian, M. 2020. *Sordaria macrospora*: 25 years as a model organism for studying the molecular mechanisms of fruiting body development. *Applied Microbiology and Biotechnology*, 104(9), 3691–3704.
- Verveer, P. J., Swoger, J., Pampaloni, F., Greger, K., Marcello, M., & Stelzer, E. H. K. 2007. High-resolution three-dimensional imaging of large specimens with light sheet-based microscopy. *Nature Methods*, 4(4), 311–313.
- Vettenburg, T., Dalgarno, H. I. C., Nylk, J., Coll-Lladó, C., Ferrier, D. E. K., Čižmár, T., Gunn-Moore, F. J., & Dholakia, K. 2014. Light-sheet microscopy using an Airy beam. *Nature Methods*, 11(5), 541–544.

- Voie, A. H., Burns, D. H., & Spelman, F. A. 1993. Orthogonal-plane fluorescence optical sectioning: threedimensional imaging of macroscopic biological specimens. *Journal of Microscopy*, 170, 229–236.
- W. Goodman. 1996. *Introduction to Fourier Optics* (Second edi). McGraw-Hill.
- Welf, E. S., Driscoll, M. K., Dean, K. M., Claudia., S., Chu, J., Davidson, M. W., Lin, M. Z., Danuser, G., & Floika, R. 2017. Quantitative Multiscale Cell Imaging in Controlled 3D Microenvironments. *Physiology & Behavior*, 176(3), 139–148.
- Wu, Y., Chandris, P., Winter, P. W., Kim, E. Y., Jaumouillé, V., Kumar, A., Guo, M., Leung, J. M., Smith, C., Rey-Suarez, I., Liu, H., Waterman, C. M., Ramamurthi, K. S., La Riviere, P. J., & Shroff, H. 2016. Simultaneous multiview capture and fusion improves spatial resolution in wide-field and light-sheet microscopy. *Optica*, 3(8), 897.
- Xiong, B., Han, X., Wu, J., Xie, H., & Dai, Q. 2020. Improving axial resolution of Bessel beam light-sheet fluorescence microscopy by photobleaching imprinting. *Optics Express*, 28(7), 9464.
- Zhang, P., Phipps, M. E., Goodwin, P. M., & Werner, J. H. 2016. Light-sheet microscopy by confocal line scanning of dual-Bessel beams. *Journal of Biomedical Optics*, 21(10), 100502.
- Zhang, Y. 2007. Simple and rigorous analytical expression of the propagating field behind an axicon illuminated by an azimuthally polarized beam. *Applied Optics*, 46(29), 7252–7257.
- Zhao, T., Lau, S. C., Wang, Y., Su, Y., Wang, H., Cheng, A., Herrup, K., Ip, N. Y., Du, S., & Loy, M. M. T. 2016. Multicolor 4D Fluorescence Microscopy using Ultrathin Bessel Light Sheets. *Scientific Reports*, 6.

Annexes

Image processing and data storage

```

////////////////////Stack processing////////////////////
////////Advanced microscopy laboratory, CICESE////////
////////////////////2020////////////////////
////////////////////

////////Open the raw stack //////////
Stackoriginal=File.openDialog("Select Stack");
open(Stackoriginal); //Filename
rename("image_3.tif")
////////Open the nose //////////
noise=File.openDialog("Select nose");
open(noise); //Filename el nombre de la imagen
rename("ruido1.tif")

////////////////////taking out background, NaNs and the hot pixels////////////////////
imageCalculator("Subtract create stack", "image_3.tif","ruido1.tif"); //Result of image_3
////////////////////
//run("Remove NaNs...", "radius=2 stack");
run("Remove Outliers...", "radius=1 threshold=1 which=Bright stack");
run("Unsharp Mask...", "radius=2 mask=0.4 stack");
run("Gaussian Blur...", "sigma=.6 stack");
rename ("image_3-1.tif")
//Removed the noise from the front and back images for each plane n of the image stack /
//////////////////// $\Delta 2n=Im_{(n+1)}-Im_{(n)}$ ////////////////////
//////////////////// front image minus back image //////////////////////
t = nSlices;
s=2
i= 1
for (i=-1;i<=0 ;i++) {
    selectWindow("image_3-1.tif");
    slices=""+(s+1*i)+"-"+(t+i);
    run("Make Substack...", " slices=" + slices);
    rename ("N"+(i+s));
}
////////////////////DIFERENCIA 1 - 2 y 2-1 //////////////////////
imageCalculator("Subtract create stack", "N1","N2"); // "diferencia 1-2"
rename("Diferencia_1-2.tif")

imageCalculator("Subtract create stack", "N2","N1"); //"diferencia 2-1"
rename("Diferencia_2-1.tif")

//The 1st plane is removed from Diferencia_1-2.tif
x=1
for (i=0;i<=1 ;i++) {
    selectWindow("Diferencia_1-2.tif");
    slices=""+(x+1*i)+"-"+(t-1);
    run("Make Substack...", " slices=" + slices);
    close("Diferencia_1-2.tif");
    rename ("Diferencia_1-2.tif");
} //from 2nd plane to N-1

//The 1st plane is removed from Diferencia_2-1.tif
for (i=0;i<=0 ;i++) {

```

```

selectWindow("Diferencia_2-1.tif");
slices=""+(x+1*i)+"-"+(t-2);
run("Make Substack...", " slices=" + slices);
close("Diferencia_2-1.tif");
rename ("Diferencia_2-1.tif");
} // from 1st plane to N-2

//The last plane is removed from N2
for (i=0;i<=0 ;i++) {
selectWindow("N2");
slices=""+(x+1*i)+"-"+(t-2);
run("Make Substack...", " slices=" + slices);
close("N2");
rename ("N2");
}

//////////////////////////////////Im2=Im-Δ1-Δ2//////////////////////////////////

imageCalculator("Subtract create stack", "N2","Diferencia_1-2.tif"); // Noise is removed by
Diferencia_1_2...
rename("Imagen_1-2.tif") // image without backplane contribution  $[\Delta 2]_n = [Im]_{(n+1)} - [Im]_n$ 

imageCalculator("Subtract create stack", "Imagen_1-2.tif", "Diferencia_2-1.tif");
rename("Imagen_Final.tif")

selectWindow("Diferencia_2-1.tif");
close();
selectWindow("Diferencia_1-2.tif");
close();
selectWindow("Imagen_1-2.tif");
close();
selectWindow("N2");
close();
selectWindow("image_3-1.tif");
close();
selectWindow("N1");
close();
selectWindow("ruido1.tif");
close();
selectWindow("image_3.tif");
rename ("original.tif")
//////////////////////////////////
rename ("raw stack.tif")
//////////////////////////////////
run("Tile");
//////////////////////////////////
//////////////////////////////////
//////////////////////////////////

```

All the MACROS are available in: <https://github.com/ylunapal/LightSheet-MACROS.git>

Beam propagation simulation

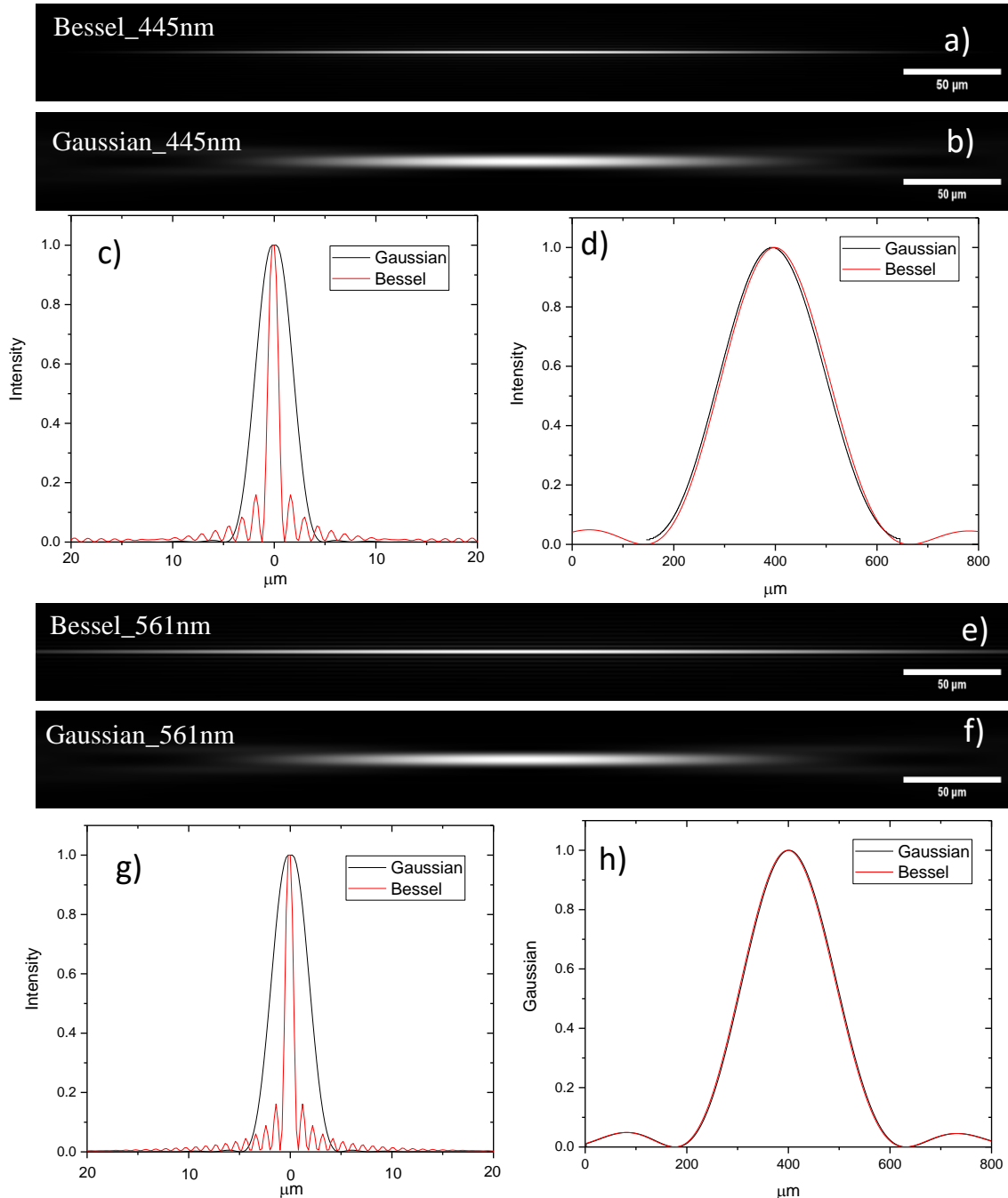


Figure 34 Bessel (a) and Gaussian (b) beam propagation under a 0.16 NA objective. Both cases are under experimental settings for 445 nm. Normalized intensity profile traces along the x-direction c) and z-direction d) of figures a, b. Bessel (e) and Gaussian (f) beam propagation under a 0.16 NA objective. Both cases are under experimental settings for 561 nm. Normalized intensity profile traces along the x-direction e) and z-direction f) of figures e, f.

MATLAB code: https://github.com/ylunapal/Beam_propagation_Bessel.git